Transactions in Theoretical and Mathematical Physics

Publisher: Qom University of Technology

ISSN: 3041-8984

Volume**:** 2, Issue 2, 2025

Available online: https://ttmp.qut.ac.ir

Table of Contents

Equivalent classes of square – integrable functions in the Hilbert space
Mehdi Jafari Matehkolaee
Pages 66-69

A brief Survey on the Selberg Trace formula (the compact case)
Jafar Shaffaf
Pages 70-76

Quantum Acoustics: Investigation of Phonons, Their Physical Properties, and Interactions with Quantum Systems
Bahareh Khishkhah; Reza Sharifian; mohammad fatemi mofrad; Hadiseh Sadri; Rasoul Sadighi-Bonabi
Pages 77-83

Adaptive numerical optimization for high-fidelity quantum gate vontrol in atom Interferometers
Javad Sharifi
Pages 84-90

Asymptotic behaviors of solutions to a singular non-local fourth-order parabolic equation with gradient-type logarithmic nonlinearity
Tingfu Feng; Ruixi Li; Mengrui Yang
Pages 91-109

Effect of time reversal symmetry on the current-phase relation in Josephson junctions including two-gap superconductors
Masoumeh Avarideh; Reza Afzali
Pages 110-115

TTMP vol 2 (2), 2025
doi: 10.30511/TTMP.2025.2054761.1050

Transactions in Theoretical and Mathematical Physics

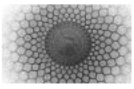

Equivalent classes of square–integrable functions in the Hilbert space

Mehdi Jafari Matehkolaeei[1a]

[1] Department of Physics, Amirkabir University of Technology (Tehran Polytechnic) P.O.Box:15875-4413, Tehran, Iran

Received: 01 March 2025 / Accepted: 17 May 2025 / Published: 17 May 2025

Abstract In this paper, we have discussed that the members of the Hilbert space are indeed not square-integrable functions themselves, but rather, the members are equivalent classes of these functions. Contemplating these functions compels us to distinguish between two operators. First, the ordinary derivative $\frac{d}{dx}$ is just the usual partial differentiation which acts on the scalar function and should not be considered as an operator which can act on the vectors in the Hilbert space. Second, the unbounded operator D_x, which is usually mixed up with the former.

1 Introduction

Quantum mechanics is one of the contexts in which the Hilbert space is used. A rigorous definition for a Hilbert space should be sought in mathematical analysis. However, this rigorous definition of the Hilbert space is not included in almost all practical applications of quantum mechanics. That is why, in most texts on quantum mechanics, especially those addressed by physicists, no attention is given to this. However, in the third chapter of the book [1], the author has discussed this subject in summary and footnotes. Ref. [2] is perhaps the only quantum mechanics book that has dealt with this issue more than others. If one were to trace the origins of the concept of a Hilbert space in mathematics and physics, it would be noticed that Hilbert space theory is part of functional analysis [3, 4].

In standard quantum mechanics, some complex Hilbert space describes a quantum mechanical system. For instance, the pure states of a single one-dimensional particle can be described by elements in the Hilbert space $L^2(\mathbb{R})$, as introduced in introductory courses in quantum mechanics. Generally, it is important to note that the L^2 space is the only space among the L^p spaces for which the norm comes from an inner product. The first natural attempt to define this space mathematically is the following:

$$L^2(\mathbb{R}) = \Big\{ f : \mathbb{R} \to \mathbb{C} \ : \ f_{[-n,n]} \text{ Riemann integrable, for } n \in \mathbb{N}, \int_{-\infty}^{\infty} |f(x)|^2 \, dx < \infty \Big\}. \tag{1}$$

In the definition (1), functions f are so-called square-integrable functions and Riemann integrable. In general, a Hilbert space is a set of vectors equipped with two operations: vector addition and scalar multiplication. It satisfies the axioms of a vector space over the field of complex numbers (or real numbers).

However, there are several problems with this approach. For example, there are plenty of square-integrable functions (according to definition (1)) which do not vanish at infinity [5]. Indeed, it is false that $f \in L^2(\mathbb{R})$ implies that $f \to 0$ as $x \to \infty$, as commonly believed. Additionally, the Hilbert space defined in (1) is not complete[1]. There exist some Cauchy sequences in $L^2(\mathbb{R})$ which do not converge in $L^2(\mathbb{R})$. For example, consider the sequence $\{\psi_j\}$, where ψ_j is a function such that $\psi_j(q_i) = 1$ for $i \leq j$, and $\psi_j(x) = 0$ otherwise. Here $\{q_i\}$ denotes an enumeration of the rational numbers[2].

[a] m.matehkolaee@aut.ac.ir

[1] There are plenty of examples which demonstrate that both the set of irrational and rational numbers are not complete. There are well-behaved sequences in each space that don't converge to an element of the space. These sequences are well-behaved in the sense that they do converge in $\mathbb{R}$.

[2] In fact, ψ_j is a sequence of functions such that $\psi_1, \psi_2, \psi_3, \ldots$. For instance, $\psi_3(q_1) = 1$, $\psi_3(q_2) = 1$, and $\psi_3(q_3) = 1$. So $\psi_3(x) = 1$ if x is one of the first three rationals; otherwise, $\psi_3(x) = 0$. Hence, each $\psi_j(x) = 0$ except for a finite number of points (to be more specific, except for three points)

Clearly, for each ψ_j, we have $\int_{-\infty}^{\infty} |\psi_j(x)|^2\, dx = 0$, and this is true for $(\psi_i - \psi_j)$ hence for any i and j the amount $(\psi_i - \psi_j)$ is nonzero only in a finite number of points. So ψ is a Cauchy sequence. While the limit of this sequence is the function $\varphi(x)$ so that $\varphi(x) = \begin{cases} 1, & x \in \mathbb{Q}, \\ 0, & x \notin \mathbb{Q}, \end{cases}$ where $\mathbb{Q}$ is a set of rational numbers. Now, we can conclude that $|\varphi|^2$ is not Riemann integrable.

As a result, if the inner product is defined using Riemann integration, the Cauchy sequence $\{\psi_j\}$ does not converge in the space of square-integrable functions. However, if Lebesgue integration is used, the Cauchy sequence converges. Also, if the inner product is defined with Lebesgue integration, the Cauchy sequence ψ does converge.

In a later section, we will discuss the distinction between the operators $\frac{d}{dx}$ and Dx.

In some quantum mechanics literature, for example, in [1, 6], misleading notations are seen, which can confuse different operators. We must distinguish between the position operator X and the real number x. Also, $f(x)$ is a number[3]. The symbol $\frac{d}{dx}$ is not well-suited to denote an operator acting on elements of the Hilbert space. Instead, we denote by D_x an operator acting in Hilbert space such that

$(D_x f)(x) = f'(x)$, where $f'(x)$ is the usual derivative of $f(x)$, assuming f is differentiable.

2 Equivalent Classes of Square–Integrable Functions

According to definition (1), we can define the norm $\|f\| = \left(\int_{-\infty}^{\infty} |f(x)|^2\, dx\right)^{1/2}$ as a norm on $L^2(\mathbb{R})$. However, there exist functions $f \in L^2(\mathbb{R})$, with $f \neq 0$, for which $\|f\| = 0$. As an example, consider the function $f(x) = \begin{cases} 1, & x = 0, \\ 0, & x \neq 0. \end{cases}$ This function is clearly not identically zero, but $\int_{-\infty}^{\infty} |f(x)|^2\, dx = 0$. To resolve this, we introduce an equivalence relation: two functions $f, g \in L^2(\mathbb{R})$, where $\|f-g\|_2 = 0$. These functions are called *equivalent* if

$$\int_{-\infty}^{\infty} |f(x) - g(x)|^2\, dx = 0. \tag{2}$$

According to Eq. (3), the functions f and g can be different on some poinbts. Therefore, when the operator D_x is applied to a function, we must account for this equivalence. For example, suppose f is differentiable and g equals f except at a single point x_1. Then g is not differentiable at x_1, but $D_x g$ is still defined as $D_x f$, because f and g are equivalent.

As an example for this points, consider the square-integrable function $f(x) = \frac{1}{1+x^2}$, and define

$$g(x) = \begin{cases} f(x), & x \neq 0, \\ 0, & x = 0. \end{cases} \tag{3}$$

It is noted that the former function is differentiable everywhere and the latter is not differentiable and therefore not continuous at $x = 0$. In fact, the reason that we should consider the equivalence classes rather than functions themselves, is to make the inner product non singular. Here, the inner product of $(f - g)$ by itself is zero, by definition of Eq. (3). While the inner product of a vector by itself should be non-zero (positive) unless that vector is zero. Therefore, if Eq. (3)) is satisfied $(f-g)$ is taken to be equivalent to 0. It means that the action of any linear operator (acting on the Hilbert space) on $(f - g)$ should be zero. So, if $D_x f$ is defined, $D_x g$ or its generalization should be defined equal to $D_x f$. Another point that should be noted is that $D_x f$ is not necessarily square-integrable despite of f being a square-integrable function. So, the domain of D_x is not the whole Hilbert space, but it is an unbounded operator.

Also, it is worthwhile to point out, that if $(f - g)$ is non-zero only at a finite number of points, Eq. (3) will be true. More generally, if the set at which $(f-g)$ is non-zero, has zero measure, then the Eq. (3) is valid and f and g are called equivalent. In other words, if two functions f and g differ from each other on a set with zero measure, then they belong to the same equivalence class[4].

We are now ready to define the desired Hilbert space [7]. A Hilbert space in the context of the Lebesgue measure typically refers to a complete vector space with an inner product defined via the Lebesgue integral.

A classic example of a quantum system in an infinite-dimensional Hilbert space is a quantum particle constrained to move along the real line. In this case, the Hilbert space is defined as $\mathcal{H} := L^2(\mathbb{R}, dx)$,

where dx denotes the standard Lebesgue measure on $\mathbb{R}$. The members of this Hilbert space are equivalence classes of measurable functions $f : \mathbb{R} \to \mathbb{C}$ with unit norm, $\|f\|_2 = \int_{\mathbb{R}} |f(x)|^2\, dx = 1$.

In this formal setting, momentum operators can be precisely defined using weak derivatives [8]. These definitions are elaborated in [7], where the discussion is extended to generalized momentum operators and domains [9].

[3] Note that f is a smooth and differentiable function and $f(x)$ is a pointwise evaluation at x, just like x itself. That is, $f(x)$ is the value of the function f at the point x.

[4] As an example, consider two functions f and g that differ only on the set of integers or a subset thereof. Since the measure of the integers is zero, $f \sim g$ in $L^2(\mathbb{R})$.

3 Difference between D_x and $\frac{d}{dx}$

This section discusses the differential operator, which acts on square-integrable functions in a Hilbert space. It is different from the usual differential operator defined in classical calculus.

One can define the operator D_x through its action on the Fourier transform of the function. For a function ψ, the Fourier transform satisfies the following identity:

$$F(D\psi)(k) = ik(F\psi)(k), \tag{4}$$

This gives a correspondence between $D_x\psi$ and multiplication by ik in the Fourier domain.

So, using above equation, we can deduce

$$(D_x\psi)(x) = \frac{1}{2\pi}\int\int e^{ikx-iky}\psi(y)\cdot(ik)\,dk\,dy. \tag{5}$$

If ψ is differentiable in the usual sense, then the right-hand side is equal to the derivative of this function. But the point is that, it can happen that the right-hand side exists, while ψ is not differentiable in the usual sense. Hence, Eq. (5) is some generalization of the definition of the derivative of ψ.

It should be npted that the operator D_x defined above is a dense in the Hilbert space. An operator is said to be densely defined in the Hilbert space if for any u and for any $\varepsilon > 0$, there exists a v such that $\|u - v\| < \varepsilon$ in the domain of the regarding operator.

Let $F(v)$ be the Fourier transform of v. It is shown that the Fourier transform of D_xv, denoted $F(D_xv)$, satisfies:

$$|F(D_xv)(k)|^2 = k^2|F(v)(k)|^2. \tag{6}$$

Now suppose $F(v)(k) = 0$ for $|k| > M$, where M is some constant. Then:

$$\int |F(D_xv)(k)|^2\,dk \le M^2\int |F(v)(k)|^2\,dk. \tag{7}$$

For v in the Hilbert space, the right-hand side and hence the left-hand side will be finite. We immediately infer if v is in the Hilbert space and its Fourier transform vanishes for $|k|$ bigger than some constant, then v is in the domain of D_x.

This result implies that if a function $v \in L^2(\mathbb{R})$ has a compactly supported Fourier transform, i.e., vanishes for $|k| > M$, then $D_xv \in L^2(\mathbb{R})$, and v belongs to the domain of the operator D_x.

For any vector u in Hilbert space, the square-integrability is defined via its Fourier transform by:

$$\int |Fu(k)|^2\,dk < \infty. \tag{8}$$

This means that for any $\alpha > 0$, there exists an N such that:

$$\left|\int |(Fu)(k)|^2 - \int_{-N}^{N} |(Fu)(k)|^2 dk\right| < 2\pi\alpha. \tag{9}$$

One can take ν to be a function with the following properties:

$$\mathcal{F}v(k) = \begin{cases} \mathcal{F}u(k), & |k| \le N, \\ 0, & |k| > N. \end{cases}$$

Clearly, v in in the domain of D_x and $|u - v|^2 \le \alpha$. So, for any $\varepsilon > 0$ ine take $\alpha = \frac{1}{2}\varepsilon^2$ and $|u - v| < \varepsilon$, while v is in the domain of D_x.

4 Conclusion

One of the key properties of the real numbers $\mathbb{R}$ is that all Cauchy sequences converge. This is proven in many real analysis texts, such as Chapter 1 of [10] or in [11].

However, we have shown that if the inner product is defined using Riemann integration, then $L^2(\mathbb{R})$ is *not* complete. This highlights the need for the Lebesgue integral. As discussed in this paper, if the inner product is defined using the Lebesgue integral, then $L^2(\mathbb{R})$ is a complete Hilbert space, meaning every Cauchy sequence converges within the space.

As a result, the members of the Hilbert space, contrary to common belief, are not square-integrable functions themselves but equivalence classes of such functions. To emphasise this difference, we may denote equivalence classes by a notation such as $[f]$.

As it is shown, this point is not only a curiosity or mathematical accuracy, but it leads to the distinction of two operators, which can remove some misconceptions. We should stress the difference between the two operators. The operator $\frac{d}{dx}$ acts on any object depending on x, be it scalar or vector. However the operator $D_x$is an unbounded operator which acts from right on vectors and convectors in the Hilbert space.

Acknowledgement

We thank Professor Mohammad Reza Sarkardei for reading the manuscript, and Professor Mohammad Khorrami for suggesting several improvements in the presentation.

References

1. D. J.Griffiths, D.F.Schroeter, *Introduction to quantum mechanics*, 3rd Cambridge University Press, (2018)
2. C. J.Isham, *Lectures on Quantum Theory: Mathematical and Structural Foundations*, ICP (1995).
3. K. S. Ranade, Fortschritte der Phy. **63**, (2015)
4. J. Dittrich, H.Kovarik, A.Laptev, J. Eur. Math. Soc. (2017)
5. F. Gieres, Rep. Prog. Phys. **63**, (2001)
6. S. Gasirowicz, *Quantum mechanics*, 3rd Edition, John Wiley, New York (2003)
7. V.Moretti, Int.J.Geom. Meth. Mod.Phys. **13**, (2016)
8. M. Jafari Matehkolaee, A. Hoseinian Abarghoei, Tran. Th. Math. Phys., **1**, (2024)
9. M. Jafari Matehkolaee and G. Rastegarzadeh, Pramana. J. Phys. **95**, (2021)
10. H.L.Royden, *Real Analysis*, Prentic Hall, (1988)
11. G.Folland, *Real Analysis: Modern Techniques and Their Applications*, Wiley, (1999)

TTMP vol 2 (2), 2025
doi: 10.30511/TTMP.2025.2048769.1045

Transactions in Theoretical and Mathematical Physics

A brief survey on the Selberg trace formula (the compact case)

Jafar Shaffaf[1 a b]

[1]Department of Mathematical Sciences, Shahid Beheshti University

Received: 23 December 2024 / Accepted: 18 May 2025 / Published: 26 May 2025

Abstract In this note, we aim to elucidate the fundamental mathematical concepts and mathematical ingredients underlying the Selberg trace formula. We explicitly present the formula for compact quotients and provide a brief overview of its interpretation in both mathematics and physics. The Selberg trace formula transcends the boundary of mathematics, establishing intriguing connections between classical mechanical entities such as volume, shape, and geodesics on a surface and quantum mechanical entities such as eigenvalues (frequencies), eigenfunctions, and resonances of the underlying geometry. A rudimentary understanding of complex analysis and hyperbolic geometry is assumed.

1 Introduction

I prepared this note for a conference on mathematical physics held in July 2024 at Qom university of technology in Qom city. Delivering a lecture on the Selberg trace formula sparked my curiosity to delve deeper into its intricate beauty and profound significance. I was fascinated by the beauty of the Selberg trace formula while preparing this report. This note serves as a (very) brief survey of the Selberg trace formula and some of its relatives which have far-reaching applications in various mathematical and physical domains, and I hope that this note will help to introduce it to others.

We begin by introducing a pivotal group known as the modular group, denoted by $\Gamma = SL(2,\mathbb{Z})$. This group acts naturally on the upper half plane $\mathscr{H}$ by linear-fractional transformations and the resulting quotient of this action is the modular surface denoted by $M = \mathscr{H}/SL(2,\mathbb{Z})$. For the interested reader, a brief introduction to hyperbolic geometry and complex analysis is essential. The modular surface $M = \mathscr{H}/SL(2,\mathbb{Z})$ is a rich mathematical entity, not only from a hyperbolic geometric perspective but also from a harmonic analysis standpoint. The following figure illustrates the renowned fundamental domain of the action of the group $SL(2,\mathbb{Z})$ on the upper half plane. This fundamental domain is also known as the Gauss fundamental domain, as Gauss had discovered it using quadratic forms (of negative discriminant) before the advent of hyperbolic geometry!

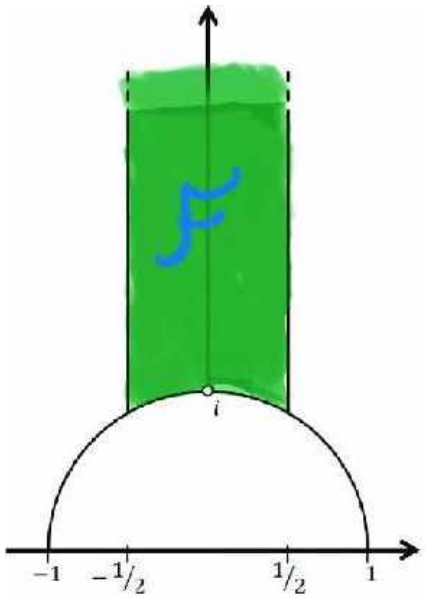

The resulting quotient surface, known as the modular surface, is a non-compact surface with finite volume (its volume is $\frac{\pi}{3}$). It is noteworthy that the geodesics on the modular surface are the projections of the geodesics in the upper half plane. Here is a picture of the modular surface and a closed geodesic on it.

[a]shaffaf@gmail.com

[b]This research was partially supported by a grant from IPM (No. 1404110116)

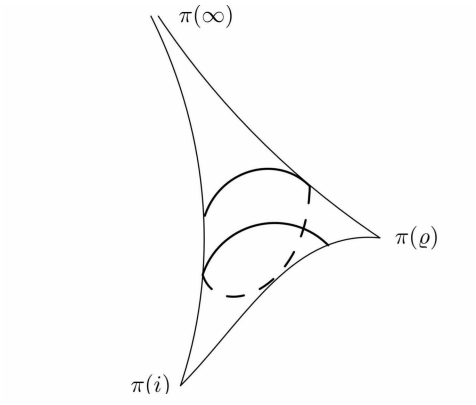

Furthermore, Studying quadratic forms of positive discriminant is closely intertwined with the study of the closed geodesics and their corresponding multiplicities on the aforementioned modular surface. A powerful tool for analyzing the behavior of closed geodesics on the surfaces (both compact or non-compact) is the Selberg trace formula. In this report, I aimed to understand this crucial formula and its significance in understanding closed geodesics on a surface. In fact, the Selberg trace formula establishes a connection between the geodesic geometry of a surface and its spectral geometry (eigenvalues of Laplacian). In this report I primarily focused on the compact case of the Selberg trace formula which is essential before delving into the more challenging case of the non-compact quotient.

The Selberg trace formula was originally discovered by Selberg in the 1950s (see [1]) influenced by the work of Maass, who employed techniques from harmonic analysis to study the spectral theory of hyperbolic surfaces. In essence, the Selberg trace formula is an identity that has a geometric side and deals with geometric entities such as closed geodesics of our underlying geometry (our surface) and a spectral side that involves eigenvalues of Laplacian of the underlying Riemann surface. These eigenvalues are crucial in quantum physics and play the role of modes (frequencies) of a domain or surface (for instance, the sound we hear from a drum). Before formulating the trace formula for hyperbolic surfaces, it is enlightening to consider the trace formula for the unit circle, which is essentially a reformulation of the Poisson summation formula. This formula for a suitable function h is as follows:

$$\sum_{n\in\mathbb{Z}} h(n) = \sum_{n\in\mathbb{Z}} \hat{h}(n), \tag{1}$$

where $\hat{h}(n) = \int_{\mathbb{R}} h(t)e^{2\pi int}dt$ is the Fourier transform of the test function h. Now, if we examine the above poisson summation formula more closely, we can reinterpret both sides of this formula as follows. In fact, the Poisson summation formula serves as the initial prototype of the trace formula. Consider $M = S^1$, a one-dimensional circle of radius 1. It is readily apparent that he eigenvalues of the Laplacian $\Delta = -\frac{d^2}{dx^2}$ on the circle S^1 are n^2 for $n = 0, \pm1, \pm2, \cdots$ with corresponding eigenvalues : $\phi_n(x) = \frac{1}{\sqrt{2\pi}}e^{inx}$. Define the linear operator T on the space of periodic functions as the following

$$[Tf](x) := \int_{[0,2\pi]} \rho(x,y)dy, \tag{2}$$

where the kernel $\rho(x,y) := \sum_{n\in\mathbb{Z}} h(n)\phi_n(x)\bar{\phi}_n(y)$. It is evident that $T\phi_n = h(n)\phi_n$. Consequently, the Poisson summation formula essentially entails computing the trace of the aforementioned linear operators in two different methods.

$$\mathrm{Tr}(T) = \sum_{n\in\mathbb{Z}} h(n) = \int_{\mathbb{R}} h(t)e^{2\pi int}dt. \tag{3}$$

Note that the left-hand side is a spectral quantity, while the right hand side is a geometric quantity, calculated as a sum over the closed geodesics on the manifold S^1 that have length $2\pi|n|$ for $n \in \mathbb{Z}$. In this way, we can see that trace formula for S^1 is actually a reformulation of the Poisson summation formula. We will also see that the strategy for higher-dimensional case of surfaces is quite similar to the above argument.

Furthermore, it is illuminating to examine the trace formula for the 2-dimensional sphere, as we possess explicit knowledge of the spectrum of the Laplacian and the structure of closed geodesics in this special case (similar to the case of circle). However, we omit this enlightening examples (the sphere) in this report and refer to [2, 3] for further details. In the context of hyperbolic surfaces, it is well-known that we have the following correspondence:
Geometric entities $\longleftrightarrow$ spectral entities
(volume, shape, geodesics) $\longleftrightarrow$ (eigenvalues, eigenfunctions, resonances)

Additionally, we can provide motivation from a physics perspective. The classical-quantum correspondence principle in physics relates classical mechanical entities such as closed geodesics, to quantum mechanical entities like resonances and frequencies (modes).

2 Some background in hyperbolic geometry and hyperbolic surfaces

The upper half plane

$$\mathscr{H} = \{z \in \mathbb{C} | Im(z) > 0\}, \tag{4}$$

serves as a standard model for hyperbolic geometry. In this geometry, the straight lines are segments of semi-circles centered at a point on the real line (boundary at infinity) and lines perpendicular to the real line.

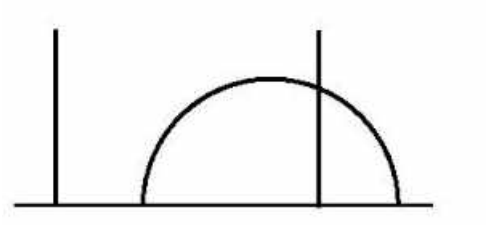

The group of isometries is the Mobius transformations (or linear-fractional transformations) defined as

$$\phi : z \mapsto \frac{az+b}{cz+d}, \tag{5}$$

where $a,b,c,d \in \mathbb{R}$ and $ad-bc>0$. It is well-known that this group is equivalent to the Lie group $PSL(2,R)$ (the group of 2 by 2 matrices with real entries and positive determinants). Furthermore, it is straightforward to demonstrate that the hyperbolic metric:

$$ds^2 = \frac{dx^2+dy^2}{y^2}, \tag{6}$$

is invariant under every element ϕ in the isometry group $PSL(2,R)$, more precisely we have

$$\phi^*(ds^2) = ds^2. \tag{7}$$

The above metric is also known as the Poincare metric. It can be easily observed that the Gaussian curvature of this metric is constant and equal to -1. The area element of this metric is $dA(z) = \frac{dxdy}{y^2}$. One can see that the distance between two points $z,w \in \mathscr{H}$ can be obtained by the following formula:

$$d(z,w) = \log \frac{|z-\bar{w}|+|z-w|}{|z-\bar{w}|-|z-w|}. \tag{8}$$

We classify the transformations in the isometry group $PSL(2,R)$ based on the behavior of their fixed points. Suppose that $T(z) = \frac{az+b}{cz+d}$ is an element of $PSL(2,R)$, and z is a fixed point of this transformation. Then z must satisfy the following quadratic equation:

$$cz^2 + (d-a)z - b = 0. \tag{9}$$

Generally this equation has 2 complex solutions.
(1) The transformation T is called elliptic if it has only one fixed point in the upper half plane (the other is in the lower half plane). In this case, geometrically, T is a rotation centered at the fixed point. One can see that the T is elliptic if and only if $|\mathrm{Tr}(T)| = |a+d| < 2$.
(2) The transformation T is referred to as parabolic if T has only one fixed point on the real line $\mathbb{R} = \partial\mathscr{H}$. In this case, T is conjugate to the translation $z \mapsto z+1$. One can see that the T is parabolic if and only if $|\mathrm{Tr}(T)| = |a+d| = 2$.
(3) The transformation T is called hyperbolic if it has two distinct fixed points on the boundary real line. In this case, T is conjugate to the transformation $z \mapsto e^a z$ for some real number a. One can see that the T is hyperbolic if and only if $|\mathrm{Tr}(T)| = |a+d| > 2$.

Table 1 Complete classification of hyperbolic isometries

Type	Fixed Points	Canonical Form	Trace
Elliptic	1 in $\mathscr{H}$	$\begin{pmatrix} \cos\theta & \sin\theta \\ -\sin\theta & \cos\theta \end{pmatrix}$	$2\cos\theta$
Parabolic	1 on $\partial\mathscr{H}$	$\begin{pmatrix} 1 & 1 \\ 0 & 1 \end{pmatrix}$	2
Hyperbolic	2 on $\partial\mathscr{H}$	$\begin{pmatrix} e^{l/2} & 0 \\ 0 & e^{-l/2} \end{pmatrix}$	$2\cosh(l/2)$

Now, we consider a Fuchsian group , which is a discrete subgroup of the isometry group $PSL(2,\mathbb{R})$. Our primary example in this context for a Fuchsian group is the discrete subgroup $SL(2,\mathbb{Z})$, which comprises 2 by 2 matrices with integer entries and determinant 1. This subgroup holds significant importance and is known as the modular group. It finds applications across various mathematical disciplines, ranging from number theory to physics. When a discrete group acts on the upper half plane $\mathscr{H}$ we can define a fundamental domain for this action. This domain is a polygonal region in the plane, ensuring that every orbit intersects the domains interior at most once (except for the boundary of this region). For instance, a fundamental domain for the modular group action is depicted in the following figure.

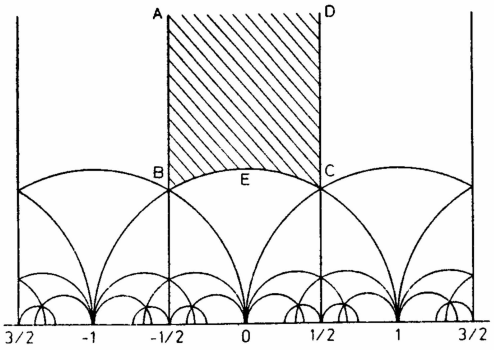

It's worth noting that if the fauchsian subgroup lacks parabolic and elliptic element, the quotient Riemann surface $S = \mathscr{H}/\Gamma$ is a compact Riemann surface with constant negative curvature -1. However, in the case $\Gamma = PSL(2,Z)$, the quotient surface, known as modular surface, is not compact. It possesses a cusp at infinity and also has finite volume. Geodesics on the modular surface S (or generally on any Riemann surface) correspond to the geodesics of the upper half plane under the action of the modular group. A function on the quotient $S = \mathscr{H}/\Gamma$ is a function on the upper half plane $\mathscr{H}$ which is invariant under the action of the Fuchsian group , meaning $f(gz) = f(z)$ for all $g \in \Gamma$. These functions are referred to as automorphic functions. Closed geodesics and their characterization on a Riemann surface (specially on the modular surface) holds immense importance in studying the surfaces geometry. They also serve as the foundation for comprehending the Selberg trace formula. When dealing with geodesics on the Riemann surface S, several key questions arise :

1) which geodesics are closed on the surface S.
2) Which closed geodesics are simple?
3) Are there dense geodesics on the surface, and how can they be characterized?

The answer to the first question is the following. Every hyperbolic matrix in $SL(2,\mathbb{Z})$ generates a closed geodesic and it is easy to see that any matrix in the modular group with trace greater than 2 is hyperbolic. Therefore, the closed geodesics correspond to conjugacy classes of hyperbolic elements in the Fuchsian group Γ.

The Laplacian operator on the upper half plane H with Poincare metric is defined as

$$\Delta := -y^2(\frac{\partial^2}{\partial x^2} + \frac{\partial^2}{\partial y^2}). \tag{10}$$

Since the hyperbolic Laplacian is invariant under the action of the group $\Gamma = SL(2,Z)$, i.e. $go\Delta = \Delta og$ for $g \in SL(2,R)$, it descends on the quotients Riemann surface $S = \mathscr{H}/\Gamma$. The area measure $dA(z) = \frac{dxdy}{y^2}$ is also invariant under the action of the group and so it gives an area measure (volume form) over the quotient Riemann surface S. The natural Hilbert space that we consider is $L^2(\mathscr{H}/\Gamma, dA)$ with the inner product

$$< f,g >:= \int_F f(z)\bar{g(z)}dA(z), \tag{11}$$

for a fundamental domain F. An eigenvalue of Δ on $S = \mathscr{H}/\Gamma$ is a number λ which satisfies the equation $\Delta\phi = \lambda\phi$ where $\phi \in L^2(\mathscr{H}/\Gamma, dA)$ is a square integrable function and in the literature the corresponding eigenfunction is called a Maass form. It is a well-known fact that if the quotient Riemann surface is compact, its corresponding spectrum is discrete and tends to infinity. Additionally there exists an orthogonal basis of eigenfunctions $\{\phi_j\}$ for $L^2(\mathscr{H}/\Gamma, dA)$. If the quotient Riemann surface is not compact but of finite volume then the corresponding spectrum has two parts, one is the discrete part contained in the interval $[0,\infty)$ and the other is the continuous part and is in fact it is the interval $[\frac{1}{4},\infty)$. In the case of non-compact quotient we attempt to study the spectrum by introducing a new operator called the resolvent, denoted as $R(\lambda) := (\Delta - \lambda)^{-1}$. It is important to note that in the upper half plane, $\mathscr{H}$, we have $\Delta y^s = s(1-s)y^s$. Therefore we assume that our spectral parameter is $\lambda = s(1-s)$ and the resolvent is

$$R(s) := (\Delta - s(1-s))^{-1}. \tag{12}$$

It is well known that the resolvent admits a meromorphic continuation to the entire complex plane. The set $\lambda \in [0,\infty)$ corresponds to

$$s \in [\frac{1}{2},1] \cup \{s|Re(s) = \frac{1}{2}\}, \tag{13}$$

(see [4]). Recall that in the literature, the poles of the meromorphically extended resolvent are referred to as resonances. Another well-known result is that the continuous spectrum is parametrized by the Eisenstein series. Furthermore, the Eisenstein series can also be meromophically continued to the complex plane with respect to the variable s. Now, we endeavor to describe the Selberg trace formula in the case of compact quotients. Assume that the function $f \in C^\infty([0,\infty))$ decays sufficiently rapidly at infinity. In this case, we can define the integral operator by introducing the kernel.

$$k_f(z,w) := \sum_{g\in\Gamma} f(d(z,gw)), \tag{14}$$

and following the above kernel one can define the operator $K_f : L^2(S,dA) \to L^2(S,dA)$ as follows:

$$(K_f(g))(z) := \int_F k_f(z,w)g(w)dA(w). \tag{15}$$

The Selberg trace formula provides two distinct methods for computing the trace of the operator K_f. In the case of the compact quotient $S = \mathscr{H}/\Gamma$ as we mentioned, we have a

discrete spectrum $\{\lambda_j\}$ and corresponding orthogonal eigenfunctions $\{\phi_j\}$. On the one hand, we have

$$\mathrm{Tr}(K_f) = \int_{\mathscr{H}/\Gamma} k_f(z,z)dA(z), \tag{16}$$

and on the other hand if we are given the eigenvalues $\{\kappa_j\}$ of the operator K_f, we can express the trace as

$$\mathrm{Tr}(K_f) = \sum_j \kappa_j. \tag{17}$$

3 The Selberg trace formula

Assume that the quotient Riemann surface $S = \mathscr{H}/\Gamma$ is compact and smooth, i. e., the discrete group Γ contains only hyperbolic elements. Recall that closed geodesics of $S = \mathscr{H}/\Gamma$ correspond to conjugacy classes of hyperbolic elements in the subgroup. Now, we can compute the trace of the operator K_f in terms of the length of the closed geodesics of the surface S. Assume that $L(\Gamma) := \{l(g)|g \in \Pi\}$ where Π is the set of hyperbolic conjugacy classes. Using the decomposition of the group in terms of the different types of conjugacy classes (hyperbolic, elliptic or parabolic) and after computation, the following formula for the trace of the operator K_f is obtained

$$\mathrm{Tr}(K_f) = f(0)\mathrm{Vol}(\mathscr{H}/\Gamma)+ \sum_{l\in\Gamma}\sum_{n\in\mathbb{N}} \frac{1}{\sinh(\frac{kl}{2})}\int_{kl}^{\infty} \frac{f(\cosh t)}{\sqrt{2\cosh t - 2\cosh kl}}\sinh t dt. \tag{18}$$

Also from the spectral side we have

$$\mathrm{Tr}(K_f) = \sum_{j=0}^{\infty} h(\sqrt{\lambda_j - \frac{1}{4}}), \tag{19}$$

where h is an appropriate function and after simplification the Selberg trace formula for the compact quotient case takes the following form: group in terms of the different types of conjugacy classes (hyperbolic, elliptic or parabolic) and after computation, we obtain the following formula for the trace of the operator K_f:

$$\sum_{j=0}^{\infty} h(\sqrt{\lambda_j - \frac{1}{4}}) = \frac{\mathrm{Vol}(\mathscr{H}/\Gamma)}{4\pi}\int_{-\infty}^{\infty} rh(r)\tanh(\pi r)dr + \sum_{l\in L(\Gamma)}\sum_{k\in\mathbb{N}} \frac{1}{\sinh(\frac{kl}{2})}\hat{h}(kl), \tag{20}$$

where $\hat{h}$ is the Fourier transform of the function h. It is noteworthy that the first term on the right hand side constitutes a topological term. This trace formula can be considered as a natural generalization of the Poisson summation formula.

4 The formula for the non-compact case

In the non compact case, the Selberg trace formula becomes more intricate due to the fact that the operator K_f is no longer a trace class operator. Consequently, new terms and integrals corresponding to elliptic and parabolic elements emerge. Notably, on the spectral side, scattering terms related to cusp points appear, transforming this side of the trace formula as follows:

$$\sum_{j=0}^{\infty} h(\sqrt{\lambda_j - \frac{1}{4}}) - \frac{1}{2\pi}\int_{-\infty}^{\infty} \frac{\phi'}{\phi}(\frac{1}{2}+ir)h(r)dr + \frac{1}{2}h(0)\mathrm{Tr}[\phi_{ij}(\frac{1}{2})], \tag{21}$$

where $\phi_{ij}(s)$ denotes the scattering matrix and $\phi(s) = \det[\phi_{ij}(s)]$. Similarly, on the length side, additional terms corresponding to elliptic and parabolic points are introduced, in addition to the previously mentioned term corresponding to hyperbolic elements as observed in the compact quotient case. For each elliptic element in the group, the following terms should be added

$$\sum_{j=1}^{n-1} \frac{1}{n\sin(\frac{\pi j}{n})}\int_{-\infty}^{\infty} \frac{e^{-\frac{2\pi jr}{n}}}{1-e^{-2\pi r}}h(r)dr, \tag{22}$$

where n is the order of the elliptic fixed point.

In the end, for a non-compact Riemann surface $\mathscr{H}/\Gamma$ like the group $\Gamma = SL(2,\mathbb{Z})$, with finite volume, the Selberg trace formula acquires additional terms and is as follows:

$$\begin{aligned}
&\sum_{j=0}^{\infty} h(r_j) - \frac{1}{4\pi}\int_{-\infty}^{\infty} \frac{\phi'}{\phi}\left(\frac{1}{2}+ir\right)h(r)\,dr \\
&\quad + \frac{1}{4}h(0)\mathrm{tr}\,\phi\left(\frac{1}{2}\right) \\
&= \frac{\mathrm{Vol}(\mathscr{F})}{4\pi}\int_{-\infty}^{\infty} rh(r)\tanh(\pi r)\,dr \\
&\quad + \sum_{\{\gamma\}}\sum_{k=1}^{\infty} \frac{l_\gamma}{2\sinh(kl_\gamma/2)}\hat{h}(kl_\gamma) \\
&\quad + \frac{1}{4}h(0) - \frac{\ln 2}{2\pi}\hat{h}(0) \\
&\quad + \sum_{\{R\}} \frac{1}{2m_R\sin(\pi/m_R)}\int_{-\infty}^{\infty} \frac{e^{-2\pi r/m_R}}{1+e^{-2\pi r}}h(r)\,dr.
\end{aligned} \tag{23}$$

Here, $\lambda_j = \frac{1}{4} + r_j^2$ are Laplacian eigenvalues, $\phi(s)$ is the scattering matrix determinant, $\{\gamma\}$ are primitive hyperbolic conjugacy classes (lengths l_γ), $\{R\}$ are elliptic conjugacy classes (orders m_R), and $\hat{h}$ is the Fourier transform of h.

5 Selberg Zeta function

One of the primary applications of the Selberg trace formula is the proof of the meromorphic continuation of a crucial zeta function known as the Selberg zeta function. The Selberg zeta function for Γ is defined as

$$Z_\Gamma(s) = \prod_{\{\gamma\}} \prod_{k=0}^{\infty} \left(1 - e^{-(s+k)l_\gamma}\right), \tag{24}$$

It satisfies the functional equation

$$\begin{aligned} Z_\Gamma(s) =& Z_\Gamma(1-s) \\ &\times \exp\left(\frac{\mathrm{Vol}(\mathscr{H}/\Gamma)}{2\pi} \int_0^{s-1/2} r\tan(\pi r)dr\right). \end{aligned} \tag{25}$$

The zeros occur at

- $s = \frac{1}{2} \pm ir_j$ (spectral zeros).
- $s = -k$, $k \in \mathbb{N}$ (trivial zeros).

One can also observe that the above product converges for $\mathrm{Re}(s) = 1$. It can be demonstrated using the trace formula that the Selberg zeta function can be analytically continued to the entire complex plane. The zeros of the Selberg zeta functions correspond to the eigenvalues of the hyperbolic Laplacian.

It would be intriguing to dissect the simple closed geodesics among all closed geodesics. For instance, if we modify the definition of the Selberg zeta function for a Riemann surface by multiplying over all simple closed geodesics, the resulting zeta function raises pertinent questions about which properties of the ordinary Selberg zeta function can induce this modified zeta function? For instance, can we extend the analytic continuation of this modified Selberg zeta function over the complex plane? Similarly, investigating the functional equation and the corresponding Riemann hypothesis holds potential. It may be worthwhile to devise a method and adapt the renowned Selberg trace formula for simple closed geodesics. This modified trace formula could then be employed to obtain the analytic continuation of the modified Selberg zeta function. Another interesting property of hyperbolic surfaces is the ergodicity of their geodesic flow. This implies that every function on the hyperbolic surface that is invariant under the geodesic flow must be a constant function. This type of ergodicity is called classical ergodicity. However, there exists a broader notion of ergodicity. Quantum ergodicity is another notion of ergodicity that holds significant importance in quantum chaos. Notably, early numerical simulations in chaotic billiards revealed intriguing phenomena involving highly excited quantum particles concentrating on periodic trajectories corresponding to classical particles. Quantum ergodicity is formally defined in terms of the Laplace eigenfunctions on a domain or, more generally, a surface or manifold. For each eigenfunction Φ_j we can associate a probability measure

$$\nu_j = |\Phi_j|^2 dA. \tag{26}$$

A central and intriguing conjecture in this research area, which now has been established as a theorem for a specific set of surfaces, points that the probability measures j converge to the Liouville measure on the unit tangent bundle of the corresponding Riemann surface. This phenomenon is referred to as quantum unique ergodicity (QUE), as discussed in [5]. For general compact manifolds with ergodic geodesic flow, it is known that for numerous choices of subsequences of eigenfunctions, the corresponding limits of the probability measures exist and are equal to the Liouville measure on the manifold (as detailed in [6]). However, this property does not hold for all sequences.

Another conjecture about the modular surface is that the simple closed geodesics on this special surface is simple, meaning that their multiplicity is 1 in the length spectrum. Through a well-known argument, it can be deduced that the corresponding quadratic forms possess class number one (according to the correspondence between closed geodesics and indefinite quadratic forms). We believe that the Selberg trace formula and Selberg zeta function are tools that will assist us in addressing the following problem. Let $K = \mathbb{Q}(\sqrt{d})$ be a real quadratic field and $\mathscr{O}_K$ be its ring of integers. The discrete group $\Gamma_K = PSL(2, \mathscr{O}_K)$ acts on the upper half plane, and we can consider the quotient surface $S = \mathscr{H}/\Gamma_K$. How is the geometry of this surface related to the arithmetic of the real quadratic number field K, such as class numbers and fundamental units, etc to the closed geodesics and spectrum of the surface S? We can also pose the same question for the complex surface (called Hilbert modular surface of dimension 2) $M = \mathscr{H} \times \mathscr{H}/\Gamma_K$. It is noteworthy that, according to a theorem by Siegel, the volume of the Hilbert modular surface is, in fact, the value of the Dedekind zeta function of the quadratic field K at -1. Another property is that the number of the cusps of the surface is equal to the class number of the number field K. Consequently, Gauss conjecture is equivalent to the following statement: There exist infinitely many

modular surfaces M_K that possess only a single cusp under the action of the discrete group $\Gamma_K = PSL(2, \mathcal{O}_K)$. These inquiries are of interest and can be subject to investigation.

6 Conclusion

The Selberg trace formula presented above reveals that the left-hand side of the formula is solely dependent on the spectral parameters (eigenvalues of the Laplace operator), which corresponds to the modes or frequencies of the surface. These parameters are quantum mechanical entities. Conversely, the right hand side of the trace formula is dependent solely on the length spectrum, which are the classical mechanical parameters of the underlying universe (our surface). In essence, the left hand side of the trace formula resides within the realm of quantum physics, while the right hand side belongs to classical mechanics. In conclusion, this note also posed several intriguing questions relating the structure of the real quadratic fields to the geometry of the corresponding modular surfaces. Understanding these relationships may provide insights into the Gauss conjecture for class numbers of the real quadratic fields.

Acknowledgements This research was partially supported by a grant from IPM (No. 1404110116). The author would like to express his gratitude to the Institute for Research in Fundamental Sciences (IPM) in Tehran for its hospitality during the preparation of this report on the Selberg trace formula. Furthermore, the author would like to express his gratitude to the INSF for providing grant number 4000296.

References

1. A. Selberg, J. Indian Math. Soc. **20**, (1956)
2. P. Buser, *Geometry and spectra of compact Riemann surfaces*, Birkhauser Publication, (1992)
3. D. Hejhal, *The Selberg trace formula for PSL*$(2,\mathbb{R})$, Springer Verlag Publication, (1976)
4. S. Sarnak, Bull. Am. Math. Soc. **40**, (2003)
5. E. Lindenstrauss, Ann. Math. **163**, (2006)
6. S. Zelditch, *Quantum ergodicity and mixing of eigenfunctions,* Encyclopedia of mathematical physics, Oxford, Vol. 1-5, (2006)

TTMP vol 2 (2), 2025
doi: 10.30511/TTMP.2025.2058927.1052

Transactions in Theoretical and Mathematical Physics

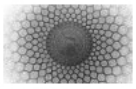

Quantum acoustics: Investigation of phonons, their physical properties, and interactions with quantum systems

Bahareh KhishKhah[b,1], **Reza Sharifian**[a,1], **Mohammad Fatemi Mofrad**[1], **Hadiseh Sadri**[1], **Sadighi-Bonabi Rasoul**[a,1]

[1]Department of Physics, Sharif University of Technology, Iran

Received: 25 April 2025 / Accepted: 27 May 2025 / Published: 27 May 2025

Abstract Phonons, as quantum quasiparticles representing collective vibrations in crystal lattices, play a fundamental role in understanding the physical properties of solid materials. This article explores the physical foundations of phonons, including their types (acoustic and optical phonons), dispersion relations, and the influence of effective mass on their propagation. It further examines the interaction of phonons with quantum systems, such as their coupling to superconducting qubits, their role in quantum information transfer, and their application in quantum memories. Additionally, cutting-edge quantum acoustics technologies are discussed, including bulk acoustic wave (BAW) and surface acoustic wave (SAW) propagation, the piezoelectric effect in phonon generation and control, and phononic waveguides. The final section addresses technical challenges and future research directions in quantum acoustics, analyzing the potential of this field for advancing quantum information processing and emerging technologies.

1 Introduction

Quantum acoustics, as an emerging branch of modern quantum physics, focuses on studying the quantum behavior of mechanical waves and their interactions with quantum systems, opening new frontiers in quantum engineering and information technologies. This field leverages fundamental concepts of phonons (quanta of lattice vibrations in solids) to explore quantum phenomena such as entanglement, superposition, and quantum information transfer in acoustic systems [1]. Surface acoustic waves (SAWs) and bulk acoustic waves (BAWs) serve as key tools in this domain, enabling low-loss, controlled-speed transmission of quantum information (Fig. 1). Recent studies have demonstrated that these waves can bridge superconducting Josephson-junction qubits and semiconductor quantum dots, paving the way for hybrid quantum processing architectures [2].

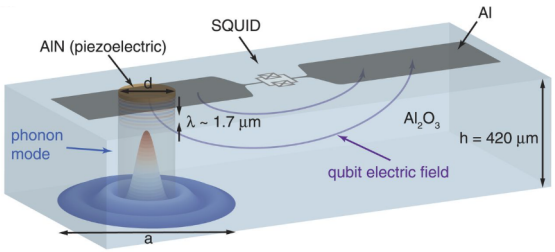

Fig. 1 Schematic of a piezoelectric coupling to modes of a high-overtone bulk acoustic resonator (HBAR) (not to scale). The longitudinal wavefunction component is depicted as a sinusoidal profile with wavelength $\lambda = 2h/l$ across the cylindrical mode volume defined by an AlN disk and a sapphire substrate. The transverse energy density profile $s_{l,0}(x/v)$ is rendered in 3D, illustrating effective energy confinement within the mode volume while accounting for diffraction-induced leakage. This also shows that the $s_{l,0}(x/v)$ mode is equivalent to the $s'_{l,3}(x/v)$ mode in a larger volume with diameter a [3].

A milestone in quantum acoustics was the achievement of coherent quantum state transfer between physically separated nodes, realized in 2022 using an advanced unidirectional piezoelectric transducer. These experiments employed single-phonon transmission over 2-mm channels with a propagation time of 500 ns, highlighting the scalability potential for quantum architectures. These advances relied on low-loss (<0.1 dB/cm) phononic waveguides with coherence times of ∼2.2 μs [4]. Meanwhile, recent theoretical studies on non-Markovian phonon-qubit dynamics have provided new insights into decoherence mechanisms and mitigation strategies. For instance, in lithium niobate systems, engineered phonon anisotropy reduced thermal noise by 40% at 10 mK [3].

[a]e-mail: sadighi@sharif.edu
[b]e-mail: bahareh.khishkhah@physics.sharif.edu

Technical challenges in this field primarily stem from surface phonon scattering and environmental factors like thermal fluctuations. Researchers have optimized hybrid piezo-optomechanical structures, achieving strong coupling (>1 MHz) between microwave phonons and optical photons, a key step toward quantum frequency converters. In 2024, a breakthrough experiment using phononic metamaterials demonstrated squeezed quantum states in acoustic waves, enabling ultra-sensitive quantum sensors [5].

Future directions include integrated quantum acoustic networks interfacing with optical and microwave processors. Early studies on time-periodic phononic crystals have shown dynamic control over phonon propagation via geometric modulation, potentially enabling all-acoustic quantum logic gates. Additionally, discoveries of collective quantum effects (e.g., Majorana-like quasiparticles in acoustic chains) are expanding topological quantum research.

Practically, quantum acoustic systems are increasingly used in quantum memories with storage times exceeding 10 ms. A recent innovation employed high-Q (10^6) acousto-optic cavities to store and retrieve single-photon states with 85% efficiency [6]. These advances, combined with phononic cooling techniques reaching sub-millikelvin temperatures, are accelerating the development of scalable quantum systems.

2 Foundations of Quantum Acoustics: Mathematical Analysis and Quantum Interactions

Quantum acoustics systematically studies the quantum behavior of mechanical waves in material media, where energy scales become sufficiently small that quantum effects such as superposition, entanglement, and projective measurements dominate the system's dynamics. The theoretical core of this field is based on the quantization of acoustic fields and non-classical interactions between phonons and other qubits. The classical wave equation in homogeneous elastic media is expressed as [7]:

$$\frac{\partial^2 \psi(\mathbf{r},t)}{\partial t^2} = v^2 \nabla^2 \psi(\mathbf{r},t), \tag{1}$$

where ψ represents particle displacement, v is the speed of sound, and ∇^2 is the Laplacian operator. For quantum description, this equation must be rewritten using secondary quantization methods. By introducing phonon creation ($b_k^\dagger$) and annihilation (b_k) operators, the displacement field is quantized as:

$$\hat{\psi}(\mathbf{r},t) = \sum_k \sqrt{\frac{\hbar}{2\rho V \omega_k}} \left(b_k e^{i(\mathbf{k}\cdot\mathbf{r}-\omega_k t)} + b_k^\dagger e^{-i(\mathbf{k}\cdot\mathbf{r}-\omega_k t)} \right). \tag{2}$$

Here, ρ is the medium density, V is the system volume, $\omega_k = v|\mathbf{k}|$ is the acoustic phonon dispersion relation, and $\mathbf{k}$ is the wave vector. This formulation shows that phonons behave as massless quantum particles with energy $E_k = \hbar\omega_k$ and momentum $\mathbf{p} = \hbar\mathbf{k}$ [8].

At low temperatures (below 100 mK), phonons follow Bose-Einstein statistics, with density of states given by $g(\omega) = \frac{V\omega^2}{2\pi^2 v^3}$. Under such conditions, quantum effects like phononic squeezed states, which reduce quantum fluctuations in one phase component, become observable. These states are generated using squeeze operators $S(\zeta) = \exp\left(\frac{1}{2}\zeta^* b^2 - \frac{1}{2}\zeta (b^\dagger)^2\right)$, where $\zeta = re^{i\theta}$ is the squeezing parameter.

Photon-phonon interactions in piezoelectric materials are modeled using quantum elasticity theory and Maxwell's equations. In these materials, mechanical stress (σ_{ij}) and electric field (E_k) are coupled through piezoelectric coefficients (e_{ijk}) [9]:

$$\sigma_{ij} = c_{ijkl}\varepsilon_{kl} - e_{kij}E_k, \tag{3}$$

$$D_i = e_{ikl}\varepsilon_{kl} + \varepsilon_{ij}E_j, \tag{4}$$

where c_{ijkl} is the elasticity tensor, ε_{kl} the strain tensor, and ε_{ij} the permittivity tensor. At the quantum level, these interactions are described by an extended Jaynes-Cummings Hamiltonian:

$$H = \hbar\omega_c a^\dagger a + \hbar\Omega_m b^\dagger b + \hbar g_0 a^\dagger a (b + b^\dagger) + \hbar J (a^\dagger b + a b^\dagger). \tag{5}$$

The first two terms represent cavity photons (frequency ω_c) and mechanical phonons (frequency Ω_m), respectively. The third term (linear electromechanical coupling, strength g_0) and fourth term (nonlinear coupling, strength J) describe energy transfer between the systems. Recent experiments on lithium niobate platforms measured $g_0/2\pi \sim 10 - 100$ kHz and $J/2\pi \sim 1 - 10$ kHz, demonstrating their strong potential for quantum processing.

A key challenge in quantum acoustics is managing decoherence from phonon-environment interactions. Surface acoustic wave (SAW) phonon decoherence rates are estimated by:

$$\Gamma_\phi = \frac{k_B T \omega_m^2}{Q_m \hbar \Omega_m}, \tag{6}$$

where Q_m is mechanical quality factor, T temperature, and Ω_m mechanical frequency. Below 20 mK with $Q_m > 10^6$, de-

coherence rates fall below 100 Hz, enabling coherence times of ∼10 ms.

Quantum information transfer via phonons requires a low-loss waveguide design. Phonon propagation in acoustic waveguides follows:

$$\frac{\partial \hat{b}(x,t)}{\partial t} = -v_g \frac{\partial \hat{b}(x,t)}{\partial x} - \frac{\kappa}{2}\hat{b}(x,t) + \sqrt{\kappa}\hat{b}_{in}(t), \tag{7}$$

where v_g is phonon group velocity, κ loss rate, and $\hat{b}_{in}$ the input operator. For $> 90\%$ transfer efficiency, the condition $\kappa L/v_g \ll 1$ must hold, recently achieved in gallium arsenide (GaAs) waveguides with $L = 2$ mm and $\kappa/2\pi = 50$ Hz.

Nonlinear effects in quantum acoustics, like phonon-phonon interactions, are described by [10]:

$$H_{nonlinear} = \hbar\chi(b^\dagger)^2 b^2, \tag{8}$$

where χ is the nonlinear coefficient. These effects are observable in highly anisotropic materials (e.g., diamond), enabling phononic squeezed states and multiphonon entanglement. In 2023, silicon nanoparticle experiments reported nonlinear interactions with $\chi/2\pi \sim 1$ kHz, paving the way for all-acoustic quantum gates.

3 Phonons and Their Properties

Phonons are fundamental quantum mechanical concepts in solid-state physics that describe collective atomic vibrations in crystalline lattices. When atoms in a solid are at their equilibrium positions, the crystal lattice is stable. However, mechanical disturbances propagate as waves through the material. While macroscopically these are sound waves, at microscopic quantum scales, they are quantized waves called phonons. Essentially, phonons are the mechanical analogs of photons in electromagnetism and play vital roles in materials' thermodynamic and electrical properties [7].

A key aspect of phonons is their influence on thermal conductivity. In insulators where heat transfer occurs primarily through phonons, understanding their dynamics enables precise descriptions of thermal behavior. Phonon-electron interactions also critically determine electrical and thermoelectric properties. For instance, in superconductors, phonon-electron coupling creates the superconducting phase where electrical resistance vanishes.

In crystalline structures, atoms are connected by electrostatic forces. When displaced, this motion propagates through interatomic forces as vibrational waves throughout the lattice. These waves, influenced by the material's mechanical and crystalline properties, form different phonon types.

Phonons are categorized as either **acoustic** or **optical**. Acoustic phonons exist in all solids and involve in-phase atomic oscillations, propagating near the material's sound speed. They facilitate mechanical and thermal energy transfer and are subdivided into longitudinal (atomic motion parallel to wave propagation) and transverse (perpendicular motion) modes [11].

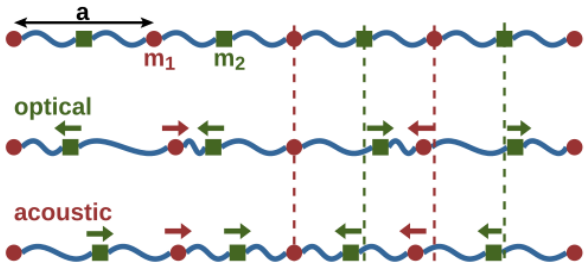

Fig. 2 Schematic of crystal lattice showing acoustic and optical phonon propagation

Optical phonons primarily occur in crystals with multiple atom types per unit cell, where atoms oscillate out of phase. This enables strong interactions with electromagnetic waves, particularly in infrared and ultraviolet regions, significantly impacting optical properties through phenomena like Raman scattering and infrared absorption. Like acoustic phonons, optical phonons have longitudinal and transverse variants (Fig. 2).

The phonon dispersion relation – describing how frequency (ω) depends on wavenumber (k) – is crucial for understanding phonon behavior. This relation is nearly linear for acoustic phonons at long wavelengths ($omega \propto k$), resembling sound waves in continuous media. At higher frequencies, crystal symmetries and interatomic interactions introduce nonlinearities.

Unlike acoustic phonons, optical phonons typically exhibit nonlinear dispersion, maintaining nearly constant frequencies at small wavenumbers because their vibrational energy depends on unit cell structural changes rather than wavenumber. Consequently, optical phonons have higher frequencies (often several THz) than acoustic phonons (Fig. 3).

Atomic mass significantly influences phonon properties. In heavier elements, higher effective phonon masses reduce wave propagation speeds, directly lowering thermal conductivity since slower phonons transfer less heat (Fig. 4).

Phonon interactions with other quantum particles are research hotspots. Phonon-photon interactions occur in Raman scattering and photoelastic effects, while phonon-electron coupling enables phenomena like electron-phonon scattering and superconductivity. In quantum systems, phonons can mediate qubit coupling for quantum information transfer.

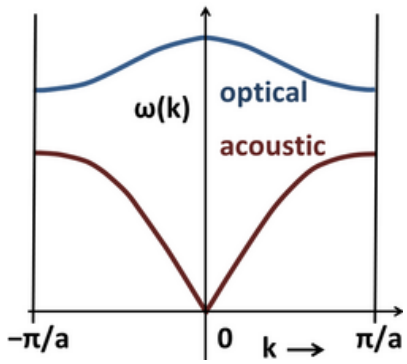

Fig. 3 Dispersion curves for acoustic and optical phonons in a linear diatomic chain

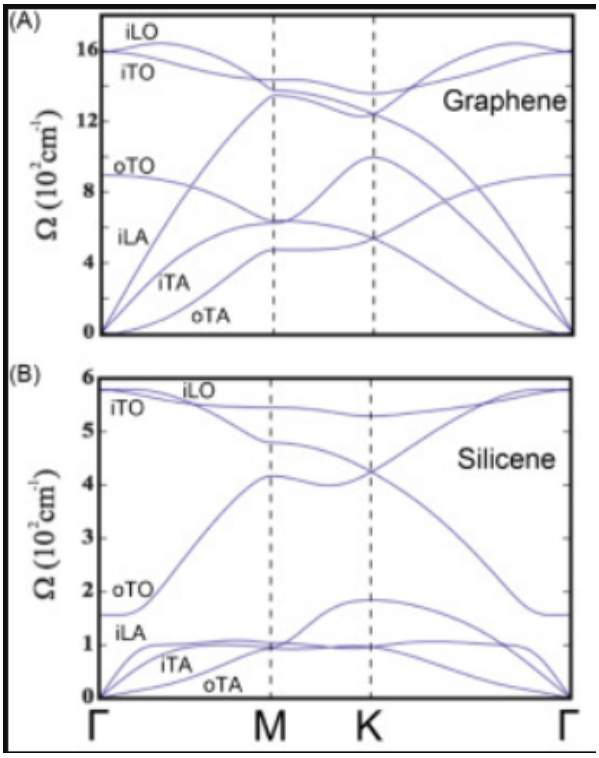

Fig. 4 Vibrational properties of silicene and graphene: (A-B) Calculated phonon dispersion with labeled modes (i: in-plane, o: out-of-plane, A: acoustic, O: optical, L: longitudinal, T: transverse) [4]

Overall, phonons are essential for understanding solid-state physics across thermodynamics, optics, electronics, and quantum computing. Recent research on phononic engineering and controlled phonon guidance structures highlights their potential for developing quantum information technologies and ultra-sensitive mechanical sensors [8, 12].

4 Interaction of Phonons with Quantum Systems

Phonons play a crucial role as quantum information carriers in the development of quantum processing and quantum communications. Unlike photons that propagate in vacuum, phonons are dependent on material media, yet this characteristic makes them particularly suitable for certain specialized applications. In some systems, phonons can serve as efficient mediators for quantum information transfer due to their long coherence times and low loss. In systems based on superconducting qubits and quantum dots, surface acoustic waves (SAWs) and bulk acoustic waves (BAWs) have been proposed for establishing connections between different components of a quantum circuit. The propagation of single-mode phonons in a controlled environment enables coherent quantum information transfer, a feature of paramount importance for establishing quantum networks [9, 11].

In quantum information processing, phonons can be engineered through various approaches. One of their most significant capabilities in this domain is their use in creating single-mode phononic states. In this method, individual phonons are generated and controlled in specific media, enabling quantum information storage and processing. In certain materials, phonons can preserve information for extended periods, making them excellent candidates for constructing quantum memories. Phononic quantum memories can serve as intermediaries for information exchange between different sections of a quantum processor, ensuring the prolonged stability of quantum information.

One of the most important interactions of phonons in quantum physics is their coupling with superconducting qubits (Fig. 5). Superconducting qubits are typically controlled through electromagnetic fields, but their interaction with phonons can also be achieved via the piezoelectric effect. In this interaction, phonon energy can induce qubit state transitions, and conversely, qubits can generate or absorb phonons. This coupling is described by various theoretical models, including the Jaynes-Cummings Hamiltonian:

$$H = \hbar\omega_q \sigma^+\sigma^- + \hbar\omega_p a^\dagger a + \hbar g(\sigma^+ a + \sigma^- a^\dagger), \tag{9}$$

where ω_q is the qubit frequency, ω_p the phonon frequency, $a^\dagger$ (a) are phonon creation (annihilation) operators, $\sigma^\pm$ are qubit raising/lowering operators, and g is the coupling strength [8, 13].

This model demonstrates that a superconducting qubit can change states by absorbing or emitting a phonon. Such phenomena provide a foundation for developing phonon-based quantum circuits where quantum information is stored and processed in qubits and phonons. The interaction between phonons and superconducting qubits also plays a role in developing quantum sensors. Due to phonons' sensitivity to environmental changes, they can be used to detect extremely weak mechanical fields, potentially leading to the development of ultra-precise sensors for measuring faint forces and structural changes in materials.

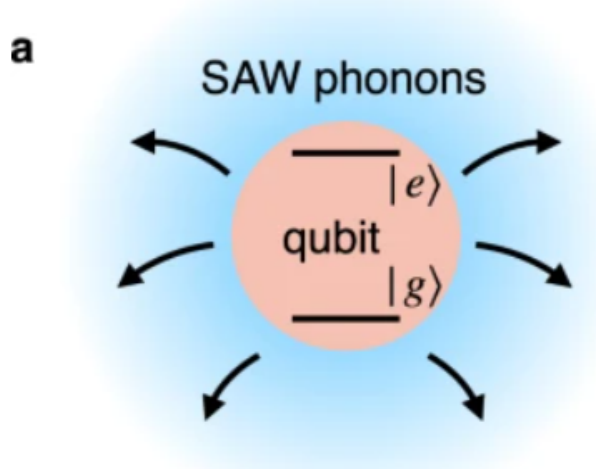

Fig. 5 Schematic diagram illustrating the coupling of a qubit to a SAW phonon bath: The qubit (orange-pink) non-uniquely emits excitations to the SAW phonon bath (blue), with the emission rate regulated by the SAW structure's electrical conductivity [14].

In summary, phonons offer unique capabilities for quantum information processing and transfer. While photons remain the primary mediators for quantum communications, phonons – with their stronger interaction with solid-state environments and ability to couple with mechanical and electronic systems – represent an exceptionally suitable platform for advancing quantum technologies. The integration of these characteristics with emerging phonon control and engineering techniques may open new pathways in quantum computing and sensing [15].

5 Quantum Acoustics-Based Technologies

Quantum acoustics, as an interdisciplinary field combining quantum mechanics and acoustic physics, encompasses technologies that utilize quantized sound waves (phonons) for information transfer and processing. These technologies are primarily categorized into three main areas: acoustic wave propagation, phonon control and generation via the piezoelectric effect, and phononic waveguides.

Acoustic waves propagating in solid materials are broadly classified into bulk acoustic waves (BAW) and surface acoustic waves (SAW). In BAW, acoustic vibrations propagate throughout the material volume and can be guided along specific paths depending on boundary conditions and material structure. Due to their deep penetration, BAWs are commonly used in high-precision sensors and quantum communication systems. In contrast, SAWs propagate only along surface layers and remain concentrated near the surface. This property gives SAWs high sensitivity to surface changes, making them suitable for frequency filters, precision sensors, and as quantum system interconnects in quantum communications [7, 8, 13].

One of the most important methods for phonon control and generation in quantum acoustics is the piezoelectric effect (Fig. 6). Observed in materials like aluminum nitride, quartz, and certain ceramics, this effect generates an electric field under mechanical stress and vice versa - applying an electric field induces mechanical deformation. This property enables precise phonon control and acoustic wave generation in solids. For example, applying alternating voltage to a piezoelectric material produces acoustic waves at specific frequencies that can guide, store, or transfer quantum information. This technology plays a key role in manufacturing quantum chips, requiring precise phononic wave control.

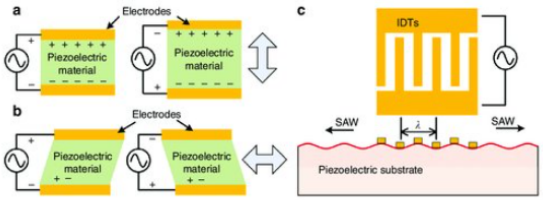

Fig. 6 Acoustic wave generation via piezoelectric materials. a) Applying voltage to electrodes causes thickness-mode vibrations (perpendicular expansion/contraction). b) For certain material orientations, applied voltage induces shear-mode vibrations (horizontal deformation). c) Interdigital transducers (IDTs) on piezoelectric crystals generate surface acoustic waves (SAWs) with wavelength (λ) determined by IDT finger spacing [16].

Phononic waveguides represent another crucial quantum acoustics technology enabling controlled phonon propagation (Fig. 7). Similar to optical waveguides in photonics, specially designed structures can guide phononic waves along predetermined paths. These waveguides are typically created by locally modifying mechanical properties like density or stiffness. Their key advantage is enabling phonon path control without external fields - essential for designing phonon-based quantum circuits [7, 17].

6 Practical Applications of Quantum Acoustics

With advancements in quantum acoustics technologies, the use of phonons for quantum information transfer has become one of the most important applications in this field (Fig. 7). While many quantum systems use photons for information transfer, phonons have emerged as a superior alternative for certain systems due to their lower environmental sensitivity and more precise controllability. In some systems, quantum qubits based on electronic states can interact with phonons, enabling information transfer between different components of a quantum processor. This capability is

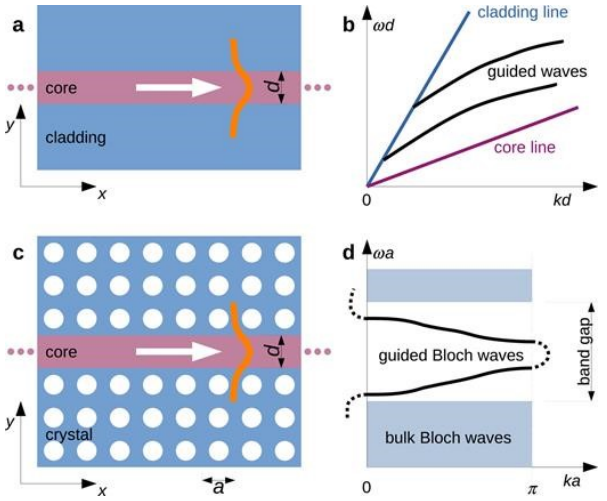

Fig. 7 Waveguide principles. a) Homogeneous waveguides contain a core and cladding. When the wave velocity is lower in the core, waves propagate in the core while being evanescent in the cladding. b) Dispersion of guided waves between two sound lines (core and cladding). c) In phononic crystal waveguides, the cladding is replaced by a complete bandgap phononic crystal. d) Being periodic along its axis, the phononic crystal waveguide exhibits folded dispersion bands within bandgaps, defined for Bloch wavenumbers in the first Brillouin zone [18].

particularly valuable for technologies requiring communication between superconducting qubits.

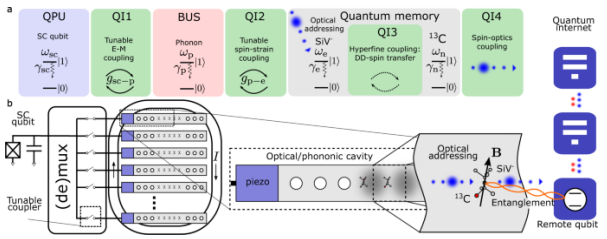

Fig. 8 (a) A superconducting quantum processing unit (QPU) connects to a phononic bus via piezoelectric "Quantum Interface 1" (QI1). The phonon couples with electron spin-orbit states of an active center (AA), forming "Quantum Interface 2" (QI2). The active center's microstructure states can further couple with nuclear spins via "Quantum Interface 3" (QI3) to form a quantum memory (QM), or connect to photons through "Quantum Interface 4" (QI4), ultimately linking to the quantum internet (blue dots: optical connections). (b) Implementation shows a superconducting qubit connected via phononic/microwave multiplexers to waveguide arrays, each interacting with mechanical cavities hosting active centers (AA). These centers' electron spin-orbit states serve as qubits, hyperfine-coupled to adjacent carbon-13 nuclear spins for high-coherence auxiliary qubits. Optical transitions provide quantum network interfaces through electron-photon spin entanglement protocols. This architecture utilizes: tunable electromechanical qubit-cavity coupling, tunable spin-strain coupling, optical spin addressing, and hyperfine coupling for nuclear quantum memory [19].

Another emerging application is phonon-based quantum memory. A major challenge in quantum computing is maintaining quantum coherence over extended periods. Phonons, with their weaker environmental interactions compared to photons and other quantum information carriers, can serve as quantum memory in certain systems. These memories utilize controlled mechanical oscillations created by phonons in materials, enabling longer-duration quantum information storage [1, 13, 15].

Quantum acoustics also enables the detection of acoustic waves at quantum levels. Phonon-sensitive systems, often based on superconducting qubits or other quantum sensors, can detect extremely weak mechanical vibrations. This has important applications in seismology, material defect detection, and even gravitational wave research [14, 17].

7 Future Prospects and Challenges

Quantum acoustics, while possessing transformative potential, faces several hurdles that must be addressed to realize its full capabilities. A primary challenge lies in the inherent difficulty of achieving precise control over phonons. Unlike photons, which propagate freely through a vacuum, phonons are intrinsically tied to the material media through which they travel. This dependence on the medium complicates their manipulation and control, adding a layer of complexity not present in photonic systems. Furthermore, the delicate nature of phonons makes them susceptible to environmental noise. Unexpected interactions with the surrounding environment can induce phonon decoherence, a process that leads to the degradation and eventual loss of the quantum information encoded within the phonons. This decoherence poses a significant obstacle to the development of robust quantum acoustic devices.

Another significant challenge stems from the experimental limitations that currently constrain our ability to generate and detect single phonons with high fidelity. While substantial progress has been made in recent years, achieving complete and reliable control over individual phonons remains an ongoing pursuit. Overcoming this limitation requires the development and refinement of advanced technologies, including improved piezoelectric devices capable of efficiently converting electrical signals into acoustic waves, sophisticated nanostructures designed to guide and manipulate phonons at the nanoscale, and highly sensitive quantum sensors capable of detecting individual phonons with minimal disturbance. Continued advancements in these areas are crucial for unlocking the full potential of quantum acoustics.

Despite these existing challenges, quantum acoustics offers immense promise for revolutionizing the field of quantum information processing. By leveraging the unique properties of phonons, researchers hope to develop more stable and efficient quantum information systems that surpass the limitations of current technologies. The true potential of

quantum acoustics is likely to be realized through its synergistic integration with other quantum technologies, creating hybrid quantum systems that combine the strengths of different physical platforms. Future progress in the field will likely be driven by focused research efforts aimed at elucidating the intricate interactions between phonons and other quantum components, designing and fabricating integrated acoustic circuits capable of performing complex quantum operations, and developing improved phononic sensors with enhanced sensitivity and precision [4, 9, 10, 12, 14].

The ongoing research efforts in quantum acoustics, particularly when considered within the broader context of other domains of quantum physics, hold the potential to yield groundbreaking discoveries that could transform various aspects of our lives. These advancements may lead to breakthroughs in quantum communications, enabling secure and ultra-fast data transmission; quantum computing, paving the way for solving currently intractable computational problems; and ultra-sensitive sensing, allowing for the detection of minute changes in the environment with unprecedented accuracy. Ultimately, the continued exploration and development of quantum acoustics may unlock entirely new pathways for scientific and technological advancement, leading to innovations that were previously unimaginable [11, 20–22].

As part of our future research endeavors, we plan to dedicate our efforts to investigating the seamless integration of quantum acoustic systems with photoacoustic imaging [3, 14, 16, 17, 22, 23] platforms. Our primary focus will be on enhancing the overall image quality achievable through this integration, with a particular emphasis on leveraging phonon-based quantum sensing techniques to improve sensitivity and resolution. Furthermore, we will explore the application of sophisticated phononic circuit engineering principles to optimize the performance of the integrated imaging system, aiming to develop a powerful and versatile tool for a wide range of applications.

References

1. É. Dumur, K. J. Satzinger, G. A. Peairs, M.-H. Chou, A. Bienfait, H.-S. Chang, A. N. Cleland, Npj Quant. Inf. **7**, (2021)
2. M. V. Gustafsson, Nature Phys. **18**, (2022)
3. Y. Chu, P. Kharel, W. H. Renninger, L. D. Burkhart, L. Frunzio, P. T. Rakich, R. J. Schoelkopf, Science **358**, (2017)
4. J. Zhang, Phys. Rev. Lett. **15**, (2023)
5. A. Blais, A. L. Grimsmo, S. M. Girvin, A. Wallraff, Rev. Mod. Phys. **93**, (2021)
6. A. H. Safavi-Naeini, O. Painter, New J. Phys. **13**, (2011)
7. K. Kuruma, Nature Phys. **1**, (2024)
8. K. J. Satzinger, Appl. Phys. Lett. **18**, (2023)
9. L. R. Sletten, Phys. Rev. B **107**, (2023)
10. J.-J. Xue, W.-Q. Zhu, Y.-N. He, X. Wang, H.-R. Li, Quantum Inf. Process. **19**, (2020)
11. M. Kervinen, I. Rissanen, M. A. Sillanpää, Phys. Rev. Lett. **128**, (2022)
12. A. Pontin, M. Bonaldi, A. Borrielli, L. Marconi, F. Marin, F. Marino, L. Conti, Phys. Rev. Lett. **116**, (2016)
13. H. M. I. Hassan, N. F. F. Areed, H. A. El-Mikati, M. F. O. Hameed, S. S. A. Obayya, Opt. Quantum Electron. **54**, (2022)
14. J. D. Teufel, T. Donner, D. Li, J. W. Harlow, M. S. Allman, K. Cicak, R. W. Simmonds, Nature **475**, (2011)
15. G. T. Foster, A. Lamas-Linares, J. C. Howell, Phys. Rev. B **62**, (2000)
16. J. M. Kitzman, J. R. Lane, C. Undershute, P. M. Harrington, N. R. Beysengulov, C. A. Mikolas, J. Pollanen, Nat. Commun. **14**, (2023)
17. M. Mirhosseini, A. Sipahigil, M. Kalaee, O. Painter, Nature **588**, (2020)
18. M. Wu, A. Ozcelik, J. Rufo, Z. Wang, R. Fang, T. Jun Huang, Microsyst. Nanoeng. **5**, (2019)
19. A. Bienfait, Y. P. Zhong, H. S. Chang, M. H. Chou, C. R. Conner, É. Dumur, J. Grebel, G. A. Peairs, R. G. Povey, A. N. Cleland, Phys. Rev. Lett. **130**, (2023)
20. T. Neuman, M. Eichenfield, M. E. Trusheim, L. Hackett, P. Narang, D. Englund, Npj Quant. Inf. **7**, (2021)
21. M. Aspelmeyer, T. J. Kippenberg, F. Marquardt, Rev. Mod. Phys. **86**, (2014)
22. V. Laude, APL Mater. **9**, (2021)
23. L. V. Wang, S. Hu, Science **335**, (2012)

TTMP vol 2 (2), 2025
doi: 10.30511/TTMP.2025.2057316.1051

Transactions in Theoretical and Mathematical Physics

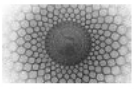

Adaptive numerical optimization for high-fidelity quantum gate control in atom interferometers

Javad Sharifi[1] [a]

[1]Electrical and Computer Engineering Department, Qom University of Technology, Qom, Iran

Received: 07 April 2025 / Accepted: 29 May 2025 / Published: 29 May 2025

Abstract The atomic interferometer has two quantum unitary gates that must be realized for quantum sensing purposes: the atomic gravimeter and the atomic interferometer gyroscope. An optimal cost function that defines the distance between two unitary operators is defined. Based on it, general adaptive (GADA) algorithms for optimization-based quantum control are innovated to realize the atomic mirror and beam-splitter gates. We used optimal quantum control to realize those atom interferometer gates. We obtained gate fidelities of 0.99980 and 0.99998 for the mirror and the beam-splitter gates, respectively. In this research, a two-level atom system with clock transitions $^1S_0 \leftrightarrow {}^3P_0$ of strontium(^{87}Sr) atom was employed.

1 Introduction

Atoms are surprisingly accurate measurement devices. They can detect external signals with high sensitivity; furthermore, they are employed for very accurate time measurement in atomic clocks. An important class of atom sensors are atom interferometers that in a controlled manner have been versatilized for investigation fundamental physics such as particle physics, general relativity [1], gravity [2, 3], gravitational wave detection [4, 5], dark matter [6] and cosmology. Atom interferometers also have several applications in quantum sensing and quantum metrology, navigation, and geophysics. Zhaoshan long-baseline atom interferometer gravitation antenna (ZAIGA) in China [7] and MAGIS-100 atom interferometer in Fermilab in USA [5] are among the most famous. For the detailed formulation of atom interferometry, see the lecture [8]. Atomic interferometer gyroscopes are more accurate than optical gyroscopes, and shortly, they are hoped to become more accurate than mechanical gyroscopes. Atom interferometers are more angle-sensitive than light interferometers because the de Broglie wavelength is much smaller than optical wavelengths. Hence, when covering the same area, the two types of interferometers display differences in phase shifts. Atom interferometers cause much longer phase shifts based on the Sagnac phase shift formula [9, 10].

Moreover, the precise working of any technology depends on its embedded control system, and especially, quantum technology requires the implementation of arbitrary control operations on the quantum system [11]. Among different technologies, quantum technology will become a dominant future technology that will change the whole lives of human beings. For quantum technology, it is essential to develop quantum materials, devices, and circuits; then, we must precisely engineer and control quantum states or unitary gates of such devices based on appropriate high-fidelity circuit readout. For example, for quantum computing applications, the exact unitary matrix of quantum gates must be implemented despite decoherence, relaxation, and, in some quantum materials, leakage errors, which lead to quantum computational subspace exit from qubit computational subspace. All of these issues, in addition to the development and engineering of the quantum devices, need precise and high-fidelity quantum control protocols [12–16] to be implemented on appropriate classical hardware such as SOC-FPGA and the quantum hardware. Quantum control as an essential part of the development of quantum science and technology dates back to 1980-2000 by pioneering research works in [17–20]. Optimized control, especially numerical pulse-based optimal control, performs better than the other quantum control methods since it guarantees optimal realization and increased convergence speed to achieve the desired quantum gates or states. Numerical optimizations were at the centre of researchers' attention. They included stochastic gradient descent [21], adaptive gradient [22, 23], momentum method [24], adaptive momentum [25],

[a]jv.sharifi@gmail.com

Levenberg-Marquardt [26], adaptive delta [27], etc. These methods have been successful in different scientific and engineering applications.

In this research, we initially innovated a numerical optimal control method. Then, we introduced the quantum dynamics of a two-level atomic transition clock and the atom interferometer. We introduced the cost function for gate realization, which was adopted from the related quantum information literature and derived the numerical pulse optimal control for this atomic system. Finally, we numerically simulated the optimal control for implementing two unitary gates of the atom interferometer, i.e., the atomic reflection or mirror and the atomic beam-splitter gate.

2 Optimal Control Methodology

Lets start with a cost function $J\big(\underline{u}(t)\big)$ of the control vector $\underline{u}_{p\times 1}(t)$. We denote the gradient vector of this cost as $\underline{g}(t) = \frac{\partial J}{\partial \underline{u}(t)}$ and the Hessian matrix as $S_{p\times p}(t) = \frac{\partial \underline{g}(t)}{\partial \underline{u}(t)}$. Now, let us expand the Taylor series of this cost function around the control vector as:

$$J\big(\underline{u}(t)+\Delta\underline{u}(t)\big) = J\big(\underline{u}(t)\big) + \Delta\underline{u}(t)^T\underline{g}(t) + \frac{1}{2}\Delta\underline{u}(t)^T S(t)\Delta\underline{u}(t) + \text{h.o.t.} \quad (1)$$

We consider the first three terms of this optimization. To minimize the cost function, the future values of the cost must be less than those of its previous ones; hence, $J\big(\underline{u}(t)+\Delta\underline{u}(t)\big) < J\big(\underline{u}(t)\big)$ leads to:

$$\Delta\underline{u}(t)^T.\Big(\underline{g}(t)+\frac{1}{2}S(t)\Delta\underline{u}(t)\Big) < 0. \quad (2)$$

Employing the above inner product, a solution of this inequality is $\underline{g}(t)+\frac{1}{2}S(t)\Delta\underline{u}(t) = -\lambda\Delta\underline{u}(t)$ in which $\lambda > 0$ is a free positive parameter. Then by simplifying this relation, we will obtain $\Delta\underline{u} = -\big(\lambda I+\frac{1}{2}S\big)^{-1}\underline{g}$ and then, we would have the following numerical control vector at iteration $k \equiv k\delta t$:

$$\underline{u}_{k+1} = \underline{u}_k - \big(\lambda I+\frac{1}{2}S_k\big)^{-1}\underline{g}_k. \quad (3)$$

Let us convert the control vector in Eq. 3 to adaptive. Then the following general adaptive (GADA) optimization would be obtained:

$$\begin{aligned}
&\underline{\xi}_k = \beta_1\underline{\xi}_{k-1} + \gamma_1\underline{g}_k \quad , \quad \underline{\xi}_0 = \underline{0}_{p\times 1},\\
&M_k = \beta_2 M_{k-1} + \gamma_2 S_k \quad , \quad M_0 = [0]_{p\times p},\\
&\underline{u}_{k+1} = \underline{u}_k - \eta\big(M_k+\lambda I\big)^{-1}\underline{\xi}_k.
\end{aligned} \quad (4)$$

In the above equation, $\underline{g}_k \to \underline{\xi}_k$ and $S_k \to M_k$ are one-order discrete-time dynamic systems without any transfer function zero; however, they have transfer function poles at β_1, β_2, Note that the pole of $S_k \to M_k$ is the zero of $\underline{\xi}_k \to \underline{u}_k$ and then it can be outside of unit-circle and the pole of $\underline{g}_k \to \underline{\xi}_k$ is the pole of $\underline{\xi}_k \to \underline{u}_k$. Then to stabilize the control signal iteration $\beta_1 \in [0,1)$ and $\beta_2 \in R$ and the parameters γ_1, γ_2 must be real numbers. Actually, with this adaptation, we include a forgetting factor coefficient of gradient vectors and Hessian matrices in optimization-based control, i.e. $M_k = \gamma_2\sum_{i=1}^{k}(\beta_2^{k-i}H_i), \underline{\xi}_k = \gamma_1\sum_{i=1}^{k}(\beta_1^{k-i}\underline{g}_i)$, then by adding the momentum terms and the Hessian matrix and gradient vector became dynamic which causes the optimal control system to converge faster compared to the conventional gradient optimization methods. We mention that this adaptive optimization for $\beta_1 = \beta_2 = \gamma_2 = 0, \gamma_1 = 1, \lambda = 1$ diminishes to the stochastic gradient descent (SGD). For parameters $\beta_1 = \beta_2 = 0, \gamma_1 = 1$ and a quadratic cost function, GADA diminishes to the Levenberg–Marquardt (LM) optimization, and for $\beta_2 = \gamma_2 = 0$ it diminishes to adaptive gradient method (AdaGrad). Note that SGD and LM are not adaptive optimization methods. If the inversion of matrix in equation4 for the large Hessian matrix is problematic, heuristically we can consider only the diagonal elements of the Hessian matrix S_k and the off-diagonal elements equal to zero,i.e. $S_k = \text{diag}\big(\frac{\partial^2 J}{\partial u_{1,k}^2},..,\frac{\partial^2 J}{\partial u_{p,k}^2}\big)$. In this condition, the M_k matrix and also the $M_k+\lambda I$ are always diagonal and the inverse $(M_k+\lambda I)^{-1}$ is trivial, let us call this simplified adaptive optimization, the diagonal adaptive (DADA) algorithm in the subsequent sections.

3 Atom Interferometer Application

3.1 Two-Level Atom Rabi Oscillation as Rotation over Bloch Sphere

These quantum mechanical matter waves can be manipulated with the atomic equivalents of lenses, beam-splitters, and mirrors. Atom interferometry is analogous to optical interferometry. In both interferometers, a beam-splitter splits an incident wave into two paths. The two paths are later redirected back toward each other with mirrors and overlapped on a final beam-splitter to produce an interference pattern (see figure 1). Making beam-splitters and mirrors in

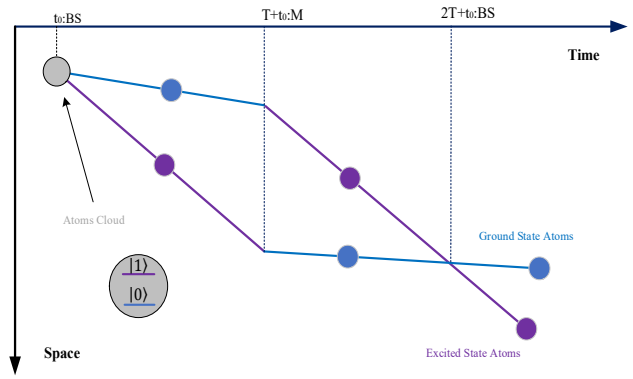

Fig. 1 Mach-Zehnder based Atom Interferometer in space-time coordinate: At times t_0 and $2T+t_0$, the atomic beam splitter (BS) and also at time $T+t_0$, the atomic mirror (M) must be implemented.

optical beams is known. To implement similar interferometer devices, such as those in atomic experiments, an ensemble of cold two-level atoms such as Strontium atom (^{87}Sr) in clock transition states ($|0\rangle = {}^1S_0 \leftrightarrow |1\rangle = {}^3P_0$) with a $\lambda_{|0\rangle\leftrightarrow|1\rangle} = 698$nm wavelength transition and a very long coherence time is considered. Freely falling atoms have enabled the development of atomic gravimeters and atomic gyrometers. In these devices, an atom cloud measures acceleration by sensing the spatial phase shift of a laser beam along its freely falling trajectory.

The quantum system described by Schrödinger equation as ($\hbar \equiv 1$): $i\frac{d}{dt}|\psi_t\rangle = H(t)|\psi_t\rangle$. The Hamiltonian of two-level atom in Rabi modeling is:

$$H(t) = \frac{1}{2}\begin{pmatrix} \Delta(t) & \Omega(t)e^{-i\phi} \\ \Omega(t)e^{i\phi} & -\Delta(t) \end{pmatrix}, \tag{5}$$

in which Ω, Δ are Rabi frequency and detuning respectively and ϕ is the initial phase of laser electric field. Sometimes, scientists employ the three-level Raman transition atoms for atom interferometer [8]; in this case, there are two stable atomic levels $|0\rangle, |1\rangle$ and an unstable excited state $|e\rangle$. For Raman's levels atoms, there are two laser beams; one is the upward beam with Rabi frequency Ω_1 and phase ϕ_1, which transfers the atomic state transition $|0\rangle \to |e\rangle$ and the other is a downward beam with Rabi frequency Ω_2 and phase ϕ_2 which lead to transition $|e\rangle \to |1\rangle$, the detuning in both transitions assumes to be approximately equal to Δ. In [28] it is shown that with two Rabi-frequencies Ω_1, Ω_2, the three-level Raman transition atom can be approximated with two-level atom with $\Omega = \frac{\Omega_1\Omega_2}{2\Delta}, \phi = \phi_2 - \phi_1$, then for every interferometer, we can use two-level Hamiltonian model of equation5. We can write this Hamiltonian based on Pauli matrices $\sigma_x, \sigma_y, \sigma_z$ as follows:

$$H(t) = \frac{1}{2}\Big(\Omega(t)\cos(\phi)\sigma_x + \Omega(t)\sin(\phi)\sigma_y + \Delta(t)\sigma_z\Big). \tag{6}$$

Let us define the infinitesimal evolution as $\mathscr{M}_n = e^{-iH_n\delta t}$, then the unitary propagator at time step $k\delta t$ is:

$$U_k = \mathscr{M}_k\mathscr{M}_{k-1}....\mathscr{M}_1 \quad , \quad |\psi_k\rangle = U_k|\psi_0\rangle. \tag{7}$$

The evolution of the two-level atom at time sample $t = k\delta t$ is:

$$\mathscr{M}(n\delta t) = \exp\Big(-\tfrac{i}{2}\delta t\big(\cos(\phi)\sigma_x + \sin(\phi)\sigma_y\big)\Omega(n\delta t) - \tfrac{i}{2}\delta t\,\sigma_z\Delta(n\delta t)\Big). \tag{8}$$

We know that, the rotation operator is [29]:

$$\begin{aligned}\mathscr{R}_{\vec{r}(t),\alpha(t)} &= e^{-i\frac{\alpha(t)}{2}\hat{r}(t)\cdot\vec{\sigma}} \\ &= \sin\big(\tfrac{1}{2}\alpha(t)\big)I - i\cos\big(\tfrac{1}{2}\alpha(t)\big)\,\hat{r}(t)\cdot\vec{\sigma},\end{aligned} \tag{9}$$

where $\vec{\sigma} = \sigma_x\hat{x} + \sigma_y\hat{y} + \sigma_z\hat{z}$, and $\hat{r} = r_x\hat{x} + r_y\hat{y} + r_z\hat{z}$ is the rotation axis and $\alpha = \omega_q t$ is the rotation angle, ω_q is the angular speed of quantum state vector on Bloch sphere. By comparing Eq. (8) and Eq.(9), we will obtain:

$$\alpha\hat{r} = \delta t\Big(\cos(\phi)\,\Omega(n\delta t)\,\hat{x} + \sin(\phi)\,\Omega(n\delta t)\,\hat{y} + \Delta(n\delta t)\,\hat{z}\Big). \tag{10}$$

Then since $|\alpha\hat{r}| = \alpha$ we obtain:

$$\alpha(n\delta t) = \delta t\sqrt{\Omega_n^2 + \Delta_n^2}, \tag{11}$$

$$\hat{r}(n\delta t) = \cos(\phi)\frac{\Omega_n}{\sqrt{\Omega_n^2+\Delta_n^2}}\hat{x} + \sin(\phi)\frac{\Omega_n}{\sqrt{\Omega_n^2+\Delta_n^2}}\hat{y} + \frac{\Delta_n}{\sqrt{\Omega_n^2+\Delta_n^2}}\hat{z}. \tag{12}$$

In these relations, we use these abbreviations $\Omega_n = \Omega(n\delta t)$, $\Delta_n = \Delta(n\delta t)$.

3.2 Atom Interferometer Gates Realization

The unitary operator of a mirror (M) and beam-splitter (BS) is:

$$U_M = \begin{pmatrix} 0 & 1 \\ 1 & 0 \end{pmatrix} = \sigma_x, U_{BS} = \frac{1}{\sqrt{2}} \begin{pmatrix} 1 & i \\ i & 1 \end{pmatrix}. \tag{13}$$

The aim of gate optimization is the implementation of atomic unitary operator of Eq. (7) to move to the desired gate of Eq. (13). For this aim, we can select an objective function as:

$$\begin{aligned} J_{\text{gate}}(T) &:= 1 - \frac{1}{d^2} \left| \langle U_{\text{gate}}, U_{\text{atom}}(T) \rangle \right|^2 \\ &= 1 - \frac{1}{d^2} \left| \text{Tr}\left(U_{\text{gate}}^{\dagger} U_{\text{atom}}(T) \right) \right|^2, \end{aligned} \tag{14}$$

in which $U_{atom} = U(k\delta t), gate = M, BS, d = \dim(U_{gate}) = 2$ and † is transpose complex conjugate. For this cost function as $U_{atom} \to U_{gate}$ then $J_{gate} \to 0$. The control vector includes Rabi-frequency and detuning, then the gradient vector and the Hessian matrix are:

$$\underline{u}_k = \begin{bmatrix} \Omega_k \\ \Delta_k \end{bmatrix}, \ \underline{g}_k = \begin{bmatrix} \frac{\partial J_{gate}}{\partial \Omega_k} \\ \frac{\partial J_{gate}}{\partial \Delta_k} \end{bmatrix}, \ S_k = \begin{pmatrix} \frac{\partial^2 J_{gate}}{\partial \Omega_k^2} & \frac{\partial^2 J_{gate}}{\partial \Omega_k \partial \Delta_k} \\ \frac{\partial^2 J_{gate}}{\partial \Delta_k \partial \Omega_k} & \frac{\partial^2 J_{gate}}{\partial \Delta_k^2} \end{pmatrix}. \tag{15}$$

3.3 Code Structure and Parameter Selection

For simulation, we develop the codes in Python 3 by using Numpy, QuTip, and Matplotlib packages. The general learning parameter η is set to 10^8, and the other parameters for each gate realization are explained in subsequent subsections. After setting the parameters, we optimize them in each iteration in a for loop based on the above adaptive optimization. In the for loop, we save each quantum state and fidelity value, which allows us to plot the quantum state transition on the Bloch sphere and also the fidelity curve.

3.4 Mirror Gate

At first we choose to implement the mirror gates, then we will obtain the following cost function:

$$\begin{aligned} J_M &= 1 - \cos^2\left(\tfrac{1}{2}\alpha\right) r_x^2 \\ &= 1 - \cos^2(\phi)\cos^2\left(\tfrac{1}{2}\delta t \sqrt{\Omega_n^2 + \Delta_n^2}\right) \frac{\Omega_n^2}{\Omega_n^2 + \Delta_n^2}. \end{aligned} \tag{16}$$

Then, the following updates for the gradient vector will be obtained:

$$\begin{aligned} \frac{\partial J_M}{\partial \Omega_k} &= \tfrac{1}{2}\delta t \cos^2(\phi)\sin(\alpha) \frac{\Omega_k^3}{\left(\Omega_k^2 + \Delta_k^2\right)^{3/2}} \\ &\quad - 2\cos^2(\phi)\cos^2\left(\tfrac{1}{2}\alpha\right) \frac{\Omega_k \Delta_k^2}{\left(\Omega_k^2 + \Delta_k^2\right)^2}, \end{aligned} \tag{17}$$

$$\begin{aligned} \frac{\partial J_M}{\partial \Delta_k} &= \tfrac{1}{2}\delta t \cos^2(\phi)\sin(\alpha) \frac{\Delta_k \Omega_k^2}{\left(\Omega_k^2 + \Delta_k^2\right)^{3/2}} \\ &\quad + 2\cos^2(\phi)\cos^2\left(\tfrac{1}{2}\alpha\right) \frac{\Delta_k \Omega_k^2}{\left(\Omega_k^2 + \Delta_k^2\right)^2}. \end{aligned} \tag{18}$$

The elements of Hessian matrix by neglecting $(\delta t)^2$ term is:

$$\begin{aligned} \frac{\partial^2 J_M}{\partial \Omega_k^2} &= \tfrac{5}{2}\delta t \cos^2(\phi)\sin(\alpha) \frac{\Omega_k^2 \Delta_k^2}{(\Omega_k^2 + \Delta_k^2)^{5/2}} \\ &\quad - 2\cos^2(\phi)\cos^2\left(\tfrac{1}{2}\alpha\right) \Delta_k^2 \frac{\Delta_k^2 - 3\Omega_k^2}{(\Omega_k^2 + \Delta_k^2)^3}, \end{aligned} \tag{19}$$

$$\begin{aligned} \frac{\partial^2 J_M}{\partial \Delta_k^2} &= \tfrac{1}{2}\delta t \cos^2(\phi)\sin(\alpha)\, \Omega_k^2 \frac{\Omega_k^2 - 4\Delta_k^2}{(\Omega_k^2 + \Delta_k^2)^{5/2}} \\ &\quad + 2\cos^2(\phi)\cos^2\left(\tfrac{1}{2}\alpha\right) \Omega_k^2 \frac{\Omega_k^2 - 3\Delta_k^2}{(\Omega_k^2 + \Delta_k^2)^3}, \end{aligned} \tag{20}$$

$$\begin{aligned} \frac{\partial^2 J_M}{\partial \Omega_k \partial \Delta_k} &= \frac{\partial^2 J_M}{\partial \Delta_k \partial \Omega_k} \\ &= \tfrac{1}{2}\delta t \cos^2(\phi)\sin(\alpha) \frac{2\Omega_k \Delta_k^3 - 3\Delta_k \Omega_k^3}{(\Omega_k^2 + \Delta_k^2)^{5/2}} \\ &\quad - 4\cos^2(\phi)\cos^2\left(\tfrac{1}{2}\alpha\right) \frac{\Omega_k^3 \Delta_k - \Omega_k \Delta_k^3}{(\Omega_k^2 + \Delta_k^2)^3}. \end{aligned} \tag{21}$$

To make Optimization possible, we must have the initial phase of the Rabi signal as $\phi \neq \frac{(2n+1)\pi}{2}$. Based on SGD with parameter setting of $(\beta_1 = \beta_2 = \gamma_2 = 0, \gamma_1 = 0.85, \lambda = 1)$ in GADA method, the optimal control signals are depicted in figure (2 a_1, b_1) and the fidelity of gate optimization is depicted in figure (2 c_1). Also, with the GADA method, the optimal control signals are depicted in figure (2 a_2, b_2) and the fidelity of gate optimization is depicted in figure (2 c_2). By using the GADA optimal control, after 44 samples of 1-microsecond control pulses (see table 1), we obtain gate

fidelity of 0.999 for the atomic mirror realization, which has a unitary of atomic gate approximately up to a phase factor $e^{i\frac{\pi}{2}}$ which is different from the actual mirror gate of Eq. 13:

$$U_{\text{atomM}}(N\delta t) = \begin{pmatrix} 0.02-0.06i & 0.999i \\ 0.999i & 0.02+0.06i \end{pmatrix}, \quad N = 44, \quad \delta t = 1\,\mu\text{s}. \tag{22}$$

By gate optimization, simultaneously we can control two populations of atoms, one population from state $|0\rangle$ to $|1\rangle$ and the other population from $|1\rangle$ to $|0\rangle$ as we can see in figure (2 d_1) for SGD and figure (2 d_2) for GADA method. Since the result of SGD,LM and AdaGrad are similar to each other and also GADA is similar to DADA, then one method from each set is depicted in figure 2.

Table 1 Number of control pulses ($\delta t = 1\,\mu$s each pulse width) and fidelity based on optimization method to realize NOT gate

Optimization Method	Control Pulse Number	NOT Gate Fidelity
SGD	42	0.99850
AdaGrad	45	0.99846
LM	43	0.99936
GADA	44	0.99980
DADA	44	0.99990

3.5 Beam-Splitter Gate

Now, to optimally implement the atomic beam-splitter on atomic clouds, we will optimize the following cost function:

$$J_{BS} = 1 - \frac{1}{2}\left(\sin(\tfrac{1}{2}\alpha) - \cos(\tfrac{1}{2}\alpha) r_x\right)^2, \tag{23}$$

and after simple calculations, we will have the following update rules for Rabi frequency and detunings:

$$\frac{\partial J_{BS}}{\partial \Omega_k} = -\left(\sin\left(\tfrac{1}{2}\alpha\right) - \cos\left(\tfrac{1}{2}\alpha\right) r_x\right) \times \left(\tfrac{1}{2}\delta t \left(\cos\left(\tfrac{1}{2}\alpha\right) + \sin\left(\tfrac{1}{2}\alpha\right) r_x\right) \frac{\Omega_k}{\sqrt{\Omega_k^2+\Delta_k^2}} - \cos\left(\tfrac{1}{2}\alpha\right)\cos(\phi)\frac{\Delta_k^2}{\left(\Omega_k^2+\Delta_k^2\right)^{3/2}}\right), \tag{24}$$

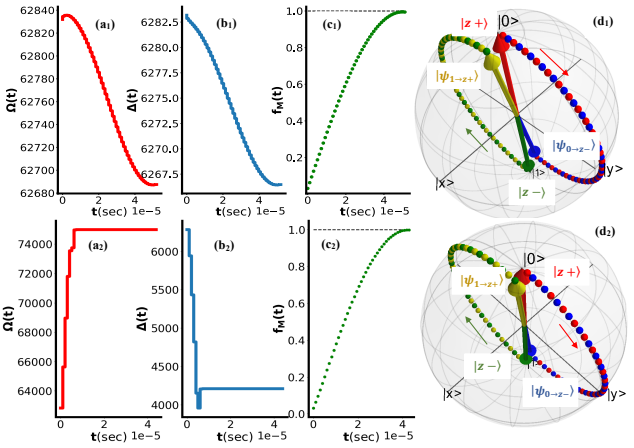

Fig. 2 Atom interferometer mirror gate realization: Top is for SGD and Bottom is for GADA based on optimal quantum control methods. SGD parameters: ($\beta_1 = \beta_2 = \gamma_2 = 0, \gamma_1 = 1, \lambda = 1$) and GADA parameters ($\beta_1 = 0.85, \beta_2 = 85, \gamma_1 = \gamma_2 = 1, \lambda = 10^{-2}$). ($a_1, b_1$) are the control pulses and (c_1) fidelity function for implementation of the atomic mirror gate realization and (d_1) shows the simultaneous quantum state transfer ($|0\rangle = |z+\rangle \to |1\rangle = |\psi_{0\to z-}\rangle$ and $|1\rangle = |z+\rangle \to |0\rangle = |\psi_{1\to z+}\rangle$) on Bloch-sphere using optimal mirror gate realization with SGD. Figures (a_2, b_2, c_2) are the control pulses and the fidelity over time for mirror implementation with GADA. (d_2) displays simultaneous quantum state transfer using optimal mirror gate realization on Bloch-sphere via GADA.

$$\frac{\partial J_{BS}}{\partial \Delta_k} = -\left(\sin\left(\tfrac{1}{2}\alpha\right) - \cos\left(\tfrac{1}{2}\alpha\right) r_x\right) \times \left(\tfrac{1}{2}\delta t \left(\cos\left(\tfrac{1}{2}\alpha\right) + \sin\left(\tfrac{1}{2}\alpha\right) r_x\right) \frac{\Delta_k}{\sqrt{\Omega_k^2+\Delta_k^2}} + \cos\left(\tfrac{1}{2}\alpha\right)\cos(\phi)\frac{\Delta_k\Omega_k}{\left(\Omega_k^2+\Delta_k^2\right)^{3/2}}\right), \tag{25}$$

and the Hessian matrix elements are:

$$\begin{aligned}\frac{\partial^2 J_{BS}}{\partial \Omega_k^2} = &-\left(\tfrac{1}{2}\delta t \left(\cos\left(\tfrac{1}{2}\alpha\right) + \sin\left(\tfrac{1}{2}\alpha\right) r_x\right) \frac{\Omega_k}{\sqrt{\Omega_k^2+\Delta_k^2}} - \cos\left(\tfrac{1}{2}\alpha\right)\cos(\phi)\frac{\Delta_k^2}{\left(\Omega_k^2+s_\Delta^2\right)^{3/2}}\right)^2 \\ &- \left(\sin\left(\tfrac{1}{2}\alpha\right) - \cos\left(\tfrac{1}{2}\alpha\right) r_x\right) \times \left[\tfrac{1}{2}\delta t \sin\left(\tfrac{1}{2}\alpha\right) \frac{\Omega_k\Delta_k^2}{\Omega_k^2+\Delta_k^2} + \tfrac{1}{2}\delta t \left(\cos\left(\tfrac{1}{2}\alpha\right) + \sin\left(\tfrac{1}{2}\alpha\right) r_x\right) \frac{\Delta_k^2}{\left(\Omega_k^2+\Delta_k^2\right)^{3/2}} \right. \\ &\left. + \tfrac{1}{2}\delta t \sin\left(\tfrac{1}{2}\alpha\right)\cos(\phi)\frac{\Delta_k^2\Omega_k}{\left(\Omega_k^2+\Delta_k^2\right)^2} + 3\cos\left(\tfrac{1}{2}\alpha\right)\cos(\phi)\frac{\Delta_k^2\Omega_k}{\left(\Omega_k^2+\Delta_k^2\right)^3}\right],\end{aligned} \tag{26}$$

$$\frac{\partial^2 J_{BS}}{\partial \Delta_k^2} = -\Bigg(\tfrac{1}{2}\delta t \left(\cos\left(\tfrac{1}{2}\alpha\right) + \sin\left(\tfrac{1}{2}\alpha\right) r_x\right) \frac{\Delta_k}{\sqrt{\Omega_k^2+\Delta_k^2}} + \cos\left(\tfrac{1}{2}\alpha\right)\cos(\phi)\frac{\Delta_k\Omega_k}{\left(\Omega_k^2+\Delta_k^2\right)^{3/2}}\Bigg)^2 - \left(\sin\left(\tfrac{1}{2}\alpha\right) - \cos\left(\tfrac{1}{2}\alpha\right) r_x\right) \times \Bigg[- \tfrac{1}{2}\delta t \sin\left(\tfrac{1}{2}\alpha\right)\frac{\Omega_k^2\Delta_k}{\Omega_k^2+\Delta_k^2} + \tfrac{1}{2}\delta t \left(\cos\left(\tfrac{1}{2}\alpha\right) + \sin\left(\tfrac{1}{2}\alpha\right) r_x\right)\frac{\Omega_k^2}{\left(\Omega_k^2+\Delta_k^2\right)^{3/2}} - \tfrac{1}{2}\delta t \sin\left(\tfrac{1}{2}\alpha\right)\cos(\phi)\frac{\Delta_k^2\Omega_k}{\left(\Omega_k^2+\Delta_k^2\right)^2} + \cos\left(\tfrac{1}{2}\alpha\right)\cos(\phi)\frac{\Omega_k^3-2\Delta_k^2\Omega_k}{\left(\Omega_k^2+\Delta_k^2\right)^{5/2}}\Bigg], \tag{27}$$

$$\begin{aligned}\frac{\partial^2 J_{BS}}{\partial \Delta_k \partial \Omega_k} &= \frac{\partial^2 J_{BS}}{\partial \Omega_k \partial \Delta_k} \\ &= -\Bigg(\tfrac{1}{2}\delta t \left(\cos\left(\tfrac{1}{2}\alpha\right) + \sin\left(\tfrac{1}{2}\alpha\right) r_x\right) \frac{\Delta_k}{\sqrt{\Omega_k^2+\Delta_k^2}} + \cos\left(\tfrac{1}{2}\alpha\right)\cos(\phi)\frac{\Delta_k\Omega_k}{\left(\Omega_k^2+\Delta_k^2\right)^{3/2}}\Bigg) \\ &\quad \times \Bigg(\tfrac{1}{2}\delta t \left(\cos\left(\tfrac{1}{2}\alpha\right) + \sin\left(\tfrac{1}{2}\alpha\right) r_x\right) \frac{\Omega_k}{\sqrt{\Omega_k^2+\Delta_k^2}} - \cos\left(\tfrac{1}{2}\alpha\right)\cos(\phi)\frac{\Delta_k^2}{\left(\Omega_k^2+\Delta_k^2\right)^{3/2}}\Bigg) \\ &\quad - \left(\sin\left(\tfrac{1}{2}\alpha\right) - \cos\left(\tfrac{1}{2}\alpha\right) r_x\right) \times \Bigg[- \tfrac{1}{2}\delta t \sin\left(\tfrac{1}{2}\alpha\right)\cos(\phi)\frac{\Omega_k^2\Delta_k}{\left(\Omega_k^2+\Delta_k^2\right)^2} \\ &\quad - \tfrac{1}{2}\delta t \left(\cos\left(\tfrac{1}{2}\alpha\right) + \sin\left(\tfrac{1}{2}\alpha\right) r_x\right)\frac{\Omega_k\Delta_k}{\left(\Omega_k^2+\Delta_k^2\right)^{3/2}} \\ &\quad + \tfrac{1}{2}\delta t \sin\left(\tfrac{1}{2}\alpha\right)\cos(\phi)\frac{\Delta_k^3}{\left(\Omega_k^2+\Delta_k^2\right)^2} \\ &\quad + \cos\left(\tfrac{1}{2}\alpha\right)\cos(\phi)\frac{\Delta_k^3-2\Delta_k\Omega_k^2}{\left(\Omega_k^2+\Delta_k^2\right)^{5/2}}\Bigg]. \end{aligned} \tag{28}$$

Based on SGD with parameter setting of ($\beta_1=\beta_2=\gamma_2=0, \gamma_1=1, \lambda=1$) in GADA method, the optimal control signals are depicted in figure (3 a_1, b_1) and the fidelity of gate optimization is depicted in figure (3 c_1). Also, with the GADA method, the optimal control signals are depicted in figure (3 a_2, b_2) and the fidelity of gate optimization is depicted in figure (3 c_2). The control signals are depicted in figure (3 a_2, b_2) and the fidelity of gate optimization is depicted in figure (3 c_2). After 23 samples of 1-microsecond control pulse we reach the fidelity of 0.9998 for beam-splitter gate optimization (see table 2) and the atomic beam-splitter gate at this optimal control reach:

$$U_{\text{atomBS}}(N\delta t) = \begin{pmatrix} 0.703-0.025i & 0.710i \\ 0.710i & 0.703+0.025i \end{pmatrix}, \quad N=23, \quad \delta t = 1\,\mu\text{s}. \tag{29}$$

By gate optimization, simultaneously we can control two populations of atoms, one population from state $|0\rangle$ to $|y+\rangle$ and other population from $|1\rangle$ to $|y-\rangle$ as we can see in figure (3 d_1) for SGD method and in figure (3 d_2) for GADA method.

Optimization Method	Control Pulse Number	Beam-Splitter Gate Fidelity
SGD	26	0.99985
AdaGrad	26	0.99991
LM	26	0.9999
GADA	23	0.99998
DADA	24	0.99996

Table 2 Fidelities and control parameters for different optimization methods.

4 Conclusion

Several researchers have developed and employed numerical optimal controls, such as SGD and AdaGrad, for quantum state preparation and some for gate synthesis. Here, we derived a general adaptive optimal methodology to speed up quantum gate realization and to increase the quantum gate fidelity. Several numerical optimizations can be deduced as a special case of our method; hence, we have more degrees of freedom to optimize the cost function of physical systems by this adaptive method. However, our optimal quantum control methodology was employed to realize atom interferometers; it will open up a new window for high-fidelity quantum gates realization for quantum computing purposes. For instance, we can realize the most important fundamental one-qubit gates such as NOT(σ_x), Hadamard ($\frac{1}{\sqrt{2}}(\sigma_x+\sigma_z)$), phase shift gate, etc. and also fundamental two-qubit gates such as CNOT ($|0\rangle\langle 0|\otimes \mathrm{I} + |1\rangle\langle 1|\otimes\sigma_x$), CPHASE ($|0\rangle\langle 0|\otimes \mathrm{I} + |1\rangle\langle 1|\otimes\sigma_z$), etc which are essential for quantum algorithms. In this research, we achieved

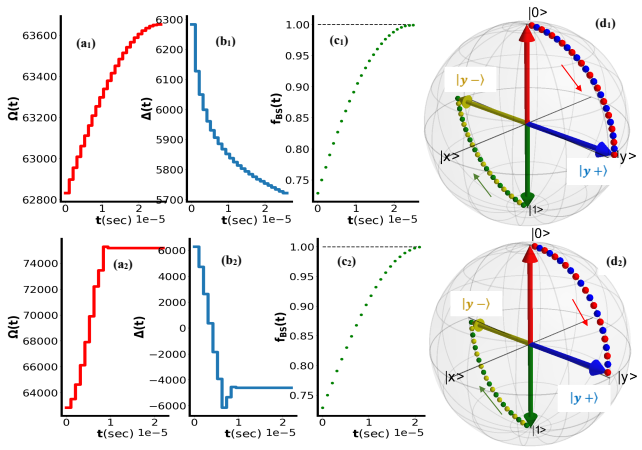

Fig. 3 Atom interferometer beam-splitter gate realization: Top is for SGD and Bottom is for GADA based on optimal quantum control methods. SGD parameters: $(\beta_1 = \beta_2 = \gamma_2 = 0, \gamma_1 = 1, \lambda = 1)$ and GADA parameters $(\beta_1 = 0.85, \beta_2 = 85, \gamma_1 = \gamma_2 = 1, \lambda = 10^{-1})$. (a_1, b_1) are the control pulses and (c_1) fidelity function for implementation of the atomic beam-splitter gate realization and (d_1) shows the simultaneous quantum state transfer $(|0\rangle \rightarrow \frac{1}{\sqrt{2}}(|0\rangle + i|1\rangle)$ and $\frac{1}{\sqrt{2}}(i|0\rangle + |1\rangle) \rightarrow |1\rangle$ on Bloch-sphere using optimal mirror gate realization with SGD. Figures (a_2, b_2, c_2) are the control pulses and the fidelity over time for mirror implementation with GADA. (d_2) displays simultaneous quantum state transfer using optimal beam-splitter gate realization on Bloch-sphere.

high fidelity of gate realization and faster convergence compared to conventional optimization methods. The method employed in this research is a promising methodology for quantum control applications from quantum sensing, quantum computing, and quantum simulations for different quantum system platforms such as superconductor circuits, atom spin systems and the spin quantum dot.

References

1. C.-W. Chou, D. B. Hume, T. Rosenband, D. J. Wineland, Science **329**, (2010)
2. X. Wu et al., Sci. Adv. **5**, (2019)
3. T. Kovachy et al., Nature **528**, (2015)
4. A. Loeb, D. Maoz, arXiv:1501.00996, (2015)
5. M. Abe et al., *Matter-wave Atomic Gradiometer Interferometric Sensor*, IOP Publishing (2021)
6. A. Arvanitaki, J. Huang, K. Van Tilburg, Phys. Rev. D, **91** (2015)
7. M.-S. Zhan et al., Int. J. Mod. Phys. D, **29,** (2020)
8. T. Kovachy et al., *Macroscopic scale atom interferometers: introduction, techniques, and applications*, Oxford University Press (2019)
9. J. Fang, J. Qin, Sensors, **12**, (2012)
10. T. L. Gustavson, Ph.D. thesis, Stanford University (2000)
11. J. Zhang, D. Burgarth, R. Laflamme, D. Suter, Phys. Rev. A **91**, (2015)
12. S. Kwon, A. Tomonaga, G. L. Bhai, S. J. Devitt, J.-S. Tsai, J. Appl. Phys., **129**, (2021)
13. P. Krantz et al. Appl. Phys. Rev., **6**, (2019)
14. H. Häffner, C. F. Roos, R. Blatt, Phys. Rep., **469**, (2008)
15. D. S. Weiss, M. Saffman, Phys. Today, **70**, (2017)
16. L. Henriet et al. Quantum, **4**, (2020)
17. G. M. Huang, T. J. Tarn, J. W. Clark, J. Math. Phys. **24**, (1983)
18. V. P. Belavkin, Autom. Remote Control, (1983)
19. W. S. Warren, H. Rabitz, M. Dahleh, Science, **259**, (1993)
20. S. Chu, Nature, **416**, (2002)
21. H. Robbins, S. Monro, Ann. Math. Stat., (1951)
22. H. B. McMahan, M. Streeter, Proc. 23rd Annu. Conf. Learn. Theory (COLT), (2010)
23. D. Zhou et al. Trans. Mach. Learn. Res. (2024)
24. N. Qian, Neural networks, **12**, (1999)
25. D. P. Kingma, J. Ba, Proc. 3rd Int. Conf. Learn. Represent. (ICLR) (2015)
26. Nelles, Oliver, *Nonlinear system identification*, IOP Publishing (2002)
27. M. D. Zeiler, arXiv:1212.5701, (2012)
28. Berman, Paul R, *Atom interferometry*, Academic press, (1997)
29. I. Glendinning, ResearchGate presentation, (2010)

TTMP vol 2 (2), 2025
doi: 10.30511/TTMP.2025.2061423.1054

Transactions in Theoretical and Mathematical Physics

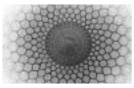

Asymptotic behaviors of solutions to a singular non-local fourth-order parabolic equation with gradient-type logarithmic nonlinearity

Tingfu Feng[a], **Ruixi Li**[b], **Mengrui Yang**[c]

[1]Department of Mathematics, Kunming University, Kunming, Yunnan, 650214, China

Received: 22 May 2025 / Accepted: 30 May 2025 / Published: 30 May 2025

Abstract In this paper, we consider the initial-boundary value problem to a singular non-local fourth-order parabolic equation with gradient-type logarithmic nonlinearity. We prove the global existence of weak solutions by utilizing the cut-off function technique and Galerkin's approximation method. We establish novel threshold criteria for the finite-time blow-up of solutions with initial value at arbitrary energy levels, and derive explicit upper bounds for the blow-up time under appropriate conditions. Furthermore, by employing energy estimates and specific ordinary differential inequalities, we characterize both non-extinction and extinction phenomena of solutions in finite time, and rigorously quantify their corresponding extinction rates.

1 Introduction

In this paper, we consider the initial-boundary value problem to a singular non-local fourth-order parabolic equation with gradient-type logarithmic nonlinearity:

$$\begin{cases} \frac{u_t}{|x|^s}+\Delta^2 u+\operatorname{div}\left(|\nabla u|^{p-2}\nabla u\log|\nabla u|\right) \\ \qquad =|u|^q-\frac{1}{|\Omega|}\int_\Omega |u|^q dx, & x\in\Omega,\quad t>0, \\ \frac{\partial u}{\partial \eta}=\frac{\partial \Delta u}{\partial \eta}=0, & x\in\partial\Omega,\ t>0, \\ u(x,0)=u_0(x), & x\in\Omega, \end{cases} \tag{1}$$

where $\Omega\subset\mathbb{R}^N (N>2)$ is a bounded domain with smooth boundary $\partial\Omega$, η denotes the outward unit normal vector on $\partial\Omega$, $x=(x_1,x_2,\cdots,x_N)$ with $|x|=\sqrt{x_1^2+x_2^2+\cdots+x_N^2}$, the initial data $u_0\in H^2(\Omega)$ satisfies $\int_\Omega u_0 dx=0$, and the parameters satisfy $0\le s\le 2$, $p>0$, $q>0$. Note that when $s=0$, Eq. (1) reduces to the following fourth-order parabolic equation:

$$u_t+\Delta^2 u-\operatorname{div}(f(\nabla u))=g(x,t). \tag{2}$$

This class of equations models epitaxial growth in nanoscale thin films [1–4], particularly focusing on surface roughening phenomena during thin film deposition. Here, u represents the height from the surface of the thin film, $\Delta^2 u$ denotes capillarity-driven surface diffusion, and $\operatorname{div}(f(\nabla u))$ describes upward atomic hopping. Recent studies on thin film equations have yielded significant advances in several key areas:

• For the case

$$\operatorname{div}(f(\nabla u))=\operatorname{div}\left(|\nabla u|^{p-2}\nabla u\right)+\Delta u,\quad p>2, \tag{3}$$

King, Stein and Winkler [5] established not only the existence, uniqueness, and regularity of solutions in an appropriate function space but also characterized the structure of the ω-limit set by employing a semi-discrete approximation technique to study the asymptotic behavior of solutions. When

$$\operatorname{div}(f(\nabla u))=-\mu\Delta u-\lambda\Delta|\nabla u|^2,\quad g(x,t)=f(x), \tag{4}$$

Winkler [6] proved the existence of global solutions in higher-dimensional settings. For the case where $g(x,t)=0$, $f(\nabla u)$ satisfies the growth condition

[a]Corresponding author: fengtingfu@kmu.edu.cn
[b]ruixili0321@163.com
[c]mengruiyang2023@163.com

$$\left|f'(\xi_1)-f'(\xi_2)\right| \le C\left(|\xi_1|^{\alpha-1}+|\xi_2|^{\alpha-1}\right)|\xi_1-\xi_2|, \quad \forall \xi_1,\xi_2 \in \mathbb{R}^N, \quad \alpha>1, \tag{5}$$

Sandjo, Moutari and Gningue [7] demonstrated the existence, uniqueness, and regularity of solutions in the function space $C^0([0,T];L^p(\Omega))$, with $p=\frac{N\alpha}{2-\alpha}$ and $1<\alpha<2$, by employing L_p-L_q estimates derived from Kato's method [8–10]. For further studies on thin film equations featuring the p-Laplacian nonlinearity $\operatorname{div}(f(\nabla u))=\operatorname{div}\left(|\nabla u|^{p-2}\nabla u\right)$, we refer to [11–24, 26–29] and references therein.

• Under the influence of molecular and ionic effects, the conventional p-Laplacian nonlinearity $\operatorname{div}\left(|\nabla u|^{p-2}\nabla u\right)$ is replaced by a gradient-type logarithmic nonlinearity of the form

$$\operatorname{div}\left(|\nabla u|^{p-2}\nabla u\log|\nabla u|\right). \tag{6}$$

In [30], Liu, Ma and Tang established rigorous lower bounds for both the blow-up time and the blow-up rate of solutions under $g(x,t)=0$. For the case $g(x,t)=u^q\log u$, Liu, Li and Li [31] established a complete characterization of solution behavior (finite-time blow-up versus global existence) through a classification scheme based on both the initial energy and the Nehari energy. Additionally, the authors derived precise asymptotic estimates for the blow-up time in finite-time blow-up cases, as well as quantitative decay rates for global solutions. For the case $g(x,t)=u^q\log u$, Liu, Li and Li [31] established conditions for blow-up or global existence by classifying the initial energy and the Nehari energy. Furthermore, they showed asymptotic estimates for blow-up time and a large-time estimate of solutions, respectively. For the case $g(x,t)=-\alpha\Delta u-u^{q-1}u$, Lv and Fang [32] studied the asymptotic behavior of global weak solutions under the conditions $0<q\le 1$ and $\alpha<\lambda_1$, where λ_1 denotes the first eigenvalue of $-\Delta u$ with null Dirichlet boundary conditions. For further studies on fourth-order pseudo-parabolic equations with gradient-dependent logarithmic nonlinearities of the form $\operatorname{div}\left(|\nabla u|^{p-2}\nabla u\log|\nabla u|\right)$, we refer to [33] and [34].

In a homogeneous, isotropic, rigid porous medium saturated with a compressible fluid, the balance of mass for the fluid phase is expressed as [35]:

$$\theta(x)u_t-\operatorname{div}(u\mathbf{V})=f(u), \tag{7}$$

where $\theta(x)$ is the volumetric moisture content, $\mathbf{V}$ is the Darcy velocity, u is the fluid density, and $f(u)$ is the net volumetric source term. Several modifications were implemented in the parabolic model by incorporating terms of the form

$$\theta(x)=\frac{1}{|x|^s}, \quad \operatorname{div}(u\vec{V})=\operatorname{div}\left(|\nabla u|^{p-2}\nabla u\right), \tag{8}$$

have been discussed in [36–39]. Recently, Liu and Fang [40] studied a singular epitaxial thin-film growth equation with logarithmic nonlinearity

$$\frac{u_t}{|x|^s}+\Delta^2 u+c\Delta u=|u|^{p-2}u\log|u|, \quad x\in\Omega,\ t>0, \tag{9}$$

where $2<p<2+\frac{4}{N}, c<\lambda_1$, λ_1 is the first eigenvalue of $-\Delta$ with null Dirichlet boundary condition. Under the Navier boundary and initial conditions, the results of the local and global well-posedness, blow-up with arbitrary initial energy and the lifespan were derived. Furthermore, Liu and Fang [41] also investigated a singular parabolic p-biharmonic equation with logarithmic nonlinearity

$$\frac{u_t}{|x|^s}+\Delta\left(|\Delta u|^{p-2}\Delta u\right)=|u|^{q-2}u\log|u|, \quad x\in\Omega,\ t>0, \tag{10}$$

where $\max\left\{1,\frac{2N}{N+4}\right\}<p\le q<p\left(1+\frac{4}{N}\right)$. Subject to Navier boundary and initial conditions, the results of blow-up with arbitrary initial energy and extinction phenomena were presented. Lv and Fang [25] considered a singular parabolic p-biharmonic equation with gradient-type logarithmic nonlinearity

$$\frac{u_t}{|x|^s}+\Delta\left(|\Delta u|^{p-2}\Delta u\right)+\operatorname{div}\left(|\nabla u|^{q-2}\nabla u\log|\nabla u|\right)=0, \quad x\in\Omega, t>0, \tag{11}$$

where $2<p\le q<p\left(1+\frac{2}{N+2}\right)$. Subject to Navier boundary and initial conditions, the authors adopted the Hardy-Sobolev inequality to show the finite time blow-up result with arbitrary initial energy.

Inspired by the above-mentioned research work, in this paper, we will concentrate on the initial boundary value problem (1.1) for a singular non-local fourth-order parabolic equation with gradient-dependent logarithmic nonlinearity. And we will prove the global existence of weak solution, the finite time blow-up properties of weak solution under different initial energies and the finite time extinction and

non-extinction phenomena of weak solution. The main difficulties stem from three key features: (i) the singular diffusion coefficient $\frac{1}{|x|^s}$; (ii) the logarithmic nonlinearity

$$\operatorname{div}\left(|\nabla u|^{p-2}\nabla u \log|\nabla u|\right), \tag{12}$$

and (iii) the non-local source term

$$|u|^{q-2}u - \frac{1}{|\Omega|}\int_\Omega |u|^{q-2}u\,dx, \tag{13}$$

which collectively make the methods from [12, 16, 22, 23, 42–44] inapplicable for analyzing finite-time blow-up of solutions with arbitrary initial energy levels, extinction and non-extinction behavior of solutions in finite time. In this paper, to overcome these difficulties, we develop an approach that combines truncation function techniques with Levine's concavity method [45], along with logarithmic inequalities and Hardy-Sobolev inequalities. We prove the global existence of weak solutions by utilizing the cut-off function technique and Galerkin's approximation method. We establish novel threshold criteria for the finite-time blow-up of solutions with initial value at arbitrary energy levels, and derive explicit upper bounds for the blow-up time under appropriate conditions. Furthermore, by employing energy estimates and specific ordinary differential inequalities, we characterize both non-extinction and extinction phenomena of solutions in finite time, and rigorously quantify their corresponding extinction rates.

This paper is organized as follows. In Section 2, we introduce essential notations, definitions, and preliminary lemmas that are fundamental to our main results. Section 3 is devoted to proving the global existence of weak solutions by utilizing the cut-off function technique and Galerkin's approximation method. In Section 4, under suitable assumptions, we establish threshold criteria for finite-time blow-up of solutions with arbitrary initial energy levels and derive explicit upper bounds for the blow-up time. Finally, in Section 5, we analyze both non-extinction and extinction phenomena of solutions in finite time through careful energy estimates and analysis of key ordinary differential inequalities.

2 Perliminaries

In this section, we denote the norm of $L^p(\Omega)$ for $1 \le p \le +\infty$ by

$$\|\phi\|_p = \begin{cases} \left(\int_\Omega |\phi(x)|^p\,dx\right)^{\frac{1}{p}}, & \text{si } 1 \le p < +\infty, \\ \operatorname{ess\,sup}_{x\in\Omega}|\phi(x)|, & \text{si } p = +\infty. \end{cases} \tag{14}$$

and the norm of $H^2(\Omega)$ by

$$\|\phi\|_{H^2(\Omega)} = \sqrt{\|\phi\|_2^2 + \|\nabla\phi\|_2^2 + \|\Delta\phi\|_2^2}. \tag{15}$$

Considering the initial data $u_0 \in H^2(\Omega)$ with $\int_\Omega u_0 dx = 0$ and the Neumann boundary condition to Eq. (1). As in [5] and [12], the Hilbert space $H_N^2(\Omega)$ is defined by

$$H_N^2(\Omega) := \left\{\phi \in H^2(\Omega) \,\middle|\, \left.\frac{\partial\phi}{\partial\eta}\right|_{\partial\Omega} = 0, \int_\Omega \phi\,dx = 0\right\}, \tag{16}$$

where $H_N^2(\Omega)$ is equipped with the inner product

$$(\phi,\psi) := \int_\Omega \Delta\phi\,\Delta\psi\,dx, \quad \forall\,\phi,\psi \in H_N^2(\Omega), \tag{17}$$

and the norm

$$\|\phi\|_{H_N^2(\Omega)} := \|\Delta\phi\|_2, \tag{18}$$

which is equivalent to the norm $\|\phi\|_{H^2(\Omega)}$.

We define the energy functional and Nehari functional associated to problem (1) as follows:

$$J(u) := \frac{1}{2}\|\Delta u\|_2^2 - \frac{1}{p}\int_\Omega |\nabla u|^p \log|\nabla u|\,dx + \frac{1}{p^2}\|\nabla u\|_p^p - \frac{1}{q+1}\|u\|_{q+1}^{q+1}, \tag{19}$$

$$I(u) := \|\Delta u\|_2^2 - \int_\Omega |\nabla u|^p \log|\nabla u|\,dx - \|u\|_{q+1}^{q+1}. \tag{20}$$

A direct calculation of (19) and (20) yields

$$J(u) = \frac{1}{p}I(u) + \frac{p-2}{2p}\|\Delta u\|_2^2 + \frac{1}{p^2}\|\nabla u\|_p^p + \frac{q+1-p}{p(q+1)}\|u\|_{q+1}^{q+1}. \tag{21}$$

Next, we provide a definition of a weak solution and discuss the existence of weak solutions.

Definition 1 (Weak solution) Let $T>0$. A function $u(x,t)$ is said to be a weak solution to problem (1) if $u(x,t)\in L^{\infty}\left(0,T;H_N^2(\Omega)\right)$ with $u_t\in L^2\left(0,T;L^2(\Omega)\right)$ satisfying the following conditions:
(i) for any $\varphi\in L^2\left(0,T;H^2(\Omega)\right)$ with $\frac{\partial\varphi}{\partial\eta}\Big|_{\partial\Omega}=0, t\in[0,T)$,

$$\int_0^t\int_\Omega\Big[\frac{u_\tau}{|x|^s}\varphi+\Delta u\Delta\varphi-|\nabla u|^{p-2}\nabla u\log|\nabla u|\nabla\varphi - \Big(u^q-\frac{1}{|\Omega|}\int_\Omega|u|^q dx\Big)\varphi\Big]dxd\tau=0; \tag{22}$$

(ii) $\int_0^t\left\|\frac{u_\tau(\tau)}{|x|^{\frac{s}{2}}}\right\|_2^2 d\tau<+\infty$ and $u(x,0)=u_0\in H_N^2(\Omega)$.

Moreover, the weak solutions to problem (1) satisfy the following energy equality:

$$J(u_0)=J(u)+\int_0^t\left\|\frac{u_\tau(\tau)}{|x|^{\frac{s}{2}}}\right\|_2^2 d\tau,\ \forall t\in[0,T). \tag{23}$$

Remark 1 Let T be the maximal existence time of a weak solution $u(x,t)$ to Eq. (1), defined as follows:
(i) If $u(x,t)$ exists for all $0\le t<+\infty$, then $T=+\infty$, and the weak solution exists globally.
(ii) There exists a $t_0\in(0,+\infty)$ such that $u(x,t)$ exists for $0\le t<t_0$, but does not exist at $t=t_0$, then $T=t_0$, and the weak solution exists locally and blows up in finite time.

Next, we define a function

$$S(t):=\frac{1}{2}\left\|\frac{u(t)}{|x|^{s/2}}\right\|_2^2. \tag{24}$$

And we provide two definitions for the finite-time blow-up and extinction of weak solutions.

Definition 2 (Finite time blow-up) A weak solution $u(x,t)$ to Eq. (1) is called finite time blow-up if the maximal existence time $T<+\infty$ and

$$\lim_{t\to T^-}\sqrt{2S(t)}=\lim_{t\to T^-}\left\|\frac{u(t)}{|x|^{s/2}}\right\|_2=+\infty. \tag{25}$$

Definition 3 (Finite time extinction) A weak solution $u(x,t)$ to problem (1) is called finite time extinction if the maximal existence time $T<+\infty$ and

$$\lim_{t\to T^-}\sqrt{2S(t)}=\lim_{t\to T^-}\left\|\frac{u(t)}{|x|^{s/2}}\right\|_2=0. \tag{26}$$

Finally, we present four key inequalities that play crucial roles in the analysis presented in this paper.

Lemma 1 ([28]) *Let $\rho>0$. Then, the following elementary inequalities hold:*

$$\begin{cases}\xi^p\ln\xi\le(e\rho)^{-1}\xi^{p+\rho}, & \forall\xi\ge1,\\ |\xi^p\ln\xi|\le(ep)^{-1}, & \forall0<\xi<1.\end{cases} \tag{27}$$

Lemma 2 (Bihari's inequality [46]) *Suppose that $T_0>0$ and $c_0>0$. Let $K:\mathbb{R}_+\to\mathbb{R}_+$ be a continuous nondecreasing function such that $K(t)>0$ for all $t>0$. Let $u_1(\cdot)$ be a Borel measurable bounded non-negative function on $[0,T]$, and let $v_1(\cdot)$ be a non-negative integrable function on $[0,T]$. If*

$$u_1(t)\le c_0+\int_0^t v_1(\tau)K\big(u_1(\tau)\big)d\tau,\quad \forall t\in[0,T]. \tag{28}$$

then,

$$u_1(t)\le G^{-1}\left[G(c_0)+\int_0^t v_1(\tau)d\tau\right]. \tag{29}$$

holds for all $t\in[0,T]$, and such that $G(c_0)+\int_0^t v_1(\tau)d\tau\in\mathrm{Dom}\left(G^{-1}\right)$, where

$$G(r_0)=\int_0^{r_0}\frac{d\tau}{K(\tau)},\quad r_0>0. \tag{30}$$

and G^{-1} is the inverse function of G.

Lemma 3 (Hardy-Sobolev inequality [47]) *Let $\mathbb{R}^N=\mathbb{R}^k\times\mathbb{R}^{N-k}$, where $2\le k\le N$, and $x=(y,z)\in\mathbb{R}^k\times\mathbb{R}^{N-k}$. For given λ and s satisfying $1<\lambda<N$, $0\le s\le\lambda$, $s<k$, and $\delta(s,N,\lambda)=\frac{\lambda(N-s)}{N-\lambda}$, there exists a constant $H(s,N,\lambda,k)>0$ such that*

$$\int_{\mathbb{R}^N}\frac{|u(x)|^\delta}{|y|^s}dx\le H\left(\int_{\mathbb{R}^N}|\nabla u(x)|^\lambda dx\right)^{\frac{N-s}{N-\lambda}},\quad \forall u\in W^{1,\lambda}\left(\mathbb{R}^N\right). \tag{31}$$

Remark 2 In particular, we set $k=N$ in Eq. (23), which implies $x=y\in\mathbb{R}^N$. We define $u(x)=0$ for $x\in\mathbb{R}^N\backslash\Omega$, thus,

$$\int_\Omega\frac{|u(x)|^\delta}{|x|^s}dx\le H\left(\int_\Omega|\nabla u(x)|^\lambda dx\right)^{\frac{N-s}{N-\lambda}},\quad \forall u\in W^{1,\lambda}(\Omega). \tag{32}$$

If $\delta = \frac{\lambda(N-s)}{N-\lambda} = 2$ in Eq. (32), then, by the $0 \le s \le 2, N > 2$, and the Rellich-Kondrachov theorem, we have

$$\int_\Omega \frac{|u(x)|^2}{|x|^s} dx \le H \left(\int_\Omega |\nabla u(x)|^{\frac{2N}{N-s+2}} dx \right)^{\frac{N-s+2}{N}} \le C_H \|\Delta u\|_2^2, \quad (33)$$

where $C_H = HB_0$, B_0 is the optimal embedding constant of the embedding $H_0^2(\Omega) \hookrightarrow W_0^{1,\frac{2N}{N-s+2}}(\Omega)$. Due to the boundedness of Ω, there exists a sufficiently large $L > 0$ such that $\Omega \subset B_L(0)$, and $|x| \le L$ for all $x \in \Omega$. Hence, we introduce the cut-off function

$$\rho_n := \min\left\{|x|^{-s}, n\right\}, \quad n \in \mathbb{N}^+. \quad (34)$$

to handle the singular diffusion coefficients $\frac{1}{|x|^s}$ in Eq. (1). Then, it follows from Eq. (33) that

$$\min\left\{L^{-s}, n\right\} \|u\|_2^2 \le \int_\Omega \rho_n |u|^2 dx \le C_H \|\Delta u\|_2^2, \quad \forall n \in \mathbb{N}^+. \quad (35)$$

Lemma 4 **([20])** *Suppose that $\theta > 0$, $\alpha > 0$ and $\beta > 0$. Let $\mu(t)$ be a nonnegative and absolutely continuous function satisfying*

$$\mu'(t) + \alpha \mu^\theta(t) \ge \beta. \quad (36)$$

Then, for $0 < t < +\infty$, it holds that

$$\mu(t) \ge \min\left\{\mu(0), \left(\frac{\beta}{\alpha}\right)^{\frac{1}{\theta}}\right\}. \quad (37)$$

3 Global existence

In this section, we establish the global existence of weak solutions utilizing the cut-off function technique and Galerkin's approximation method

Theorem 1 *Let $u \in H_N^2(\Omega)$. If*

$$\max\left\{2, \frac{2N}{N+2}\right\} < p < \min\left\{\frac{2N}{N-2}, \frac{2N+8}{N+2}\right\}. \quad (38)$$

and

$$1 < q < \min\left\{\frac{N+4}{N-4}, 1+\frac{8}{N}\right\}. \quad (39)$$

where $N \ge 4$. Then Eq. (1) admits a global weak solution $u = u(x,t) \in L^\infty\left(0,+\infty; H_N^2(\Omega)\right)$ with $\frac{u_t}{|x|^s} \in L^2\left(0,+\infty; L^2(\Omega)\right)$.

Proof . We intend to utilize the cut-off function technique and Galerkin's approximation method to demonstrate this theorem in four steps.

Step 1: Approximate problem We denote the solutions corresponding to ρ_n of Eq. (1) as u_n for any $n \in \mathbb{N}_+$. Let $\{\vartheta_i\}_{i=1}^{+\infty}$ be a completed orthogonal basis of $H_N^2(\Omega)$. Suppose that the finite dimensional space $U_l := \text{span}\{\vartheta_1, \vartheta_2, \cdots, \vartheta_l\}, l \in N_+$. Then the approximate solution of problem (1) can be constructed as

$$u_n^l(x,t) := \sum_{i=1}^{l} c_{ni}^l(t)\, \vartheta_i(x), \quad (40)$$

which satisfies

$$\begin{cases} \left(\rho_n u_{nt}^l, \hat{\vartheta}\right) + \left(\Delta u_n^l, \Delta \hat{\vartheta}\right) - \left(\left|\nabla u_n^l\right|^{p-2} \nabla u_n^l \log\left|\nabla u_n^l\right|, \nabla \hat{\vartheta}\right) \\ \qquad = \left(\left|u_n^l\right|^q - \frac{1}{|\Omega|}\int_\Omega \left|u_n^l\right|^q dx, \hat{\vartheta}\right), \\ u_n^l(x,0) = u_{n0}^l, \end{cases} \quad (41)$$

for any $\hat{\vartheta} \in H_N^2(\Omega)$. For a differential equation involving $c_{ni}^l(t)$, the following Cauchy problem can be obtained by taking $\hat{\vartheta} = \vartheta_i$ for $i = 1, 2, \cdots, l$:

$$\begin{cases} \left(\rho_n u_{nt}^l, \vartheta_i\right) + \left(\Delta u_n^l, \Delta \vartheta_i\right) \\ \qquad - \left(\left|\nabla u_n^l\right|^{p-2} \nabla u_n^l \log\left|\nabla u_n^l\right|, \nabla \vartheta_i\right) \\ \qquad = \left(\left|u_n^l\right|^q - \frac{1}{|\Omega|}\int_\Omega \left|u_n^l\right|^q dx, \vartheta_i\right), \\ \left(u_{n0}^l, \vartheta_i\right) = b_{ni}^l, \end{cases} \quad (42)$$

where b_{ni}^l are constants satisfying

$$u_n^l(x,0)=\sum_{i=1}^{l} b_{ni}^l\,\vartheta_i(x)\longrightarrow u_0(x) \tag{43}$$

in $H_N^2(\Omega)$ as $n\to+\infty$ and $l\to+\infty$. By the Picard iteration theorem of ODEs, there exists a $T>0$ such that $c_{ni}^l(t)\in C^1[0,T]$. And thus, it follows from Eq. (40) that

$$u_n^l\in C^1\left([0,T],H_N^2(\Omega)\right). \tag{44}$$

From this, we obtain the local existence of solution to Eq. (1).

Next, we prove the global existence of solution by estimating on the boundness of u_n^l in any finite time.

Step 2: Priori estimates Multiplying the first of the equations of Eq. (42) by $c_{ni}^l(t)$ and summing over $i=1,2,\cdots,l$, we obtain

$$\begin{aligned}&\left(\rho_n u_{nt}^l,u_n^l\right)+\left(\Delta u_n^l,\Delta u_n^l\right)\\&\quad-\left(\left|\nabla u_n^l\right|^{p-2}\nabla u_n^l\log\left|\nabla u_n^l\right|,\nabla u_n^l\right)\\&\quad=\left(\left|u_n^l\right|^q-\frac{1}{|\Omega|}\int_\Omega\left|u_n^l\right|^q dx,u_n^l\right).\end{aligned} \tag{45}$$

Integrating Eq. (45) over $(0,t)$, we obtain

$$\begin{aligned}&\frac{1}{2}\int_\Omega\rho_n\left|u_n^l\right|^2dx-\frac{1}{2}\int_\Omega\rho_n\left|u_{n0}^l\right|^2dx+\int_0^t\left\|\Delta u_n^l\right\|_2^2d\tau\\&\quad=\int_0^t\int_\Omega\left|\nabla u_n^l\right|^p\log\left|\nabla u_n^l\right|dxd\tau\\&\quad+\int_0^t\int_\Omega\left(\left|u_n^l\right|^q-\frac{1}{|\Omega|}\int_\Omega\left|u_n^l\right|^q dx\right)u_n^l dxd\tau.\end{aligned} \tag{46}$$

Setting $F(t)=\frac{1}{2}\int_\Omega\rho_n\left|u_n^l\right|^2dx+\int_0^t\left\|\Delta u_n^l\right\|_2^2d\tau$, then $F(0)=\frac{1}{2}\int_\Omega\rho_n\left|u_{n0}^l\right|^2dx$. Therefore, we rewrite Eq. (46) as

$$\begin{aligned}F(t)-F(0)&=\int_0^t\int_\Omega\left|\nabla u_n^l\right|^p\log\left|\nabla u_n^l\right|dxd\tau\\&+\int_0^t\int_\Omega\left(\left|u_n^l\right|^q-\frac{1}{|\Omega|}\int_\Omega\left|u_n^l\right|^q dx\right)u_n^l dxd\tau.\end{aligned} \tag{47}$$

By Lemma 1, Nirenberg's inequality and Young's inequality with ε, there exists a constant C_1 and a sufficiently small $\rho_1>0$ such that

$$\begin{aligned}&\int_\Omega\left|\nabla u_n^l\right|^p\log\left|\nabla u_n^l\right|dx\\&\le(\mathrm{e}\rho_1)^{-1}\left\|\nabla u_n^l\right\|_{p+\rho_1}^{p+\rho_1}\\&\le(\mathrm{e}\rho_1)^{-1}C_1^{p+\rho_1}\left\|\Delta u_n^l\right\|_2^{r_1(p+\rho_1)}\left\|u_n^l\right\|_2^{(1-r_1)(p+\rho_1)}\\&\le(\mathrm{e}\rho_1)^{-1}C_1^{p+\rho_1}\varepsilon\left\|\Delta u_n^l\right\|_2^2\\&+(\mathrm{e}\rho_1)^{-1}C_1^{p+\rho_1}\frac{2-r_1(p+\rho_1)}{2}\\&\times\left(\frac{2\varepsilon}{r(p+\rho_1)}\right)^{-\frac{r_1(p+\rho_1)}{2-r_1(p+\rho_1)}}\left\|u_n^l\right\|_2^{2m_1}\\&=C_1(\varepsilon)\left\|\Delta u_n^l\right\|_2^2+\bar{C}_1(\varepsilon)\left\|u_n^l\right\|_2^{2m_1},\end{aligned} \tag{48}$$

where

$$r_1=\frac{(N+2)(p+\rho_1)-2N}{4(p+\rho_1)}\in(0,1), \tag{49}$$

$$m_1=\frac{(1-r_1)(p+\rho_1)}{2-r_1(p+\rho_1)}>1. \tag{50}$$

Additionally, following a similar approach to Eq. (48), we know that there exists a constant C_2 such that

$$\begin{aligned}&\int_\Omega\left(\left|u_n^l\right|^q-\frac{1}{|\Omega|}\int_\Omega\left|u_n^l\right|^q dx\right)u_n^l dx\\&\le\int_\Omega\left|u_n^l\right|^{q+1}dx-\frac{1}{|\Omega|}\int_\Omega\left|u_n^l\right|^q dx\int_\Omega u_n^l dx\\&=\int_\Omega\left|u_n^l\right|^{q+1}dx\\&\le C_2^{q+1}\left\|\Delta u_n^l\right\|_2^{r_2(q+1)}\left\|u_n^l\right\|_2^{(1-r_2)(q+1)}\\&\le C_2^{q+1}\varepsilon\left\|\Delta u_n^l\right\|_2^2\\&+C_2^{q+1}\frac{2-r_2(q+1)}{2}\left(\frac{2\varepsilon}{r_2(q+1)}\right)^{-\frac{r_2(q+1)}{2-r_2(q+1)}}\left\|u_n^l\right\|_2^{2m_2}\\&=C_2(\varepsilon)\left\|\Delta u_n^l\right\|_2^2+\bar{C}_2(\varepsilon)\left\|u_n^l\right\|_2^{2m_2},\end{aligned} \tag{51}$$

where

$$r_2=\frac{N(q-1)}{4(q+1)}\in(0,1),\quad m_2=\frac{(1-r_2)(q+1)}{2-r_2(q+1)}>1. \tag{52}$$

Thus, it can be obtained from Eq. (35) and Eqs (47)-(51) that

$$F(t)-F(0)\leq\int_0^t\left(C_1(\varepsilon)\left\|\Delta u_n^l\right\|_2^2+\bar{C}_1(\varepsilon)\left\|u_n^l\right\|_2^{2m_1}\right)d\tau+\int_0^t\left(C_2(\varepsilon)\left\|\Delta u_n^l\right\|_2^2+\bar{C}_2(\varepsilon)\left\|u_n^l\right\|_2^{2m_2}\right)d\tau$$

$$\begin{aligned}
\leq & C_1(\varepsilon)\left(\frac{1}{2}\int_\Omega\rho_n\left|u_n^l\right|^2dx+\int_0^t\left\|\Delta u_n^l\right\|_2^2d\tau\right)+C_2(\varepsilon)\left(\frac{1}{2}\int_\Omega\rho_n\left|u_n^l\right|^2dx+\int_0^t\left\|\Delta u_n^l\right\|_2^2d\tau\right)\\
&+\bar{C}_1(\varepsilon)\int_0^t\frac{1}{\min\{L^{-s},n\}^{m_1}}\cdot\min\{L^{-s},n\}^{m_1}\left\|u_n^l\right\|_2^{2m_1}d\tau+\bar{C}_2(\varepsilon)\int_0^t\frac{1}{\min\{L^{-s},n\}^{m_2}}\cdot\min\{L^{-s},n\}^{m_2}\left\|u_n^l\right\|_2^{2m_2}d\tau\\
\leq & C_3(\varepsilon)F(t)+\frac{\bar{C}_1(\varepsilon)}{\min\{L^{-s},n\}^{m_1}}\int_0^t\left(\int_\Omega\rho_n\left|u_n^l\right|^2dx\right)^{m_1}d\tau+\frac{\bar{C}_2(\varepsilon)}{\min\{L^{-s},n\}^{m_2}}\int_0^t\left(\int_\Omega\rho_n\left|u_n^l\right|^2dx\right)^{m_2}d\tau\\
\leq & C_3(\varepsilon)F(t)+\frac{\bar{C}_1(\varepsilon)}{\min\{L^{-s},n\}^{m_1}}\int_0^t\left(\int_\Omega\rho_n\left|u_n^l\right|^2dx+2\int_0^t\left\|\Delta u_n^l\right\|_2^2d\tau\right)^{m_1}d\tau\\
&+\frac{\bar{C}_2(\varepsilon)}{\min\{L^{-s},n\}^{m_2}}\int_0^t\left(\int_\Omega\rho_n\left|u_n^l\right|^2dx+2\int_0^t\left\|\Delta u_n^l\right\|_2^2d\tau\right)^{m_2}d\tau\\
= & C_3(\varepsilon)F(t)+\bar{C}_3(\varepsilon)\int_0^t[(F(\tau))^{m_1}+(F(\tau))^{m_2}]d\tau,
\end{aligned}\tag{53}$$

which implies

$$\begin{aligned}
F(t)\leq\ & \frac{F(0)}{1-C_3(\varepsilon)}\\
&+\frac{\bar{C}_3(\varepsilon)}{1-C_3(\varepsilon)}\int_0^t[F(\tau)^{m_1}+F(\tau)^{m_2}]d\tau.
\end{aligned}\tag{54}$$

where

$$C_3(\varepsilon)=C_1(\varepsilon)+C_2(\varepsilon),\tag{55}$$

$$\bar{C}_3(\varepsilon)=\max\left\{\frac{2^{m_1}\bar{C}_1(\varepsilon)}{\min\{L^{-s},n\}^{m_1}},\frac{2^{m_2}\bar{C}_2(\varepsilon)}{\min\{L^{-s},n\}^{m_2}}\right\}.\tag{56}$$

By Lemma 2, there exists a $T>0$ such that

$$F(t)\leq\Phi^{-1}\left[\Phi\left(\frac{F(0)}{1-C_3(\varepsilon)}\right)+\frac{\bar{C}_3(\varepsilon)}{1-C_3(\varepsilon)}t\right].\tag{57}$$

where $\Phi(r_1)=\int_0^{r_1}\frac{d\tau}{(F(\tau))^{m_1}+(F(\tau))^{m_2}}$, $r_1>0$. Therefore, we have $F(t)\leq C_T$, which means

$$\frac{1}{2}\int_\Omega\rho_n\left|u_n^l\right|^2dx+\int_0^t\left\|\Delta u_n^l\right\|_2^2d\tau\leq C_T,\ \forall n,l\in\mathbb{N}_+.\tag{58}$$

Multiplying the first equation of (42) by $\frac{d}{dt}c_{ni}^l(t)$, summing over $i=1,2,\cdots,l$, and integrating (45) over $(0,t)$, we obtain

$$J\left(u_{n0}^l\right)=J\left(u_n^l\right)+\int_0^t\int_\Omega\rho_n\left|u_{n\tau}^l\right|^2dxd\tau.\tag{59}$$

By the continuity of $J(u(t))$ and Eq. (42), we can know that there exists a $\hat{C}>0$ such that

$$J\left(u_{n0}^l\right)\leq\hat{C},\ \forall n,l\in\mathbb{N}_+.\tag{60}$$

From Eqs (19), (59) and Eqs (60), we derive

$$\begin{aligned}
&\hat{C}\geq J\left(u_{n0}^l\right)\geq J\left(u_n^l\right)\\
=&\frac{1}{2}\left\|\Delta u_n^l\right\|_2^2-\frac{1}{p}\int_\Omega\left|\nabla u_n^l\right|^p\log\left|\nabla u_n^l\right|dx\\
&+\frac{1}{p^2}\left\|\nabla u_n^l\right\|_p^p-\frac{1}{q+1}\left\|u_n^l\right\|_{q+1}^{q+1}\\
\geq&\left[\frac{1}{2}-\frac{C_1(\varepsilon)}{p}-\frac{C_2(\varepsilon)}{q+1}\right]\left\|\Delta u_n^l\right\|_2^2-\frac{\bar{C}_1(\varepsilon)}{p}\left\|u_n^l\right\|_2^{2m_1}\\
&+\frac{1}{p^2}\left\|\nabla u_n^l\right\|_p^p-\frac{\bar{C}_2(\varepsilon)}{q+1}\left\|u_n^l\right\|_2^{2m_2}\\
\geq&\left[\frac{1}{2}-\frac{C_1(\varepsilon)}{p}-\frac{C_2(\varepsilon)}{q+1}\right]\left\|\Delta u_n^l\right\|_2^2\\
&+\frac{1}{p^2}\left\|\nabla u_n^l\right\|_p^p-\frac{2^{m_1}\bar{C}_1(\varepsilon)}{p\min\{L^{-s},n\}^{m_1}}(F(t))^{m_1}\\
&-\frac{2^{m_2}\bar{C}_2(\varepsilon)}{(q+1)\min\{L^{-s},n\}^{m_2}}(F(t))^{m_2}.
\end{aligned}\tag{61}$$

Combining Eqs (58) and (61), we obtain

$$\left\|\rho_n^{\frac{1}{2}} u_{nt}^l\right\|_{L^2\left(0,T;L^2(\Omega)\right)} \leq C,\ \forall n,l \in \mathbb{N}_+, \tag{62}$$

$$\left\|u_n^l\right\|_{L^\infty\left(0,T;H_0^2(\Omega)\right)} \leq C,\ \forall n,l \in \mathbb{N}_+, \tag{63}$$

$$\left\|u_n^l\right\|_{L^\infty\left(0,T;W_0^{1,p}(\Omega)\right)} \leq C,\ \forall n,l \in \mathbb{N}_+, \tag{64}$$

$$\left\|u_n^l\right\|_{L^\infty\left(0,T;L^{q+1}(\Omega)\right)} \leq C,\ \forall n,l \in \mathbb{N}_+. \tag{65}$$

Step 3: Pass to the limit Since $u_n^l \in C^1\left([0,T];H_N^2(\Omega)\right)$ and Eq. (63), then $\left\{u_n^l\right\}$ is a uniformly bounded and equicontinuous sequence. Thus, by the Arzela-Ascoli theorem and Eqs (62)-(65), there exist a function u and a subsequence of $\left\{u_n^l\right\}_{n,l=1}^{+\infty}$, which we still denote by $\left\{u_n^l\right\}_{n,l=1}^{+\infty}$, for convenience, such that

$$u_{nt}^l \to u_t \ strongly\ in\ L^2\left(0,T;L^2(\Omega)\right), \tag{66}$$

$$u_n^l \to u\ weakly\ star\ in\ L^\infty\left(0,T;H_0^2(\Omega)\right), \tag{67}$$

$$u_n^l \to u\ weakly\ star\ in\ L^\infty\left(0,T;W_0^{1,p}(\Omega)\right), \tag{68}$$

$$u_n^l \to u\ weakly\ star\ in\ L^\infty\left(0,T;L^{q+1}(\Omega)\right). \tag{69}$$

Combining Eqs (66)-(69) and the Aubin-Lions-Simon theorem, we have

$$u_n^l \to u, \nabla u_n^l \to \nabla u\ strongly\ in\ C\left([0,T];L^2(\Omega)\right), \tag{70}$$

which implies $u_n^l \to u, \nabla u_n^l \to \nabla u,\ a.e.\ \Omega \times (0,T)$. Therefore,

$$\left|\nabla u_n^l\right|^{p-2} \nabla u_n^l \log\left|\nabla u_n^l\right| \to |\nabla u|^{p-2} \nabla u \log|\nabla u|,\ a.e.\ \Omega \times (0,T). \tag{71}$$

Additionally, we define

$$\Omega_1 := \{x \in \Omega \mid |u_n^l(x)| \leq 1\}, \quad \Omega_2 := \{x \in \Omega \mid |u_n^l(x)| > 1\}. \tag{72}$$

Then, from Lemma 1, it follows that there exists a constant $\rho_2 = 1$ such that

$$\begin{aligned}
&\int_\Omega \left(\left|\nabla u_n^l\right|^{p-2} \nabla u_n^l \log\left|\nabla u_n^l\right|\right)^{p'} dx \\
=&\int_{\Omega_1} \left(\left|\nabla u_n^l\right|^{p-2} \nabla u_n^l \log\left|\nabla u_n^l\right|\right)^{p'} dx \\
&+ \int_{\Omega_2} \left(\left|\nabla u_n^l\right|^{p-2} \nabla u_n^l \log\left|\nabla u_n^l\right|\right)^{p'} dx \\
\leq&[e(p-1)]^{-p'} |\Omega| + \frac{1}{e\rho_2} \int_{\Omega_2} \left(\left|\nabla u_n^l\right|^{p-1+\rho_2}\right)^{p'} dx \\
=&[e(p-1)]^{-p'} |\Omega| + e^{-p'} \int_{\Omega_2} \left(\left|\nabla u_n^l\right|^p\right)^{p'} dx \leq C.
\end{aligned} \tag{73}$$

Hence, by Eqs (71) and (73), we have

$$\left|\nabla u_n^l\right|^{p-2} \nabla u_n^l \log\left|\nabla u_n^l\right| \to |\nabla u|^{p-2} \nabla u \log|\nabla u|\ \ weakly\ star\ in\ L^\infty\left(0,T;L^{p'}(\Omega)\right). \tag{74}$$

In order to show the limit u in Eqs (66)-(69) and (74) is a weak solution to problem (1), we proceed as follows. Fix a positive integer $k \in \mathbb{N}_+$ satisfying $k \leq l$. For the given smooth function $\left\{d_{ni}^l(t)\right\}_{i=1}^k$, we choose a function $\vartheta(x,t) = \sum_{i=1}^k d_{ni}^l(t)$ where $\vartheta_i \in C^1\left([0,T],H_N^2(\Omega)\right)$. Multiplying the first equation of Eq. (42) by $d_{ni}^l(t)$, summing for i from 1 to k and then integrate it with respect to t, we obtain

$$\begin{aligned}
&\int_0^T \left(\rho_n u_{nt}^l, \vartheta\right) + \left(\Delta u_n^l, \Delta\vartheta\right) \\
&\quad - \left(\left|\nabla u_n^l\right|^{p-2} \nabla u_n^l \log\left|\nabla u_n^l\right|, \nabla\vartheta\right) dt \\
&\quad = \int_0^T \left(\left|u_n^l\right|^q - \frac{1}{|\Omega|} \int_\Omega \left|u_n^l\right|^q dx, \vartheta\right) dt.
\end{aligned} \tag{75}$$

Taking $n \to +\infty, l \to +\infty$ in Eq. (75), and using $\lim_{n\to+\infty} \rho_n = |x|^{-s}$ and the convergence results established above, we conclude that

$$\int_0^T \left(|x|^{-s}u_t,\vartheta\right)+(\Delta u,\Delta\vartheta) - \left(|\nabla u|^{p-2}\nabla u\log|\nabla u|,\nabla\vartheta\right)dt = \int_0^T\left(|u|^q-\frac{1}{|\Omega|}\int_\Omega |u|^q dx,\vartheta\right)dt. \tag{76}$$

Since ϑ is dense in $L^2\left([0,T],H_N^2(\Omega)\right)$, Eq. (76) holds for all $\vartheta\in L^2\left([0,T],H_N^2(\Omega)\right)$. Therefore, u is a global weak solution to Eq. (1).

Step 4: Uniqueness Assume that there are different functions $\bar{u}(x,t)$, $\bar{v}(x,t)$ as bounded weak solutions to problem (1) with the initial condition $\bar{u}(x,0)=\bar{v}(x,0)=u_0\in H_N^2(\Omega)$. Then, we have

$$\left(|x|^{-s}\bar{u}_t,\vartheta\right)+(\Delta\bar{u},\Delta\vartheta)-\left(|\nabla\bar{u}|^{p-2}\nabla\bar{u}\log|\nabla\bar{u}|,\nabla\vartheta\right) = \left(|\bar{u}|^q-\frac{1}{|\Omega|}\int_\Omega|\bar{u}|^q dx,\vartheta\right), \tag{77}$$

$$\left(|x|^{-s}\bar{v}_t,\vartheta\right)+(\Delta\bar{v},\Delta\vartheta)-\left(|\nabla\bar{v}|^{p-2}\nabla\bar{v}\log|\nabla\bar{v}|,\nabla\vartheta\right) = \left(|\bar{v}|^q-\frac{1}{|\Omega|}\int_\Omega|\bar{v}|^q dx,\vartheta\right), \tag{78}$$

for any $\vartheta\in H_N^2(\Omega)$. Then, we have

$$\begin{aligned}&\left(|x|^{-s}(\bar{u}-\bar{v})_t,\vartheta\right)+\left(\Delta(\bar{u}-\bar{v}),\Delta\vartheta\right)\\ &-\left(|\nabla\bar{u}|^{p-2}\nabla\bar{u}\log|\nabla\bar{u}|-|\nabla\bar{v}|^{p-2}\nabla\bar{v}\log|\nabla\bar{v}|,\nabla\vartheta\right)\\ &=\left(|\bar{u}|^q-\frac{1}{|\Omega|}\int_\Omega|\bar{u}|^q dx-\left(|\bar{v}|^q-\frac{1}{|\Omega|}\int_\Omega|\bar{v}|^q dx\right),\vartheta\right).\end{aligned} \tag{79}$$

We choose the test function in (79) as

$$\vartheta(\tau)=\begin{cases}\bar{u}(\tau)-\bar{v}(\tau), & \text{if } \tau\in[0,t],\\ 0, & \text{if } \tau\in(t,T).\end{cases} \tag{80}$$

which implies that Eq. (79) can be rewritten as

$$\begin{aligned}&\left(|x|^{-s}(\bar{u}-\bar{v})_t,\bar{u}-\bar{v}\right)+\left(\Delta(\bar{u}-\bar{v}),\Delta(\bar{u}-\bar{v})\right)\\ &-\left(|\nabla\bar{u}|^{p-2}\nabla\bar{u}\log|\nabla\bar{u}|-|\nabla\bar{v}|^{p-2}\nabla\bar{v}\log|\nabla\bar{v}|,\nabla(\bar{u}-\bar{v})\right)\\ &=\left(|\bar{u}|^q-\frac{1}{|\Omega|}\int_\Omega|\bar{u}|^q dx-\left(|\bar{v}|^q-\frac{1}{|\Omega|}\int_\Omega|\bar{v}|^q dx\right),\bar{u}-\bar{v}\right).\end{aligned} \tag{81}$$

Integrating over $(0,t)$, we obtain

$$\begin{aligned}&\frac{1}{2}\left\|\frac{\bar{u}-\bar{v}}{|x|^{\frac{s}{2}}}\right\|_2^2+\int_0^t\int_\Omega|\Delta(\bar{u}-\bar{v})|^2dxd\tau\\ &=\int_0^t\int_\Omega\left(|\nabla\bar{u}|^{p-2}\nabla\bar{u}\log|\nabla\bar{u}|-|\nabla\bar{v}|^{p-2}\nabla\bar{v}\log|\nabla\bar{v}|\right)\\ &\quad\times(\nabla\bar{u}-\nabla\bar{v})dxd\tau\\ &+\int_0^t\int_\Omega\left[|\bar{u}|^q-\frac{1}{|\Omega|}\int_\Omega|\bar{u}|^q dx-\left(|\bar{v}|^q-\frac{1}{|\Omega|}\int_\Omega|\bar{v}|^q dx\right)\right]\\ &\quad\times(\bar{u}-\bar{v})dxd\tau.\end{aligned} \tag{82}$$

Define

$$Q_1(\tau):=|\tau|^{p-2}\tau\log|\tau|, \tag{83}$$

$$Q_2(\tau):=|\tau|^q-\frac{1}{|\Omega|}\int_\Omega|\tau|^q dx. \tag{84}$$

By the Lipschitz continuity of $Q_j:\mathbb{R}_+\to\mathbb{R}_+$ for all $j=1,2$, we derive

$$\begin{aligned}&\frac{1}{2}\left\|\frac{\bar{u}-\bar{v}}{|x|^{\frac{s}{2}}}\right\|_2^2+\int_0^t\int_\Omega|\Delta(\bar{u}-\bar{v})|^2dxd\tau\\ &=\int_0^t\int_\Omega\left(Q_1(\nabla\bar{u})-Q_1(\nabla\bar{v})\right)(\nabla\bar{u}-\nabla\bar{v})dxd\tau\\ &\quad+\int_0^t\int_\Omega\left[Q_2(\bar{u})-Q_2(\bar{v})\right](\bar{u}-\bar{v})dxd\tau\\ &\le C_4\int_0^t\int_\Omega|\nabla\bar{u}-\nabla\bar{v}|^2dxd\tau+C_5\int_0^t\int_\Omega|\bar{u}-\bar{v}|^2dxd\tau.\end{aligned} \tag{85}$$

Taking $\omega=\bar{u}-\bar{v}$, from Nirenberg's inequality and Young's inequality with ε, we obtain

$$\begin{aligned}&\frac{1}{2}\left\|\frac{\omega}{|x|^{\frac{s}{2}}}\right\|_2^2+\int_0^t\int_\Omega|\Delta\omega|^2dxd\tau\\ &\le C_4\int_0^t\int_\Omega|\nabla\omega|^2dxd\tau+C_5\int_0^t\int_\Omega|\omega|^2dxd\tau\\ &\le C_4C_6^2\int_0^t\|\Delta\omega\|_2\|\omega\|_2d\tau+C_5\int_0^t\int_\Omega|\omega|^2dxd\tau\\ &\le\varepsilon C_4C_6^2\int_0^t\|\Delta\omega\|_2^2d\tau+\left[(4\varepsilon)^{-1}C_4C_6^2+C_5\right]\int_0^t\|\omega\|_2^2d\tau.\end{aligned} \tag{86}$$

Let $\varepsilon=\left(C_4C_6^2\right)^{-1}$ and $C_7=\frac{C_4^2C_6^4}{4}+C_5$. Then, we derive

$$\begin{aligned}\frac{1}{2}\left\|\frac{\omega}{|x|^{\frac{s}{2}}}\right\|_2^2 \leq & C_7\int_0^t \|\omega\|_2^2 d\tau \\ = & C_7\int_0^t\int_\Omega |x|^s\cdot\frac{|\omega|^2}{|x|^s}dxd\tau \\ \leq & C_7L^s\int_0^t\left\|\frac{\omega}{|x|^{\frac{s}{2}}}\right\|_2^2 d\tau. \end{aligned} \tag{87}$$

By Gronwall's inequality, we have

$$\left\|\frac{\omega}{|x|^{\frac{s}{2}}}\right\|_2 = \left\|\frac{\bar{u}-\bar{v}}{|x|^{\frac{s}{2}}}\right\|_2 = 0, \quad \text{i.e., } \bar{u}=\bar{v}. \tag{88}$$

which contradicts the assumption. Thus, Eq. (1) admits a weak solution in $\Omega\times[0,T]$. Next, we consider Eq. (1) in $\Omega\times[(k-1)T,kT]$ for all $k=2,3,\cdots$. Finally, we conclude that Eq. (1) admits a global weak solution.

The proof is completed.

4 Blow-up in finite time

In this section, we not only derive new threshold results for the finite-time blow-up of solutions with initial value at arbitrary energy levels, but also determine the upper bounds for the blow-up time under appropriate conditions.

Theorem 2 *Let $2<p<q+1$. If $J(u_0)<0$, then the solution to problem (1) blows up in finite time t_*. Moreover, the upper bound of t_* is estimated as*

$$t_* \leq \frac{\left\|\frac{u_0}{|x|^{\frac{s}{2}}}\right\|_2^2}{p(2-p)J(u_0)}. \tag{89}$$

Proof . We define a function

$$\gamma(t) := -J(u(t)). \tag{90}$$

It is straightforward to observe that $S(0)=\frac{1}{2}\left\|\frac{u_0}{|x|^{\frac{s}{2}}}\right\|_2^2>0$ and $\gamma(0)=-J(u_0)>0$. Since the weak solution to problem (1) satisfies the following energy equality

$$J(u_0)=J(u)+\int_0^t\left\|\frac{u_\tau(\tau)}{|x|^{\frac{s}{2}}}\right\|_2^2 d\tau, \tag{91}$$

we obtain

$$\begin{aligned}\gamma'(t) = & -\frac{d}{dt}J(u(t)) = \frac{d}{dt}\int_0^t\left\|\frac{u_\tau(\tau)}{|x|^{\frac{s}{2}}}\right\|_2^2 d\tau - \frac{d}{dt}J(u_0) \\ = & \left\|\frac{u_t(t)}{|x|^{\frac{s}{2}}}\right\|_2^2 \geq 0. \end{aligned} \tag{92}$$

From Eq. (92), it follows that

$$0<\gamma(0)\leq\gamma(t), \quad \forall t\in[0,t_*). \tag{93}$$

Based on Eqs (20), (21) and the condition $2<p<q+1$, we derive

$$\begin{aligned} S'(t) = & \int_\Omega \frac{u(t)u_t(t)}{|x|^s}dx = -I(u(t)) \\ = & -pJ(u(t))+\frac{p-2}{2}\|\Delta u(t)\|_2^2 \\ & +\frac{1}{p}\|\nabla u(t)\|_p^p+\frac{q+1-p}{q+1}\|u(t)\|_{q+1}^{q+1} \geq -pJ(u(t)). \end{aligned} \tag{94}$$

which implies

$$S'(t)\geq -pJ(u(t)) = p\gamma(t)>0, \ \forall t\leq[0,t_*). \tag{95}$$

Using Eqs (92), (95) and the Cauchy-Schwartz inequality, we obtain

$$\begin{aligned} S(t)\gamma'(t) = & \frac{1}{2}\left\|\frac{u(t)}{|x|^{\frac{s}{2}}}\right\|_2^2\left\|\frac{u_t(t)}{|x|^{\frac{s}{2}}}\right\|_2^2 \\ \geq & \frac{1}{2}\left(\int_\Omega\frac{u(t)u_t(t)}{|x|^s}dx\right)^2 \geq \frac{p}{2}S'(t)\gamma(t). \end{aligned} \tag{96}$$

Thus, via direct calculation using Eq. (96), we have

$$\begin{aligned}\left[S^{-\frac{p}{2}}(t)\gamma(t)\right]' = & \\ & S^{-\frac{p}{2}-1}(t)\left[S(t)\gamma'(t)-\tfrac{p}{2}S'(t)\gamma(t)\right]\geq 0. \end{aligned} \tag{97}$$

It follows that

$$0 < S^{-\frac{p}{2}}(0)\gamma(0) \le S^{-\frac{p}{2}}(t)\gamma(t) \le \frac{2}{p(2-p)}\left(S^{-\frac{p}{2}+1}(t)\right)', \tag{98}$$

and since $\frac{2}{p(2-p)} < 0$, we deduce

$$\left(S^{-\frac{p}{2}+1}(t)\right)' \le \frac{p(2-p)}{2} S^{-\frac{p}{2}}(0)\,\gamma(0). \tag{99}$$

Integrating over $(0,t)$ yields

$$S^{-\frac{p}{2}+1}(t) \le \frac{p(2-p)}{2} S^{-\frac{p}{2}}(0)\,\gamma(0)t + S^{-\frac{p}{2}+1}(0). \tag{100}$$

Taking he limi $t \to t_*$ in Eq. (100) to obtain

$$\lim_{t\to t_*^-} S^{-\frac{p}{2}+1}(t) = \frac{1}{\lim_{t\to t_*^-} S^{\frac{p}{2}-1}(t)} = 0. \tag{101}$$

which implies

$$\lim_{t\to t_*^-} S(t) = \lim_{t\to t_*^-} \frac{1}{2}\left\|\frac{u(t)}{|x|^{s/2}}\right\|_2^2 = +\infty. \tag{102}$$

The proof is completed.

Theorem 3 *Let $2 < p < q+1$. If $0 \le J(u_0) < \frac{p-2}{2pC_H}\left\|\frac{u_0}{|x|^{\frac{s}{2}}}\right\|_2^2$, then the solution to problem (1) blows up in finite time t_*, and the upper bound of t_* is estimated as*

$$t_* \le \frac{8p\left\|\frac{u_0}{|x|^{s/2}}\right\|_2^2}{(p-2)^2\left[\frac{(p-2)}{C_H}\left\|\frac{u_0}{|x|^{s/2}}\right\|_2^2 - 2pJ(u_0)\right]}. \tag{103}$$

Proof . Suppose that u is a solution of the Eq. (1) with initial data u_0. We observe that

$$\int_0^t \left\|\frac{u_\tau(\tau)}{|x|^{\frac{s}{2}}}\right\|_2 d\tau \ge \left\|\int_0^t \frac{u_\tau(\tau)}{|x|^{\frac{s}{2}}} d\tau\right\|_2 = \left\|\frac{u(t)}{|x|^{\frac{s}{2}}} - \frac{u_0}{|x|^{\frac{s}{2}}}\right\|_2 \ge \left\|\frac{u(t)}{|x|^{\frac{s}{2}}}\right\|_2 - \left\|\frac{u_0}{|x|^{\frac{s}{2}}}\right\|_2, \quad \forall t \in [0,+\infty). \tag{104}$$

Though a direct calculation, we obtain

$$\begin{aligned}\left\|\frac{u(t)}{|x|^{\frac{s}{2}}}\right\|_2 &\le \left\|\frac{u_0}{|x|^{\frac{s}{2}}}\right\|_2 + \int_0^t \left\|\frac{u_\tau(\tau)}{|x|^{\frac{s}{2}}}\right\|_2 d\tau \\ &\le \left\|\frac{u_0}{|x|^{\frac{s}{2}}}\right\|_2 + t^{\frac{1}{2}}\left(\int_0^t \left\|\frac{u_\tau(\tau)}{|x|^{\frac{s}{2}}}\right\|_2^2 d\tau\right)^{\frac{1}{2}} \\ &= \left\|\frac{u_0}{|x|^{\frac{s}{2}}}\right\|_2 + t^{\frac{1}{2}}\left(J(u_0) - J(u(t))\right)^{\frac{1}{2}}.\end{aligned} \tag{105}$$

Suppose u is a global weak solution of Eq. (1). We know $J(u(t)) \ge 0$ for all $t \in [0,+\infty)$. If this were false, there would exist $t_0 \in (0,+\infty)$ such that $J(u(t_0)) < 0$. Following the proof of Theorem 2, we conclude that u blows up in finite time, contradicting our assumption. Therefore, from Eq. (105), we obtain

$$\begin{aligned}\left\|\frac{u(t)}{|x|^{\frac{s}{2}}}\right\|_2 &\le \left\|\frac{u_0}{|x|^{\frac{s}{2}}}\right\|_2 + t^{\frac{1}{2}}\left(J(u_0) - J(u(t))\right)^{\frac{1}{2}} \\ &\le \left\|\frac{u_0}{|x|^{\frac{s}{2}}}\right\|_2 + t^{\frac{1}{2}}\left(J(u_0)\right)^{\frac{1}{2}}, \quad \forall t \in [0,+\infty).\end{aligned} \tag{106}$$

Furthermore, from the definition of $S(t)$ and using Eqs (20), (21), (33) with the condition $2 < p < q+1$, we derive

$$\begin{aligned}S'(t) &= -pJ(u(t)) + \frac{p-2}{2}\|\Delta u(t)\|_2^2 + \frac{1}{p}\|\nabla u(t)\|_p^p + \frac{q+1-p}{q+1}\|u(t)\|_{q+1}^{q+1} \\ &\ge -pJ(u(t)) + \frac{p-2}{2C_H}\left\|\frac{u(t)}{|x|^{\frac{s}{2}}}\right\|_2^2 \\ &= \frac{p-2}{C_H}\left[S(t) - \frac{pC_H}{p-2}J(u(t))\right].\end{aligned} \tag{107}$$

From Eq. (92) , it follows that

$$\frac{d}{dt}J(u(t)) = -\left\|\frac{u_t(t)}{|x|^{\frac{s}{2}}}\right\|_2^2 \le 0. \tag{108}$$

Then, from Eqs (107) and (108), it yields

$$\begin{aligned}\frac{d}{dt}\left(S(t) - \frac{pC_H}{p-2}J(u(t))\right) &\ge \frac{d}{dt}S(t) \\ &\ge \frac{p-2}{C_H}\left[S(t) - \frac{pC_H}{p-2}J(u(t))\right].\end{aligned} \tag{109}$$

Let $\varphi(t) = S(t) - \frac{pC_H}{p-2} J(u(t))$, from Eq. (109), we have

$$\frac{d}{dt}\varphi(t) \geq \frac{p-2}{C_H}\varphi(t), \ \forall t \in [0,+\infty). \tag{110}$$

Integrating Eq. (110) over $(0,t)$, we obtain

$$\varphi(t) \geq \mathrm{e}^{\frac{p-2}{C_H}t}\varphi(0), \quad \forall t \in [0,+\infty). \tag{111}$$

namely,

$$\left\| \frac{u(t)}{|x|^{\frac{s}{2}}} \right\|_2^2 \geq \frac{2pC_H}{p-2} J(u(t)) + 2\mathrm{e}^{\frac{p-2}{C_H}t}\varphi(0), \quad \forall t \in [0,+\infty). \tag{112}$$

Since $0 \leq J(u(t)) \leq J(u_0)$, it follows from Eq. (112) that

$$\left\| \frac{u(t)}{|x|^{\frac{s}{2}}} \right\|_2^2 \geq 2\mathrm{e}^{\frac{p-2}{C_H}t}\varphi(0). \tag{113}$$

which implies

$$\begin{aligned} \left\| \frac{u(t)}{|x|^{\frac{s}{2}}} \right\|_2 &\geq (2\varphi(0))^{\frac{1}{2}} \mathrm{e}^{\frac{p-2}{2C_H}t} \\ &= \left(\left\| \frac{u_0}{|x|^{\frac{s}{2}}} \right\|_2^2 - \frac{2pC_H}{p-2} J(u_0) \right)^{\frac{1}{2}} \mathrm{e}^{\frac{p-2}{2C_H}t}, \ \forall t \in [0,+\infty), \end{aligned} \tag{114}$$

this contradicts Eq. (106) for sufficiently large t. Thus, $t_* < +\infty$.

Next, we derive the upper bound of t_*. Since the weak solution to problem (1) satisfies the energy equality

$$J(u_0) = J(u(t)) + \int_0^t \left\| \frac{u_\tau(\tau)}{|x|^{\frac{s}{2}}} \right\|_2^2 d\tau. \tag{115}$$

Combining this with Eqs (21), (23), (33) under the conditions $2 < p < q+1$ and $0 \leq J(u_0) < \frac{p-2}{2pC_H} \left\| \frac{u_0}{|x|^{\frac{s}{2}}} \right\|_2^2$, we obtain

$$\begin{aligned} I(u_0) &= pJ(u_0) - \frac{p-2}{2}\|\Delta u_0\|_2^2 - \frac{1}{p}\|\nabla u_0\|_p^p \\ &\quad - \frac{q+1-p}{q+1}\|u_0\|_{q+1}^{q+1} = p\left[J(u_0) - \frac{p-2}{2pC_H} \left\| \frac{u_0}{|x|^{\frac{s}{2}}} \right\|_2^2 \right] \\ &\quad - \frac{p-2}{2}\left[\|\Delta u_0\|_2^2 - \frac{1}{C_H} \left\| \frac{u_0}{|x|^{\frac{s}{2}}} \right\|_2^2 \right] \\ &\quad - \frac{1}{p}\|\nabla u_0\|_p^p - \frac{q+1-p}{q+1}\|u_0\|_{q+1}^{q+1} < 0. \end{aligned} \tag{116}$$

We assert that $I(u(t)) < 0$ for all $t \in [0,t_*)$. Otherwise, there exists a $\tilde{t} \in (0,t_*)$ such that $I(u(\tilde{t})) = 0$, and $I(u(t)) < 0$ for all $t \in [0,\tilde{t})$. Combining with Eq. (95), we have $S'(t) = -I(u(t)) > 0$ for all $t \in [0,\tilde{t})$. It means that $S(t)$ is strictly increasing on $[0,\tilde{t})$, and consequently,

$$0 \leq J(u_0) < \frac{p-2}{2pC_H} \left\| \frac{u_0}{|x|^{\frac{s}{2}}} \right\|_2^2 < \frac{p-2}{2pC_H} \left\| \frac{u(\tilde{t})}{|x|^{\frac{s}{2}}} \right\|_2^2. \tag{117}$$

Furthermore, from Eqs (21) and (33), we derive

$$\begin{aligned} J(u_0) \geq J(u(\tilde{t})) &= \frac{p-2}{2p}\|\Delta u(\tilde{t})\|_2^2 + \frac{1}{p^2}\|\nabla u(\tilde{t})\|_p^p \\ &\quad + \frac{q+1-p}{q+1}\|u(\tilde{t})\|_{q+1}^{q+1} + \frac{1}{p}I(u(\tilde{t})) \\ &\geq \frac{p-2}{2p}\|\Delta u(\tilde{t})\|_2^2 \geq \frac{p-2}{2pC_H} \left\| \frac{u(\tilde{t})}{|x|^{\frac{s}{2}}} \right\|_2^2, \end{aligned} \tag{118}$$

which contradicts Eq. (117). Therefore, $I(u(t)) < 0$ for all $t \in [0,t_*)$, and consequently $S'(t) = -I(u(t)) > 0$ for all $t \in [0,t_*)$. This implies that $S(t)$ is strictly increasing on $[0,t_*)$.

In order to derive the upper bound of t_*, we define a function

$$\Phi(t) := \int_0^t \left\| \frac{u(\tau)}{|x|^{\frac{s}{2}}} \right\|_2^2 d\tau + (\hat{T}-t) \left\| \frac{u_0}{|x|^{\frac{s}{2}}} \right\|_2^2 + \sigma(t+\kappa)^2, \quad \forall t \in \left[0,\hat{T}\right], \tag{119}$$

where $\hat{T} \in (0,t_*)$, $\sigma > 0$ and $\kappa > 0$ are sufficiently small. From Eq. (119), we obtain

$$\begin{aligned}\Phi'(t)=&\left\|\frac{u(t)}{|x|^{\frac{s}{2}}}\right\|_2^2-\left\|\frac{u_0}{|x|^{\frac{s}{2}}}\right\|_2^2+2\sigma(t+\kappa)\\=&\int_0^t\frac{d}{d\tau}\left\|\frac{u(\tau)}{|x|^{\frac{s}{2}}}\right\|_2^2d\tau+2\sigma(t+\kappa)\\=&2\int_0^t\int_\Omega\frac{u(\tau)u_\tau(\tau)}{|x|^s}dxd\tau+2\sigma(t+\kappa).\end{aligned}\tag{120}$$

It is evident from Eqs (119) and (120) that

$$\Phi(0)=\hat{T}\left\|\frac{u_0}{|x|^{\frac{s}{2}}}\right\|_2^2+\sigma\kappa^2>0,\quad \Phi'(0)=2\sigma\kappa>0.\tag{121}$$

By Eqs (21), (33) and (119), combined with $2<p<q+1$ and $\sigma>0$, we derive

$$\begin{aligned}\Phi''(t)=&2\int_\Omega\frac{u(t)u_t(t)}{|x|^s}dx+2\sigma\\=&-2I(u(t))+2\sigma\\=&-2pJ(u(t))+(p-2)\|\Delta u(t)\|_2^2\\&+\frac{2}{p}\|\nabla u(t)\|_p^p+\frac{2(q+1-p)}{q+1}\|u(t)\|_{q+1}^{q+1}+2\sigma\\=&-2pJ(u_0)+2p\int_0^t\left\|\frac{u_\tau(\tau)}{|x|^{\frac{s}{2}}}\right\|_2^2d\tau\\&+(p-2)\|\Delta u(t)\|_2^2+\frac{2}{p}\|\nabla u(t)\|_p^p\\&+\frac{2(q+1-p)}{q+1}\|u(t)\|_{q+1}^{q+1}+2\sigma\\\geq&-2pJ(u_0)+2p\int_0^t\left\|\frac{u_\tau(\tau)}{|x|^{\frac{s}{2}}}\right\|_2^2d\tau\\&+\frac{p-2}{C_H}\left\|\frac{u(t)}{|x|^{\frac{s}{2}}}\right\|_2^2,\forall t\in[0,\hat{T}].\end{aligned}\tag{122}$$

Recalling $S(t)$ is strictly increasing on $[0,t_*)$, we know $\Phi'(t)>0$, which implies $\Phi(t)$ is strictly increasing on $[0,t_*)$. Through a direct calculation, we obtain

$$\begin{aligned}&-\frac{p}{2}[\Phi'(t)]^2=-2p\left[\int_0^t\int_\Omega\frac{u(\tau)u_\tau(\tau)}{|x|^s}dxd\tau+\sigma(t+\kappa)\right]^2\\\geq&-2p\left[\left(\int_0^t\left\|\frac{u(\tau)}{|x|^{\frac{s}{2}}}\right\|_2^2d\tau\right)^{\frac{1}{2}}\left(\int_0^t\left\|\frac{u_\tau(\tau)}{|x|^{\frac{s}{2}}}\right\|_2^2d\tau\right)^{\frac{1}{2}}\right.\\&\left.+\sigma(t+\kappa)\right]^2\\\geq&-2p\left[\int_0^t\left\|\frac{u(\tau)}{|x|^{\frac{s}{2}}}\right\|_2^2d\tau+\sigma(t+\kappa)^2\right]\left[\int_0^t\left\|\frac{u_\tau(\tau)}{|x|^{\frac{s}{2}}}\right\|_2^2d\tau+\sigma\right]\\\geq&-2p\Phi(t)\left[\int_0^t\left\|\frac{u_\tau(\tau)}{|x|^{\frac{s}{2}}}\right\|_2^2d\tau+\sigma\right].\end{aligned}\tag{123}$$

Then, it follows from Eqs (119)-(123) that

$$\begin{aligned}&\Phi(t)\Phi''(t)-\frac{p}{2}(\Phi'(t))^2\\\geq&\Phi(t)\left[-2pJ(u_0)+2p\int_0^t\left\|\frac{u_\tau(\tau)}{|x|^{\frac{s}{2}}}\right\|_2^2d\tau\right.\\&\left.+\frac{p-2}{C_H}\left\|\frac{u(t)}{|x|^{\frac{s}{2}}}\right\|_2^2\right]-2p\Phi(t)\left[\int_0^t\left\|\frac{u_\tau(\tau)}{|x|^{\frac{s}{2}}}\right\|_2^2d\tau+\sigma\right]\\=&2p\Phi(t)\left[\left(\frac{p-2}{2pC_H}\left\|\frac{u_0}{|x|^{\frac{s}{2}}}\right\|_2^2-J(u_0)\right)-\sigma\right]\geq0,\end{aligned}\tag{124}$$

where $\sigma\in\left(0,\frac{p-2}{2pC_H}\left\|\frac{u_0}{|x|^{\frac{s}{2}}}\right\|_2^2-J(u_0)\right]$. Let $\Gamma(t)=\Phi^{-\frac{p}{2}+1}(t)$ for any $t\in[0,\hat{T}]$. By a direct calculation, we obtain

$$\Gamma'(t)=\left(-\frac{p}{2}+1\right)\Phi^{-\frac{p}{2}}(t)\Phi'(t),\tag{125}$$

$$\begin{aligned}\Gamma''(t)=&\left(-\frac{p}{2}+1\right)\Phi^{-\frac{p}{2}-1}(t)\\&\times\left[\Phi(t)\Phi''(t)-\frac{p}{2}(\Phi'(t))^2\right].\end{aligned}\tag{126}$$

By Eqs (124), (126) and the condition $p>2$, we have $\Gamma''(t)\leq0$, which implies that $\Gamma(t)$ is a concave function on $[0,\hat{T}]$, and $\Gamma'(t)$ is a decreasing function on $[0,\hat{T}]$. Therefore,

$$\Gamma(\hat{T})\leq\Gamma(0),\quad\forall t\in[0,\hat{T}].\tag{127}$$

By integrating the above inequality over $\left[0,\hat{T}\right]$, we obtain

$$\Gamma\left(\hat{T}\right) \leq \Gamma(0) + \Gamma'(0)\hat{T}. \tag{128}$$

Since $\Phi(0) > 0$ and $\Phi(t)$ is strictly increasing on $\left[0,\hat{T}\right]$, it follows that

$$\Gamma(0) = \Phi^{-\frac{p}{2}+1}(0) > 0, \tag{129}$$

$$\Gamma\left(\hat{T}\right) = \Phi^{-\frac{p}{2}+1}\left(\hat{T}\right) > 0, \tag{130}$$

for any $\hat{T} \in (0,t_*)$. Additionally, by the conditions $\Phi'(0) > 0$, $p > 2$ and using Eq. (125), we have

$$\begin{aligned}\Gamma'(0) &= \left(-\frac{p}{2}+1\right)\Phi^{-\frac{p}{2}}(0)\Phi'(0)\\ &= \left(-\frac{p}{2}+1\right)\Gamma(0)\frac{\Phi'(0)}{\Phi(0)} < 0.\end{aligned} \tag{131}$$

From Eqs(128)-(131), combined with Eqs (119) and (120), we derive

$$\begin{aligned}\hat{T} &\leq \frac{\Gamma(0)-\Gamma\left(\hat{T}\right)}{-\Gamma'(0)} \leq \frac{\Gamma(0)}{-\Gamma'(0)} = \frac{2\Phi(0)}{(p-2)\Phi'(0)}\\ &= \frac{\hat{T}\left\|\frac{u_0}{|x|^{\frac{s}{2}}}\right\|_2^2 + \sigma\kappa^2}{(p-2)\sigma\kappa} = \frac{\left\|\frac{u_0}{|x|^{\frac{s}{2}}}\right\|_2^2}{(p-2)\sigma\kappa}\hat{T} + \frac{\kappa}{p-2},\end{aligned} \tag{132}$$

where $\kappa \in \left(\frac{\left\|\frac{u_0}{|x|^{\frac{s}{2}}}\right\|_2^2}{(p-2)\sigma}, +\infty\right)$. Taking the limit as $\hat{T} \to t_*$ in Eq. (132), we have

$$t_* \leq \frac{\sigma\kappa^2}{(p-2)\sigma\kappa - \left\|\frac{u_0}{|x|^{\frac{s}{2}}}\right\|_2^2}. \tag{133}$$

We define the set

$$\begin{aligned}M := \Big\{(\sigma,\kappa) : \sigma \in \Big(0, \frac{p-2}{2pC_H}\left\|\frac{u_0}{|x|^{\frac{s}{2}}}\right\|_2^2 - J(u_0)\Big],\\ \kappa \in \Big(\frac{\left\|\frac{u_0}{|x|^{\frac{s}{2}}}\right\|_2^2}{(p-2)\sigma}, +\infty\Big)\Big\},\end{aligned} \tag{134}$$

and the function

$$f(\sigma,\kappa) := \frac{\sigma\kappa^2}{(p-2)\sigma\kappa - \left\|\frac{u_0}{|x|^{\frac{s}{2}}}\right\|_2^2}. \tag{135}$$

Direct calculation shows that $f(\sigma,\kappa)$ attains its minimum value at $\kappa = \frac{2\left\|\frac{u_0}{|x|^{\frac{s}{2}}}\right\|_2^2}{(p-2)\sigma}$. Thus, from Eqs (133)–(135), we derive

$$\begin{aligned}t_* &\leq \inf_{(\sigma,\kappa)\in M} f(\sigma,\kappa)\\ &= \frac{8p\left\|\frac{u_0}{|x|^{s/2}}\right\|_2^2}{(p-2)^2\left[\frac{(p-2)}{C_H}\left\|\frac{u_0}{|x|^{s/2}}\right\|_2^2 - 2pJ(u_0)\right]}.\end{aligned} \tag{136}$$

The proof is completed.

Corollary 1 *Assume $2 < p < q+1$. Then there exists a weak solution with arbitrarily high initial energy to Eq. (1) that blows up in finite time.*

Proof . Let Ω_1 and Ω_2 be two disjoint open subdomains of Ω. Choose an arbitrary nontrivial function $v \in H_N^2(\Omega_1)$, and for any $R > 0$, there exists a sufficiently large $\chi > 0$ such that

$$\begin{aligned}\left\|\frac{\chi v}{|x|^{s/2}}\right\|_2^2 &= \chi^2\int_\Omega \frac{|v|^2}{|x|^s}dx\\ &= \chi^2\int_{\Omega_1}\frac{|v|^2}{|x|^s}dx > \frac{2pC_H}{p-2}R.\end{aligned} \tag{137}$$

and for $2 < p < q+1$ and Eq. (19), it follows that

$$\begin{aligned}R - J(\chi v) &= R - \frac{\chi^2}{2}\|\Delta v\|_2^2 + \frac{\chi^p}{p}\int_\Omega |\nabla v|^p \log|\nabla v|\,dx\\ &\quad + \frac{\chi^p}{p}\log\chi\|\nabla v\|_p^p - \frac{\chi^p}{p^2}\|\nabla v\|_p^p\\ &\quad + \frac{\chi^{q+1}}{q+1}\|v\|_{q+1}^{q+1} \to +\infty,\end{aligned} \tag{138}$$

as $\chi \to +\infty$. Fix χ and $\omega \in H_N^2(\Omega_2)$ such that $J(\chi v) + J(\omega) = R$. Next, we extend v and ω as follows:

$$v=\begin{cases} v,\ x\in\Omega_1,\\ 0,\ x\in\Omega_2,\end{cases}\qquad \omega=\begin{cases}\omega,\ x\in\Omega_2,\\ 0,\ x\in\Omega_1.\end{cases}\tag{139}$$

Let $u_0:=\chi v+\omega$. Then we have

$$\begin{aligned}\left\|\frac{u_0}{|x|^{\frac{s}{2}}}\right\|_2^2&=\int_\Omega\left|\frac{\chi v+\omega}{|x|^s}\right|^2dx\\ &\geq\int_{\Omega_1}\left|\frac{\chi v}{|x|^s}\right|^2dx>\frac{2qC_H}{q-2}R\end{aligned}\tag{140}$$

and

$$\begin{aligned}J(u_0)=&\frac{1}{2}\int_\Omega|\Delta u_0|^2dx-\frac{1}{p}\int_\Omega|\nabla u_0|^p\log|\nabla u_0|\,dx\\ &+\frac{1}{p^2}\int_\Omega|\nabla u_0|^pdx-\frac{1}{q+1}\int_\Omega|u_0|^{q+1}dx\\ =&\frac{1}{2}\int_{\Omega_1}|\chi\Delta v|^2dx-\frac{1}{p}\int_{\Omega_1}|\chi\nabla v|^p\log|\chi\nabla v|\,dx\\ &+\frac{1}{p^2}\int_{\Omega_1}|\chi\nabla v|^pdx-\frac{1}{q+1}\int_{\Omega_1}|\chi v|^{q+1}dx\\ &+\frac{1}{2}\int_{\Omega_2}|\Delta\omega|^2dx-\frac{1}{p}\int_{\Omega_2}|\nabla\omega|^p\log|\nabla\omega|\,dx\\ &+\frac{1}{p^2}\int_{\Omega_2}|\nabla\omega|^pdx-\frac{1}{q+1}\int_{\Omega_2}|\omega|^{q+1}dx\\ =&J(\chi v)+J(\omega)\\ =&R,\end{aligned}\tag{141}$$

which means $J(u_0)=R<\frac{p-2}{2pC_H}\left\|\frac{u_0}{|x|^{\frac{s}{2}}}\right\|_2^2$. Therefore, by Theorem 3, we conclude that there exists a weak solution with arbitrarily high initial energy to Eq. (1) that blows up in finite time.

The proof is completed.

5 Non-extinction and extinction in finite time

In this section, by employing energy estimates and specific ordinary differential inequalities, we characterize both non-extinction and extinction phenomena of solutions in finite time, and rigorously quantify their corresponding extinction rates.

Theorem 4 *Assume that $p\geq 2$ and $p>q+1$. If $J(u_0)<0$, then the solution to Eq. (1) does not extinct in finite time.*

Proof . Since the weak solution to Eq. (1) satisfies the following energy inequality:

$$J(u_0)=J(u)+\int_0^t\left\|\frac{u_\tau(\tau)}{|x|^{\frac{s}{2}}}\right\|_2^2d\tau.\tag{142}$$

Furthermore, from the definition of $S(t)$ and using Eqs (20), (21), (23) and (33) under the conditions $|x|<L$, $p\geq 2$ and $p>q+1$, we derive

$$\begin{aligned}S'(t)=&-pJ(u(t))+\frac{p-2}{2}\|\Delta u(t)\|_2^2\\ &+\frac{1}{p}\|\nabla u(t)\|_p^p+\frac{q+1-p}{q+1}\|u(t)\|_{q+1}^{q+1}\\ =&-pJ(u_0)+p\int_0^t\left\|\frac{u_\tau(\tau)}{|x|^{\frac{s}{2}}}\right\|_2^2d\tau+\frac{p-2}{2}\|\Delta u(t)\|_2^2\\ &+\frac{1}{p}\|\nabla u(t)\|_p^p-\frac{p-q-1}{q+1}\|u(t)\|_{q+1}^{q+1}\\ \geq&-pJ(u_0)+p\int_0^t\left\|\frac{u_\tau(\tau)}{|x|^{\frac{s}{2}}}\right\|_2^2d\tau\\ &-\frac{p-q-1}{q+1}\|u(t)\|_{q+1}^{q+1}\\ \geq&-pJ(u_0)-\frac{p-q-1}{q+1}|\Omega|^{\frac{1-q}{2}}\left(\int_\Omega u^2(t)\,dx\right)^{\frac{q+1}{2}}\\ \geq&-pJ(u_0)-\frac{p-q-1}{q+1}|\Omega|^{\frac{1-q}{2}}(2L^s)^{\frac{q+1}{2}}S^{\frac{q+1}{2}}(t),\end{aligned}\tag{143}$$

which implies

$$\begin{aligned}&S'(t)+\frac{p-q-1}{q+1}|\Omega|^{\frac{1-q}{2}}(2L^s)^{\frac{q+1}{2}}S^{\frac{q+1}{2}}(t)\\ &\qquad\geq-pJ(u_0).\end{aligned}\tag{144}$$

Since $p\geq 2$, $p>q+1$ and $J(u_0)<0$, we have

$$\alpha_1=\frac{p-q-1}{q+1}|\Omega|^{\frac{1-q}{2}}(2L^s)^{\frac{q+1}{2}}>0.\tag{145}$$

Then, it follows from Eqs (144) and (145) that

$$S'(t)+\alpha_1S^{\frac{q+1}{2}}(t)\geq\beta_1.\tag{146}$$

By Lemma 4, we know

$$S(t)\geq\min\left\{S(0),\left(\frac{\beta_1}{\alpha_1}\right)^{\frac{2}{q+1}}\right\}>0,\ \forall t\in(0,+\infty).\tag{147}$$

Hence, Eq. (147) implies

$$\left\|\frac{u(t)}{|x|^{\frac{s}{2}}}\right\|_2=\sqrt{2S(t)}>0,\quad\forall t\in(0,+\infty).\tag{148}$$

Then, for any $m_3 > 1$, by the interpolation inequality, we obtain

$$\left\| \frac{u(t)}{|x|^{\frac{s}{2}}} \right\|_2 \le \left\| \frac{u(t)}{|x|^{\frac{s}{2}}} \right\|_{m_3}^{\frac{1}{2}} \left\| \frac{u(t)}{|x|^{\frac{s}{2}}} \right\|_{\frac{m_3}{m_3-1}}^{\frac{1}{2}}. \tag{149}$$

which together with $\left\| \frac{u(t)}{|x|^{\frac{s}{2}}} \right\|_2 > 0$, implies that for any $m_3 > 1$, there does not exist a $t_* > 0$ such that

$$\lim_{t\to t_*} \left\| \frac{u(t)}{|x|^{\frac{s}{2}}} \right\|_{m_3} = 0 \quad \text{or} \quad \lim_{t\to t_*} \left\| \frac{u(t)}{|x|^{\frac{s}{2}}} \right\|_{\frac{m_3}{m_3-1}} = 0. \tag{150}$$

Therefore, the solution to Eq. (1) does not become extinct in finite time.

The proof is completed.

Theorem 5 *Assume that* $p < 2$ *and* $q < 1$. *If* $[\mathrm{e}(2-p)]^{-1} B^2 < 1$ *and*

$$\left\| \frac{u_0}{|x|^{\frac{s}{2}}} \right\|_2 > \left(\frac{D_2}{D_1} \right)^{\frac{1}{1-q}}. \tag{151}$$

then the solution to Eq. (1) *becomes extinct in finite time, with the upper bound of the extinction rate is*

$$\begin{cases} \left\| \frac{u(t)}{|x|^{\frac{s}{2}}} \right\|_2 \le \left[\left\| \frac{u_0}{|x|^{\frac{s}{2}}} \right\|_2^{1-q} \right. \\ \quad \left. + \frac{1}{2} \left(D_2 - D_1 \left\| \frac{u_0}{|x|^{\frac{s}{2}}} \right\|_2^{1-q} \right) t \right]^{\frac{1}{1-q}}, \ 0 < t < T_0, \\ \left\| \frac{u(t)}{|x|^{\frac{s}{2}}} \right\|_2 = 0, \qquad t \ge T_0. \end{cases} \tag{152}$$

where

$$T_0 = \frac{2 \left\| \frac{u_0}{|x|^{\frac{s}{2}}} \right\|_2^{1-q}}{D_1 \left\| \frac{u_0}{|x|^{\frac{s}{2}}} \right\|_2^{1-q} - D_2}, \tag{153}$$

$$D_1 = (1-q) \left\{ 1 - [\mathrm{e}(2-p)]^{-1} B^2 \right\} C_H^{-1} \tag{154}$$

$$D_2 = (1-q) |\Omega|^{\frac{1-q}{2}} L^{\frac{s(q+1)}{2}} \tag{155}$$

and B *is the optimal embedding constant of* $H_0^2(\Omega) \hookrightarrow W_0^{1,2}(\Omega)$.

Proof . Multiplying Eq. (1) by u and integrating over Ω, we obtain

$$\frac{1}{2} \frac{d}{dt} \left\| \frac{u(t)}{|x|^{\frac{s}{2}}} \right\|_2^2 + \|\Delta u(t)\|_2^2 - \int_\Omega |\nabla u(t)|^p \log |\nabla u(t)| \, dx = \int_\Omega |u(t)|^q u(t) \, dx. \tag{156}$$

For the left-hand side of Eq. (156), we observe from Lemma 1 and Eq. (32) that there exists a positive constant $\rho_3 = 2 - p$ such that

$$\begin{aligned} &S'(t) + \|\Delta u(t)\|_2^2 - \int_\Omega |\nabla u(t)|^p \log |\nabla u(t)| \, dx \\ &\ge S'(t) + \|\Delta u(t)\|_2^2 - (\mathrm{e}\rho_3)^{-1} \|\nabla u(t)\|_{p+\rho_3}^{p+\rho_3} \\ &= S'(t) + \|\Delta u(t)\|_2^2 - [\mathrm{e}(2-p)]^{-1} \|\nabla u(t)\|_2^2 \\ &\ge S'(t) + \|\Delta u(t)\|_2^2 - [\mathrm{e}(2-p)]^{-1} B^2 \|\Delta u(t)\|_2^2 \\ &\ge S'(t) + \left\{ 1 - [\mathrm{e}(2-p)]^{-1} B^2 \right\} C_H^{-1} \left\| \frac{u(t)}{|x|^{\frac{s}{2}}} \right\|_2^2 \\ &= S'(t) + 2 \left\{ 1 - [\mathrm{e}(2-p)]^{-1} B^2 \right\} C_H^{-1} S(t). \end{aligned} \tag{157}$$

Then, Eq. (105) can be represented as

$$\begin{aligned} &S'(t) + 2 \left\{ 1 - [\mathrm{e}(2-p)]^{-1} B^2 \right\} C_H^{-1} S(t) \le \int_\Omega |u(t)|^{q+1} dx \\ &\le |\Omega|^{\frac{1-q}{2}} \|u(t)\|_2^{q+1} \\ &\le 2^{\frac{q+1}{2}} |\Omega|^{\frac{1-q}{2}} L^{\frac{s(q+1)}{2}} S^{\frac{q+1}{2}}(t). \end{aligned} \tag{158}$$

Setting $H(t) = S^{\frac{1-q}{2}}(t)$, we obtain from the above that

$$\begin{aligned} H'(t) &= \frac{1-q}{2} S^{\frac{-1-q}{2}}(t) S'(t) \\ &\le (1-q) 2^{\frac{q-1}{2}} |\Omega|^{\frac{1-q}{2}} L^{\frac{s(q+1)}{2}} \\ &\quad - (1-q) \left\{ 1 - [\mathrm{e}(2-p)]^{-1} B^2 \right\} C_H^{-1} S^{\frac{1-q}{2}}(t) \\ &= 2^{\frac{q-1}{2}} D_2 - D_1 H(t) = \Lambda(t). \end{aligned} \tag{159}$$

Since $\left\| \frac{u_0}{|x|^{\frac{s}{2}}} \right\|_2 > \left(D_2 D_1^{-1} \right)^{\frac{1}{1-q}}$, we have $\Lambda(0) < 0$. Then there exists a sufficiently small $\tilde{t} > 0$ such that $\Lambda(t) < \frac{\Lambda(0)}{2} < 0$ for all $t \in (0, \tilde{t}]$. This implies that

$$H'(t) \le \frac{\Lambda(0)}{2}. \tag{160}$$

Integrating Eq. (160) over $(0,t)$, we obtain

$$\begin{cases} H(t) \le H(0) + \dfrac{\Lambda(0)}{2}t, & 0 < t < T_0, \\ H(t) = 0, & t \ge T_0. \end{cases} \tag{161}$$

From the definitions of $H(t)$ and $\Lambda(t)$, we conclude that Eq. (152) holds.

The proof is completed.

Theorem 6 *Assume that $s = 0$, $p = 2$ and $q < 1$. If $J(u_0) \le 0$ and $\|u_0\|_2 < \left(D_4 D_3^{-1}\right)^{\frac{1}{1-q}}$, then the solution to Eq. (1) becomes extinct in finite time, where the lower bound of the extinction rate is*

$$\begin{cases} \|u(t)\|_2 \ge \left[D_4 D_3^{-1} + \left(\|u_0\|_2^{1-q} \right.\right. \\ \quad \left.\left. - D_4 D_3^{-1}\right) \mathrm{e}^{D_3 t}\right]^{\frac{1}{1-q}}, \quad 0 < t < T_1, \\ \|u(t)\|_2 = 0, \quad t \ge T_1. \end{cases} \tag{162}$$

where

$$T_1 = \frac{1}{D_3} \log \left(\frac{D_4 D_3^{-1}}{D_4 D_3^{-1} - \|u_0\|_2^{1-q}} \right) \tag{163}$$

$D_3 = \frac{1-q}{2} B_1^{-2}$, $D_4 = \frac{(q-1)^2}{q+1} |\Omega|^{\frac{1-q}{2}}$, and B_1 is the optimal embedding constant of $W_0^{1,2}(\Omega) \hookrightarrow L^2(\Omega)$.

Proof . We define

$$G(t) := \tfrac{1}{2}\|u(t)\|_2^2 \tag{164}$$

Combined with the conditions $s = 0$, $p = 2$ and $q < 1$, and based on the energy equality

$$J(u_0) = J\big(u(t)\big) + \int_0^t \|u_\tau(\tau)\|_2^2 d\tau \tag{165}$$

we derive from Eqs (20), (21), (23) and $J(u_0) \le 0$ that

$$\begin{aligned} G'(t) &= \int_\Omega u(t) u_t(t) dx \\ &= -I(u(t)) \\ &= -2J(u(t)) + \frac{1}{2}\|\nabla u(t)\|_2^2 + \frac{q-1}{q+1}\|u(t)\|_{q+1}^{q+1} \\ &\ge -2J(u_0) + \frac{B_1^{-2}}{2}\|u(t)\|_2^2 \\ &+ \frac{q-1}{q+1}|\Omega|^{\frac{1-q}{2}}\|u(t)\|_2^{q+1} \\ &\ge B_1^{-2} G(t) + 2^{\frac{q+1}{2}} \frac{q-1}{q+1} |\Omega|^{\frac{1-q}{2}} G^{\frac{q+1}{2}}(t). \end{aligned} \tag{166}$$

Setting $Z(t) = G^{\frac{1-q}{2}}(t)$, we obtain from Eq. (166) that

$$\begin{aligned} Z'(t) &\ge \frac{1-q}{2} G^{-\frac{q+1}{2}}(t) \\ &\times \left[B_1^{-2} G(t) + 2^{\frac{q+1}{2}} \frac{q-1}{q+1} |\Omega|^{\frac{1-q}{2}} G^{\frac{q+1}{2}}(t) \right] \\ &= \frac{1-q}{2} B_1^{-2} G^{\frac{1-q}{2}}(t) - 2^{\frac{q-1}{2}} \frac{(q-1)^2}{q+1} |\Omega|^{\frac{1-q}{2}} \\ &= D_3 Z(t) - 2^{\frac{q-1}{2}} D_4. \end{aligned} \tag{167}$$

Solving this ordinary differential equation yields

$$\begin{cases} Z(t) \ge 2^{\frac{q-1}{2}} D_4 D_3^{-1} + \left(Z(0) - 2^{\frac{q-1}{2}} D_4 D_3^{-1} \right) e^{D_3 t}, \\ \qquad\qquad 0 < t < T_1, \\ Z(t) = 0, \quad t \ge T_1, \end{cases} \tag{168}$$

which implies that Eq. (162) holds.

The proof is completed.

Theorem 7 *Assume that $q + 1 < 2 < p$. If $J(u_0) \le 0$ and*

$$\left\| \frac{u_0}{|x|^{\frac{s}{2}}} \right\|_2 < \left(\frac{D_6}{D_5} \right)^{\frac{1}{1-q}}. \tag{169}$$

then the solution to Eq. (1) becomes extinct in finite time, and the lower bound of the extinction rate is

$$\begin{cases} \left\| \frac{u(t)}{|x|^{\frac{s}{2}}} \right\|_2 \ge \left[D_6 D_5^{-1} + \left(\left\| \frac{u_0}{|x|^{\frac{s}{2}}} \right\|_2^{1-q} - D_6 D_5^{-1} \right) \mathrm{e}^{D_5 t} \right]^{\frac{1}{1-q}}, \\ \qquad\qquad 0 < t < T_2, \\ \left\| \frac{u(t)}{|x|^{\frac{s}{2}}} \right\|_2 = 0, \qquad t \ge T_2, \end{cases} \tag{170}$$

where

$$T_2 = \frac{1}{D_5}\log\left(\frac{D_6 D_5^{-1}}{D_6 D_5^{-1} - \left\|\frac{u_0}{|x|^{s/2}}\right\|_2^{1-q}}\right), \tag{171}$$

$$D_5 = \frac{(1-q)(p-2)}{2C_H}, \tag{172}$$

$$D_6 = (1-q)L^{\frac{s(q+1)}{2}}|\Omega|^{\frac{1-q}{2}}\cdot\frac{p-q-1}{q+1}. \tag{173}$$

Proof . By a direct calculation, similar to Eq. (166), we obtain

$$\begin{aligned}
S'(t) =& -I(u(t))\\
=& -pJ(u(t)) + \frac{p-2}{2}\|\Delta u(t)\|_2^2\\
&+\frac{1}{p}\|\nabla u(t)\|_p^p + \frac{q+1-p}{q+1}\|u(t)\|_{q+1}^{q+1}\\
\geq& -pJ(u_0) + \frac{p-2}{2}\|\Delta u(t)\|_2^2 + \frac{1}{p}\|\nabla u(t)\|_p^p\\
&-\frac{p-q-1}{q+1}\|u(t)\|_{q+1}^{q+1}\\
\geq& \frac{p-2}{2}\|\Delta u(t)\|_2^2 - \frac{p-q-1}{q+1}\|u(t)\|_{q+1}^{q+1}.
\end{aligned} \tag{174}$$

Then, by Eqs (33), (174) and $|x| \leq L$, we derive

$$\begin{aligned}
S'(t) \geq& \frac{p-2}{2}C_H^{-1}\left\|\frac{u(t)}{|x|^{\frac{s}{2}}}\right\|_2^2\\
&-|\Omega|^{\frac{1-q}{2}}\frac{p-q-1}{q+1}\left(\int_\Omega u^2(t)dx\right)^{\frac{q+1}{2}}\\
\geq& (p-2)C_H^{-1}S(t)\\
&-L^{\frac{s(q+1)}{2}}|\Omega|^{\frac{1-q}{2}}\frac{p-q-1}{q+1}\left(\int_\Omega \frac{u^2(t)}{|x|^s}dx\right)^{\frac{q+1}{2}}\\
=& (p-2)C_H^{-1}S(t)\\
&-2^{\frac{q+1}{2}}L^{\frac{s(q+1)}{2}}|\Omega|^{\frac{1-q}{2}}\frac{p-q-1}{q+1}S^{\frac{q+1}{2}}(t)
\end{aligned} \tag{175}$$

According to Eq. (175) and $H(t) = S^{\frac{1-q}{2}}(t)$,

$$\begin{aligned}
H'(t) \geq& \frac{1-q}{2}S^{-\frac{q+1}{2}}(t)\left((p-2)C_H^{-1}S(t)\right.\\
&\left.-2^{\frac{q+1}{2}}L^{\frac{s(q+1)}{2}}|\Omega|^{\frac{1-q}{2}}\frac{p-q-1}{q+1}S^{\frac{q+1}{2}}(t)\right)\\
=& D_5 H(t) - 2^{\frac{q-1}{2}}D_6.
\end{aligned} \tag{176}$$

This ordinary differential equation directly implies that

$$\begin{cases}
H(t) \geq 2^{\frac{q-1}{2}}D_6 D_5^{-1}\\
\qquad + \left(H(0) - 2^{\frac{q-1}{2}}D_6 D_5^{-1}\right)e^{D_5 t},\ 0 < t < T_2,\\
H(t) = 0, \qquad\qquad t \geq T_2.
\end{cases} \tag{177}$$

Then, we obtain Eq. (170).

The proof is completed.

Declaration of competing interest

The authors declare that they have no known competing financial interests or personal relationships that could have appeared to influence the work reported in this paper.

Acknowledgements This work is sponsored by the National Natural Science Foundation of China (Grant No.12261053), the project Science and Technology Project of Yunnan Province, Key Technology Projects in Yunnan Province (No. 202302AF080003), the Special Basic Cooperative Research Programs of Yunnan Provincial Undergraduate Universities Association (Grant No.202401BA070001-110, 202301
BA070001-002, 202101BA070001-132), and the Scientific Research Fund of Education Department of Yunnan Province (Grant No.2024Y775, 2024Y776, 2025Y1076, 2024J0775).

References

1. M. D. Johnson, C. Orme, A. W. Hunt, D. Graff, J. Sudijono, L. M. Sander, B. G. Orr, *Phys. Rev. Lett.* **72**, (1994)
2. M. Ortiz, E. A. Repetto, H. Si, *J. Mech. Phys. Solids.* **47**, (1999)
3. T. P. Schulze, R. V. Kohn, *Phys. D.* **132**, (1999)
4. A. Zangwill, *J. Cryst. Growth.* **163**, (1996)
5. B. B. King, O. Stein, M. Winkler, *J. Math. Anal. Appl.* **286**, (2003)
6. M. Winkler, *Z. Angew. Math. Phys.* **62**, (2011)
7. A. N. Sandjo, S. Moutari, Y. Gningue, *J. Differential Equations.* **259**, (2015)
8. H. Fujita, T. Kato, *Arch. Ration. Mech. Anal.* **516**, (1964)
9. T. Kato, *Math. Z.* **187**, (1984)

10. T. Kato, Bol. Soc. Bras. Mat. (N.S.). **22**, (1992)
11. A. El Soufi, M. Jazar, R. Monneau, *Ann. Inst. H. Poincare Anal. Non Lineaire.* **24**, (2007)
12. F. L. Sun, L. S. Liu, Y. H. Wu, *J. Math. Anal. Appl.* **458**, (2018)
13. G. Xu, J. Zhou , C. Mu, *J. Dyn. Control Syst.* **26**, (2020)
14. J. Zhou, *J. Math. Anal. Appl.* **464**, (2018)
15. J. Zhou, *Nonlinear Anal. Real World Appl.* **48**, (2019)
16. Y. Feng, B. Y. Hu, X. Q. Xu, *J. Differential Equations.* **317**, (2022)
17. K. Baghaei, *Comptes Rendus. Mecanique.* **350**, (2022)
18. Z. H. Dong, J. Zhou, *Z. Angew. Math. Phys.* **68**, (2017)
19. C. Qu, X. Bai, S. Zheng, *J. Math. Anal. Appl.* **412**, (2014)
20. B. Guo, W. Gao, *J. Math. Anal. Appl.* **422**, (2015)
21. B. Guo, J. J. Zhang, W. J. Gao, M. L. Liao, *J. Differential Equations.* **340**, (2022)
22. Y. Z. Han, *Nonlinear Anal. Real World Appl.* **43**, (2018)
23. K. Ishige, N. Miyake, S. Okabe, *SIAM J. Math. Anal.* **52**, (2020)
24. Q. W. Li, W. J. Gao, Y. Z. Han, *Nonlinear Anal.* **147**, (2016)
25. J. Lv, Z. B. Fang, *Discrete Contin. Dyn. Syst.-S.* **17**, (2024)
26. R. Kiwan, M. Jazar, *Ann. Inst. H. Poincare Anal. Non Lineaire.* **25**, (2008)
27. A. Khelghati, K. Baghaei, *Math. Methods Appl. Sci.* **44**, (2021)
28. M. L. Liao, Q. W. Li, *Taiwanese J. Math.* **24**, (2020)
29. Y. Liu, W. K. Li, *Discrete Contin. Dyn.-S.* **14**, (2021)
30. C. C. Liu, Y. T. Ma, H. Tang, *Appl. Math. Lett.* **111**, (2021)
31. B. C. Liu, K. Li, F. J. Li, *J. Math. Phys.* **64**, (2023)
32. J. Lv, Z. B. Fang, *Nonlinear Anal. Real World Appl.* **81**, (2025)
33. S. Jayachandran, G. Soundararajan, *Math. Methods Appl. Sci.* **47**, (2024)
34. M. Zhang, Z. Liu, X. Zhang, *Math. Nachr.* **297**, (2024)
35. Z. Q. Wu, J. N. Zhao, J. X. Yin, H. L. Li, *Nonlinear diffusion equations.* (World Scientific, 2001)
36. M. Feng, J. Zhou, *J. Math. Anal. Appl.* **464**, (2018)
37. Z. Tan, *Acta Math. Sci.* **24**, (2004)
38. G.Y. Xu, J. Zhou, *Commun. Pure Appl. Anal.* **17**, (2018)
39. Y. Z. Han, X. Liu, *Rocky Mountain J. Math.* **51**, (2021)
40. Z. Liu, Z. B. Fang, *Nonlinear Anal. Real World Appl.* **70**, (2023)
41. H. Liu, Z. B. Fang, *Math. Methods Appl. Sci.* **47**, (2024)
42. H. Song, *Nonlinear Anal. Real World Appl.* **26**, (2015)
43. G. A. Philippin, S. Vernier Piro, *J. Math. Anal. Appl.* **436**, (2016)
44. A. Hao, J. Zhou, *Appl. Math. Lett.* **64**, (2017)
45. H. A. Levine, *Arch. Ration. Mech. Anal.* **51**, (1973)
46. X. Mao, C. Yuan, *Stochastic differential equations with Markovian switching*. (Imperial College Press, London, 2006).
47. M. Badiale, G. Tarantello, *Arch. Ration. Mech. Anal.* **163**, (2002)

TTMP vol 2 (2), 2025
doi: 10.30511/TTMP.2025.2059119.1053

Transactions in Theoretical and Mathematical Physics

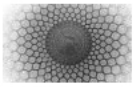

Effect of time reversal symmetry on the current-phase relation in Josephson junctions including two-gap superconductors

Masoumeh Avarideh[a], **Reza Afzali**[b]

[1]Department of Physics, K. N. Toosi University of Technology, Tehran 15875-4416, Iran

Received: 30 April 2025 / Accepted: 31 May 2025 / Published: 31 May 2025

Abstract From a general viewpoint, the Josephson Effect is a quantum phenomenon that the tunnelling of Cooper electron pairs can describe. This junction involves two or more superconductors separated by a thin layer of non-superconducting material. A supercurrent can flow without dissipation through this junction without applying voltage. The dependence of the Josephson current on the phase difference between the two superconductors is of significant importance and is investigated in this study. This research considers a Josephson junction consisting of two gap superconductors separated by a thin insulator. Additionally, we consider a spin-singlet s-wave pair potential in each conduction band. We study the effect of time-reversal symmetry on the phase difference and, consequently, on the Josephson current in two cases. The first case is when only one of the superconductors has time-reversal symmetry, and the second is when neither superconductor has time-reversal symmetry. These states are compared with the condition where both superconductors have time-reversal symmetry.

1 Introduction

In 1962, Josephson predicted that a supercurrent could exist in a junction consisting of two superconductors separated by a thin insulator (typically about 1 nm) [1]. This phenomenon was experimentally confirmed by Shapiro [3–5]. Research on Josephson junctions remains essential due to their wide applications, including SQUIDs, electrical metrology, and digital memory circuits [4, 6, 7]. The initial structure of the Josephson junction was the Superconductor-Insulator-Superconductor (SIS) junction. Over the decades, alternative structures such as Superconductor-Ferromagnetic-Superconductor (SFS) [6–9] and Superconductor-Insulator-Ferromagnetic-Superconductor (SIFS) [6–10] have been investigated. Various aspects of Josephson junctions have been studied, including their current-voltage (I-V) characteristics, temperature dependence [11], frequency dependence [12], electrodynamics, and the Current-Phase Relation (CPR) [2]. Some studies on Josephson junctions' current-voltage (I-V) characteristics have shown that the significant nonlinearity in the I-V characteristics makes them suitable for digital and pulsed devices [13]. Nevertheless, the Current-Phase Relation (CPR) is one of the fundamental properties of a Josephson junction. When an insulator separates two superconductors, the Josephson current is typically proportional to $\sin\theta$, where $\theta = \varphi_R - \varphi_L$ denotes the phase difference between the right (φ_R) and left (φ_L) superconductors [14]. If the superconductors have two or more conduction bands, as in iron pnictides, the relation becomes more complex [15]. Studies show that even in the absence of a phase difference between the superconductors, a Josephson current can arise due to the internal phase difference between bands [15–18]. While the BCS theory adequately describes conventional superconductors, many unconventional superconductors deviate from BCS predictions. Time-reversal symmetry is generally preserved in the mean-field Hamiltonian of two-band superconductors [19]. However, mounting evidence suggests that time-reversal symmetry breaking (TRSB) occurs in several unconventional systems [20–22]. The time-reversal operation affects the Hamiltonian H such that $\Theta H \Theta^{-1} = H$. TRSB occurs when this condition is violated [19, 23, 24]. Besides intrinsic magnetism, local disruptions can also break time-reversal symmetry, influencing the local quasiparticle spectrum. Vortices carrying fractional flux become strongly pinned to domain walls in superconductors with broken time-reversal symmetry, leading to atypical flux-flow dynamics [24].

[a]Corresponding author: masi.avarideh@email.kntu.ac.ir
[b]afzali@kntu.sc.ir

This research considers a junction between two dissimilar double-band s-wave superconductors (Figure 1). After deriving the current-phase relation, we examined the dependence of the Josephson current on the phase under two conditions. In the first case, we assumed that time-reversal symmetry was preserved in one of the superconductors but broken in the other. The results showed that the current-phase relationship is exactly the opposite of the case where time-reversal symmetry is preserved in both superconductors. In the second case, we assumed that time-reversal symmetry was broken in both superconductors. Under these conditions, the results were similar to the case where both superconductors were in a time-reversal symmetric state.

In contrast to previous studies, such as Sasaki et al. [15], which focused on time-reversal symmetric Josephson junctions composed of two-band superconductors, our work investigates both symmetric and time-reversal symmetry-breaking configurations. In particular, we explore the case in which time-reversal symmetry is broken in only one of the superconductors. This asymmetric situation leads to non-trivial modifications in the current-phase relation, including spontaneous supercurrents that appear even without phase difference. Furthermore, our analysis includes the role of inter-band hybridization in such time-reversal symmetry-broken systems, revealing new contributions to the Josephson current that were not previously addressed.

2 Introduction to Current-Phase Relation

When an electron tunnels through a barrier, it generates an electron state on one side and a hole state on the opposite side (left and right) of the barrier. The Hamiltonian describing this process can be expressed as [2, 15, 18]:

$$H_J = H_L + H_R + \mathscr{T}, \tag{1}$$

$$\mathscr{T} = \sum_{p,q,\sigma} \left(\mathscr{T}_{pq} a^{\dagger}_{\sigma p} a_{\sigma q} + \mathscr{T}^{*}_{pq} a^{\dagger}_{\sigma q} a_{\sigma p} \right), \tag{2}$$

where H_L and H_R denote the Hamiltonians of the left and right superconductors, respectively, and $\mathscr{T}_{pq}$ describes the tunneling matrix elements that determines the probability of tunneling. The operators $a^{\dagger}_{p\sigma}$ and $a_{p\sigma}$ are the creation and annihilation operators for electrons on the left superconductor with momentum $\mathbf{p}$ and spin σ, respectively. Similarly, $a^{\dagger}_{q\sigma}$ and $a_{q\sigma}$ are the corresponding operators for electrons on the right superconductor with momentum $\mathbf{q}$ and spin σ.

The Josephson current can be expressed as [25]:

$$J = 2e\,\mathrm{Im}\left[T \sum_{i\omega_n} \sum_{k,p} \mathrm{Tr}\left(\hat{t}_T\, \hat{\mathscr{F}}^{\dagger}_R(k, i\omega_n)\, \hat{t}_T\, \hat{\mathscr{F}}^{\dagger}_L(k, i\omega_n) \right) \right], \tag{3}$$

where $\hat{\mathscr{F}}_L(k, i\omega_n)$ and $\hat{\mathscr{F}}_R(k, i\omega_n)$ are the anomalous Green's functions for the left and right superconductors, respectively. Here, $\hat{\mathscr{F}}^{\dagger}_R(k, i\omega_n) = \hat{\mathscr{F}}_R(-k, -i\omega_n)$. The operator Tr denotes the trace over internal degrees of freedom (e.g., spin or band indices), T is the temperature, e is the electron charge, and Im denotes the imaginary part. The matrix $\hat{t}_T$ represents the tunneling matrix between the superconductors.

The fermionic Matsubara frequencies are given by $\omega_n = (2n+1)\pi T, \quad n = 1, 2, 3, \ldots$ The current-phase relation (CPR) is a central feature of the Josephson junction. In only a few special cases, it simplifies to the classical sinusoidal form with a critical current J_c [18], namely:

$$J = J_c \sin\varphi, \tag{4}$$

The maximum current J_c in the current-phase relation (CPR) is called the *critical current*. In general, it depends on the temperature, the magnetic field, and may include effects due to fluctuations [2]. Additionally, the phase difference of the superconducting order parameters across the junction is given by $\varphi = \varphi_R - \varphi_L$, where φ_R and φ_L are the phases of the right and left superconductors, respectively [15].

In general, the dependence of the supercurrent J on the phase difference φ can be written as a Fourier series [2]:

$$J(\varphi) = \sum_{n \geq 1} \left[J_c \sin(n\varphi) + J_n \cos(n\varphi) \right], \tag{5}$$

It is predicted that if time-reversal symmetry is preserved, the cosine harmonic coefficients J_n in the Fourier expansion vanish [2, 19, 26, 27]. However, some characteristics of the current-phase relation (CPR) are quite universal and do not depend on the specific material, geometry of the junction, or theoretical framework used to describe it. For example, reversing the direction of supercurrent flow necessarily results in a reversal of the phase difference's sign [5]:

$$J(\varphi) = -J(-\varphi). \tag{6}$$

Moreover, $J(\varphi)$ is a 2π-periodic function [5], i.e.,

$$J(\varphi) = J(\varphi + 2\pi). \tag{7}$$

The investigation of the CPR in diverse junctions, such as superconductor-insulator-superconductor (SIS), double-barrier, superconductor-ferromagnet-superconductor (SFS), and superconductor-constriction-superconductor point-contact junctions, shows that the CPR exhibits different structures for each type of junction [16, 17, 19].

3 Description of Our Model

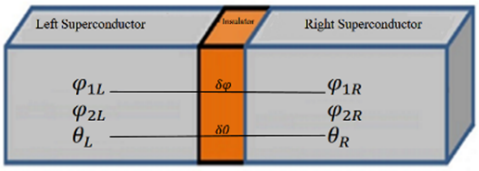

Fig. 1 Schematic picture of the Josephson structure considered in this article.

The supercurrent consists of three distinct terms in a Josephson junction consisting of two dissimilar s-wave spin-singlet two-gap superconductors separated by an insulator. The first term arises from the tunneling of electron pairs between the first conduction band, the second term arises from the tunneling of electron pairs between the second conduction band, and the third term corresponds to the tunneling of electron pairs induced by band hybridization.

In the following equations, the currents resulting from the tunneling of electron pairs in the first and second conduction bands are denoted by J_1 and J_2, respectively. The current arising from the tunneling of an induced electron pair due to band hybridization is given by J_{12} [15, 16]. In these expressions, the indices $\alpha = L,R$ refer to the left and right superconductors, and the band indices $\beta = 1,2$ represent the first and second conduction bands. The quantity υ_α denotes the hybridization amplitude between the two bands in superconductor α, while $\xi_{\alpha\beta}$ is the kinetic energy of an electron in band β on side α. The superconducting order parameter is denoted by $\Delta_{\alpha\beta}$, and T represents the temperature. The tunneling matrix elements through the barrier in band β on side α are represented by t_α. Finally, the phase factors are given by $e^{i\varphi_{\alpha\beta}}$ and $e^{i\theta_\alpha}$, where $\varphi_{\alpha\beta}$ is the phase of the superconducting order parameter in band β of superconductor α, and θ_α is an internal phase related to time-reversal symmetry.

3.1 First Condition: Just One Superconductor is in a Time-Reversal Symmetry State

$$J_1 = \mathrm{Im}\sum_{kp} eT \sum_{\omega_n} \left[\frac{t_1^2 \left[\left(\xi_{2R}^2 + |\Delta_{2R}|^2 + \omega_n^2\right) |\Delta_{1R}| + \upsilon_R^2 |\Delta_{2R}|\, e^{i(2\theta_R + \varphi_{2R} - \varphi_{1R})} \right]}{\left(\xi_{1R}^2 + |\Delta_{1R}|^2 + \omega_n^2\right)\left(\xi_{2R}^2 + |\Delta_{2R}|^2 + \omega_n^2\right) + \upsilon_R^2\left(\omega_n^2 - \xi_{1R}\xi_{2R}|\Delta_{1R}||\Delta_{2R}|\cos(\varphi_{2R} - \varphi_{1R} + 2\theta_R) + \upsilon_R^4\right)} \right. \\ \left. \times \frac{\left[\left(\xi_{2L}^2 + |\Delta_{2L}|^2 + \omega_n^2\right) |\Delta_{1L}| + \upsilon_L^2 |\Delta_{2L}|\, e^{i(2\theta_L + \varphi_{1L} - \varphi_{1L})} \right] \cdot e^{i(\varphi_{1L} - \varphi_{1R})}}{\left(\xi_{1L}^2 + |\Delta_{1L}|^2 + \omega_n^2\right)\left(\xi_{2L}^2 + |\Delta_{2R}|^2 + \omega_n^2\right) + \upsilon_L^2\left(\omega_n^2 - \xi_{1L}\xi_{2L}|\Delta_{1L}||\Delta_{2L}|\cos(\varphi_{2L} - \varphi_{1L} + 2\theta_L) + \upsilon_L^4\right)} \right], \tag{8}$$

$$J_2 = \mathrm{Im}\sum_{kp} eT \sum_{\omega_n} \left[\frac{t_2^2 \left[\left(\xi_{1R}^2 + |\Delta_{1R}|^2 + \omega_n^2\right) |\Delta_{2R}| + \upsilon_R^2 |\Delta_{1R}|\, e^{i(2\theta_R + \varphi_{2R} - \varphi_{1R})} \right]}{\left(\xi_{1R}^2 + |\Delta_{1R}|^2 + \omega_n^2\right)\left(\xi_{2R}^2 + |\Delta_{2R}|^2 + \omega_n^2\right) + \upsilon_R^2\left(\omega_n^2 - \xi_{1R}\xi_{2R}|\Delta_{1R}||\Delta_{2R}|\cos(\varphi_{2R} - \varphi_{1R} + 2\theta_R) + \upsilon_R^4\right)} \right. \\ \left. \times \frac{\left[\left(\xi_{1L}^2 + |\Delta_{1L}|^2 + \omega_n^2\right) |\Delta_{2L}| + \upsilon_L^2 |\Delta_{1L}|\, e^{i(2\theta_L + \varphi_{2L} - \varphi_{1L})} \right] \cdot e^{i(\varphi_{2L} - \varphi_{2R})}}{\left(\xi_{1L}^2 + |\Delta_{1L}|^2 + \omega_n^2\right)\left(\xi_{2L}^2 + |\Delta_{2R}|^2 + \omega_n^2\right) + \upsilon_L^2\left(\omega_n^2 - \xi_{1L}\xi_{2L}|\Delta_{1L}||\Delta_{2L}|\cos(\varphi_{2L} - \varphi_{1L} + 2\theta_L) + \upsilon_L^4\right)} \right], \tag{9}$$

$$J_{12} = \mathrm{Im}\sum_{kp} eT \sum_{\omega_n} \left[\begin{array}{c} t_1 t_2 \left(\left[\xi_{1R}|\Delta_{2R}| e^{i(\varphi_{2R} - \theta_R} + \xi_{2R}|1R| e^{i(\varphi_{1R} - \theta_R}\right] \left[\left(\xi_{1L}|\Delta_{2L}| e^{i(\varphi_{2L} - \theta_L}\right) + \xi_{2L}|\Delta_{1L}| e^{i(\varphi_{1L} - \theta_L}\right] \right. \\ \left. + \left[|\Delta_{2R}| e^{i(\varphi_{2R} - \theta_R)} - |\Delta_{1R}| e^{i(\varphi_{1R} - \theta_R)} \right] \left[|\Delta_{2L}| e^{i(\varphi_{2L} - \theta_L} - |\Delta_{1L}| e^{i(\varphi_{1L} - \theta_L} \right] \omega_n^2 \right) \upsilon_R \upsilon_L \cdot e^{i\theta_R}\, e^{-i\varphi_{1R}} \\ \hline \left\{ \left(\xi_{1R}^2 + |\Delta_{1R}|^2 + \omega_n^2\right)\left(\xi_{2R}^2 + |\Delta_{2R}|^2 + \omega_n^2\right) + \upsilon_R^2\left(\omega_n^2 - \xi_{1R}\xi_{2R}|\Delta_{1R}||\Delta_{2R}|\cos(\varphi_{2R} - \varphi_{1R} + 2\theta_R) + \upsilon_R^4\right) \right\} \\ \times \left\{ \left(\xi_{1L}^2 + |\Delta_{1L}|^2 + \omega_n^2\right)\left(\xi_{2L}^2 + |\Delta_{2R}|^2 + \omega_n^2\right) + \upsilon_L^2\left(\omega_n^2 - \xi_{1L}\xi_{2L}|\Delta_{1L}||\Delta_{2L}|\cos(\varphi_{2L} - \varphi_{1L} + 2\theta_L) + \upsilon_L^4\right) \right\} \end{array} \right] \tag{10}$$

To observe the time-reversal symmetry state, the phases of the first and second conduction bands must satisfy:

$$2\theta_R = \varphi_{1R} - \varphi_{2R} + 2\pi n_R. \tag{11}$$

Therefore, for the state in which time-reversal symmetry is broken [16]:

$$2\theta_R \neq \varphi_{1R} - \varphi_{2R} + 2\pi n_R. \tag{12}$$

So, the relationship between the phases in the state of broken time-reversal symmetry could be assumed as

$$2\theta_R = \varphi_{1R} - \varphi_{2R} + \pi n_R. \tag{13}$$

Based on the phase configuration assumed in Eq. (13), and considering the three distinct tunneling contributions in Eqs. (8)–(10), we derive the general form of the current-phase relation (CPR) when time-reversal symmetry is broken in only one superconductor:

$$\begin{aligned} J &= J_1' \sin(\delta\varphi) + J_2' \sin(-2\delta\theta + \delta\varphi) + J_{12}' \sin(\delta\varphi - \delta\theta) \\ \implies J &= J' \sin(\delta\varphi) \\ &\quad + J_2'[\sin(\delta\varphi)\cos(2\delta\theta) - \sin(2\delta\theta)\cos(\delta\varphi)] \\ &\quad + J_{12}'[\sin(\delta\varphi)\cos(\delta\theta) - \sin(\delta\theta)\cos(\delta\varphi)], \end{aligned} \tag{14}$$

where $J'_{1(2,12)}$ represent the amplitudes of the currents corresponding to the first, second, and third components, respectively, and are temperature-dependent. We define the relative phase difference between the superconductors as $\delta\theta = \theta_L - \theta_R$, which depends on the intrinsic characteristics of the superconductors. Additionally, we consider $\delta\varphi_1 \equiv \varphi_{1L} - \varphi_{1R}$, and define the average phase as $\varphi_{1L(R)} = \frac{1}{2}\left(\varphi_{1L(R)} + \varphi_{2L(R)}\right)$. Regarding the internal phase relations within each superconductor, two possible configurations are considered. In the S++ configuration, the phases satisfy $\varphi_1 = \varphi_2$, while in the S+− configuration, the relative phase satisfies $\varphi_1 - \varphi_2 = \pi$.

3.1.1 S++/S++ Junction

In this situation, for the superconductor that preserves time-reversal symmetry, we have $\delta\theta = -\frac{\pi}{2}, \frac{\pi}{2}$ while for the other superconductor, $\theta_L = \frac{\pi}{2}, -\frac{\pi}{2}$. Considering Eq. (14), the current-phase relation (CPR) takes the form:

$$\begin{aligned} &\delta\theta = \pm\frac{\pi}{2} \implies \\ &\qquad J = J_1' \sin(\delta\varphi) - J_2' \sin(\delta\varphi) \mp J_{12}' \cos(\delta\varphi), \end{aligned} \tag{15}$$

3.1.2 S+-/S+- Junction

Similar to the previous situation, in this junction configuration we also obtained $\delta\theta = \frac{\pi}{2}, -\frac{\pi}{2}$, and the result is consistent with the findings in Section 3.1.1.

3.1.3 S++/S+- Junction

Under this condition, we consider the phase relation $\varphi_{1R} - \varphi_{2R} = \pi$, which implies $\theta_R = \frac{\pi}{2}, -\frac{\pi}{2}$, $\theta_L = \frac{\pi}{2}, -\frac{\pi}{2}$, and thus, $\delta\theta = 0$, π, or $-\pi$. Based on Eq. (14), for this junction configuration, the sign reversal in one of the bands leads to partial cancellation in the hybridized current contributions modifying the overalln (CPR) with an inherent asymmetry not present in fully symmetric configurations. The interference terms may no longer add constructively, giving rise to spontaneous currents or non-sinusoidal CPR asymmetry.

$$\begin{aligned} &\delta\theta = 0 \implies \\ &\qquad J = J_1' \sin(\delta\varphi) + J_2' \sin(\delta\varphi) + J_{12}' \sin(\delta\varphi), \end{aligned} \tag{16}$$

$$\begin{aligned} &\delta\theta = \pm\pi \implies \\ &\qquad J = J_1' \sin(\delta\varphi) - J_2' \sin(\delta\varphi) - J_{12}' \cos(\delta\varphi), \end{aligned} \tag{17}$$

It is obvious that θ affects the Josephson current in all the situations discussed above by modifying the sign of the last term in the current expression. Moreover, in $S{+}{+}/S{+}{+}$ and $S{+}{-}/S{+}{-}$ junctions, this last term leads to supercurrent flow even in the absence of a phase difference (i.e., $\delta\varphi = 0$). This behavior is in stark contrast to the behavior observed in Josephson junctions composed of two superconductors that both preserve time-reversal symmetry.

3.2 Second Condition: Both Superconductors Break Time-Reversal Symmetry

In this section, we consider Eq. (12) to be valid for both superconductors. All other assumptions remain the same as those outlined in Section 3.1.

3.2.1 S++/S++ Junction

Under this circumstance, for both superconductors, $\varphi_1 - \varphi_2 = 0$, and $\theta_{L(R)} = \frac{\pi}{2}, -\frac{\pi}{2}$. Therefore, $\delta\theta = 0, \pi$, and we conclude:

$$\begin{aligned} &\delta\theta = 0 \implies \\ &\qquad J = J_1' \sin(\delta\varphi) + J_2' \sin(\delta\varphi) + J_{12}' \sin(\delta\varphi), \end{aligned} \tag{18}$$

$$\delta\theta = \pi \implies$$
$$J = J_1' \sin(\delta\varphi) + J_2' \sin(\delta\varphi) - J_{12}' \cos(\delta\varphi), \quad (19)$$

3.2.2 S+-/S+- Junction

Similar to Section 3.2.1, in this junction the CPR is described by Eqs. (18) and (19).

3.2.3 S++/S+- Junction

In this section, we assumed $\theta_L = \pm\frac{\pi}{2}$ and $\theta_R = 0$. The CPR is described by:

$$\theta_L = \pm\frac{\pi}{2}, \theta_R = 0 \implies$$
$$J = J_1 \sin(\delta\varphi) - J_2 \sin(\delta\varphi) + J_{12} \pm \cos(\delta\varphi), \quad (20)$$

$$\theta_L = \pm\frac{\pi}{2}, \theta_R = \pi \implies$$
$$J = J_1 \sin(\delta\varphi) - J_2 \sin(\delta\varphi) + J_{12} \mp \cos(\delta\varphi), \quad (21)$$

Again, it is evident that θ modifies the Josephson current by altering the sign of the last term. However, this junction's result is similar to that of a junction consisting of two superconductors with time-reversal symmetry [15].

It is worth emphasizing that the sign structure of the superconducting gaps—i.e., whether the system is in an S++ or S± state—plays a crucial role in determining the behavior of the Josephson current. In S++ junctions, the constructive phase alignment between bands enhances the magnitude and symmetry of the CPR. In contrast, S± configurations introduce sign changes that may cancel or invert certain contributions, especially under broken time-reversal symmetry conditions.

We explicitly compare the S++ and S± configurations to clarify the qualitative impact of gap symmetry on the CPR. In the S++ state, both superconducting gaps have the same sign, leading to constructive interference between the interband tunneling contributions. As a result, the CPR is symmetric and typically dominated by first harmonic components.

However, in the S± state, the sign reversal between the bands introduces destructive interference, particularly in the current's interband (hybridization-induced) component. This can lead to significant deviations from the conventional sinusoidal CPR, including suppression of the critical current and the emergence of higher harmonics or phase shifts.

Figure 2 shows the CPR curves for a symmetric S++/S++ junction and a sign-reversed S±/S± junction, both

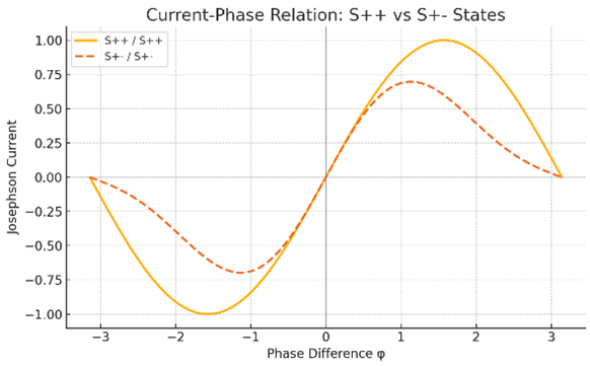

Fig. 2 Comparative CPR for S++ and S± states under time-reversal symmetric conditions.

under time-reversal symmetric conditions. As shown, the S± configuration leads to an overall reduction in current amplitude and a distortion in the CPR shape due to phase cancellation effects. This qualitative difference becomes even more pronounced when time-reversal symmetry is broken in one or both superconductors, leading to spontaneous currents and asymmetric CPRs, as discussed in previous sections.

4 Conclusions

A Josephson junction consisting of two dissimilar double-band superconductors separated by an insulating barrier was considered. The effect of time-reversal symmetry on the current-phase relation (CPR) was studied under two different conditions: first, when only one of the superconductors preserved time-reversal symmetry, and second, when both superconductors broke time-reversal symmetry. The results were compared with the case where both superconductors preserved time-reversal symmetry.

Contrary to an isolated superconductor, we conclude that the gauge parameter modifies the Josephson current. However, the CPR was similar when both superconductors were in the same time-reversal symmetry state—regardless of whether they broke or preserved the symmetry. In contrast, if only one broke the symmetry, the result was the opposite.

The modifications in the CPR observed under time-reversal symmetry breaking conditions can be intuitively understood as arising from the asymmetry in the phase structure of the superconducting order parameters. When time-reversal symmetry is broken, especially asymmetrically across the junction, complex inter-band phase differences and hybridization terms contribute to the Josephson current in a way that is not invariant under phase inversion. As a result, higher-order harmonics and phase shifts emerge in the CPR. In such scenarios, spontaneous supercurrents may appear even in the absence of an applied phase differ-

ence, highlighting the role of symmetry in shaping the transport properties of Josephson junctions.

References

1. B. D. Josephson, *Physics Letters*, **1**, 1962
2. F. Tafuri, Springer Nature, (2019)
3. S. Shapiro, Phys. Rev. Lett., **11**, (1963)
4. B. J. Benz,S. Benz, Eur. Phys. J., **(172)**, (2009)
5. B. W. Petley, TContemp. Phys., **10**, (1969)
6. V. V. Ryazanov et al., *Phys. Procedia*, **36**, (2012)
7. B. W. Petley, K. M. Petley, *Metrologia*, **6**, (1970)
8. V. V. Ryazanov et al., *Phys. Rev. Lett.*, **96**, (2006)
9. T. Golod, V. K. Oboznov, *Phys. Rev. Applied*, **11**, (2019)
10. M. Y. Kupriyanov et al., *Phys. Rev. Lett.*, **96**, (2006)
11. M. Fiske *Rev. Mod. Phys.*, **36**, (1964)
12. C. A. Hamilton, *Phys. Rev. B*, **5**, (1972)
13. I. Askerzade, *Tech. Phys.*, **51**, (2006)
14. V. Ambegaokar, A. Baratoff, *Phys. Rev. Lett.* **10**, (1963)
15. A. Sasaki, *Phys. Rev. B*, **101**, (2020)
16. A. A. Golubov, *Rev. Mod. Phys.*, **76**, (2004)
17. A. L. Kasatkin, E. A. Pashitskii, *Ukr. Fiz. Zh.*, **21**, (1976)
18. I. Askerzade, M. C. Abul-Magd, *Modern Aspects of Josephson Dynamics and Superconductivity Electronics*, Springer, (2017)
19. Y. Asano, *Phys. Rev. B*, **97**, (2018)
20. B. M. Andersen, *Front. Phys.*, **12**, (2024)
21. S. K. Ghosh, *J. Phys.: Condens. Matter*, **32**, (2020)
22. G. M. Luke, *Nature*, **394**, (1998)
23. J. J. Sakurai, J. Napolitano, *Modern Quantum Mechanics*, Cambridge University Press, (2020)
24. V. K. Anand, *Phys. Rev. B*, **107**, (2023)
25. G. D. Mahan, *Many-Particle Physics*, Plenum Press, New York, (1990)
26. M. Tinkham, *Introduction to Superconductivity*, 2nd Ed., Dover Publications, (2004)
27. A. I. Buzdin, *Rev. Mod. Phys.*, **77**, (2005)